2d DI-HADRON CORRELATIONS AT $\sqrt{S_{NN}} = 2.76$ TeV USING THE ALICE EXPERIMENT

A Dissertation

Presented to

the Faculty of the Department of Physics

University of Houston

In Partial Fulfillment

of the Requirements for the Degree

Doctor of Philosophy

By

Danthasinghe Waduge Badrajee Piyarathna

May 2015

2d DI-HADRON CORRELATIONS AT $\sqrt{S_{NN}} = 2.76$ TeV USING THE ALICE EXPERIMENT

Danthasinghe Waduge Badrajee Piyarathna

APPROVED:

Prof. Rene Bellwied, Chairman
Dept. of Physics

Prof. Kevin Bassler
Dept. of Physics

Prof. Ed Hungerford
Dept. of Physics

Prof. Lawrence S. Pinsky
Dept. of Physics

Prof. Eric Bittner
Dept. of Chemistry

Dean, College of Natural Sciences and Mathematics

Acknwoledgements

As a high school kid, I was amazed by the modern accelerators and their quest of finding the nature at the smallest scale. As of today, that thirst has led me to earn a Ph.D in physics. First and foremost I offer my sincerest gratitude to my supervisor, Prof. Rene Bellwied, and the group members, who has supported me throughout my physics graduate life with patience and knowledge. Second, deepest gratitude goes goes to the academic and non-academic staff in the department of physics, University of Colombo, Sri Lanka, who laid the foundation for a graduate physics studies. I acknowledge the Department of Physics University of Houston, committee members and all the staff members for helping me to smoothen my life as of being a graduate student. Further, I wish to express my sincere appreciation to to the ALICE collaboration and it's colleagues. I would like to express my heartfelt thanks to back bone of my work, my family for their continued support and enthusiasm during the period of study. Many thanks to you, my Mother, Father and Brother, for the utmost support given to me through out my journey being a physicist. Without you, I would not have become who I'm today. I hope this dissertation brings you happiness and pride, as much as it does for me. Thank you my loving wife, Eranga, and the little bundle of joy, our daughter Yashodhya for coming into my life and sharing your love with me. At last, a huge thank you to all my beloved relatives, in-laws, Sri Lankan friends, my teachers from kindergarten to high school, my, colleagues and everyone in Sri Lanka for the loving support and company. Deepest gratitude to everyone! Thank You!.

2d DI-HADRON CORRELATIONS AT $\sqrt{S_{NN}} = 2.76$ TeV USING THE ALICE EXPERIMENT

An Abstract of a Dissertation

Presented to

the Faculty of the Department of Physics

University of Houston

In Partial Fulfillment

of the Requirements for the Degree

Doctor of Philosophy

By

Danthasinghe Waduge Badrajee Piyarathna

May 2015

Abstract

The Large Hadron Collider (LHC) at CERN Geneva, Switzerland, attempts to recreate the initial conditions at the begining of our universe. Heavy ions (Pb^{208}_{82}) are accelerated up to 0.999999 of the speed of the light and collided at $\sqrt{s_{NN}} = 2.76\ TeV$ (center of mass energy per nucleon) in order to recreate the initial energy density ($\sim 10^{-6}s$) after the Big Bang. The theory of Quantum Chromo Dynamics (QCD) predicts the formation of a primordial nuclear matter phase known as Quark Gluon Plasma (QGP) under these experimental conditions. This dissertation focuses on studying this QCD medium using data from the 'A Large Ion Collider Experiment' (ALICE).

The study of two-dimensional two-particle correlations of emitted charged particles carries valuable time integrated information of the dynamical QCD medium. Long-range correlations between particles in angular and momentum space generally can be attributed to collective behavior, which is not found in a superposition of elementary collisions. The focus of this thesis is to understand the long-range correlation structure observed in pseudo-rapidity ($\Delta\eta$) as a function of p_T and to obtain better estimates of medium properties of the QGP, such as shear viscosity. The interpretation is based on empirical models describing well-established hydrodynamical collective flow phenomena and possible novel phenomena related to in-medium parton fragmentation. The flow and Gaussian parameters extracted from the fit model can be used to constrain medium properties such as the initial gluon density, the shear viscosity and the partonic energy transport coefficient.

Contents

List of Figures

List of Tables

Chapter 1

Heavy-Ion physics of the LHC

As human beings our ancestors always used to observe the sky and the stars and tried to find the answer to the most fundamental question "Who are we?", "And where do we come from?". Over thousands of years, they gained knowledge about the universe, and found it filled with stars, planets, galaxies, clusters and superclusters etc. The other fundamental question is "What is the universe made of?". Starting from basic substances such as water, air, and soil we have now achieved the resolution to identify quarks and leptons as the basic building blocks of the observable matter in the universe [1]. The Big Bang theory is the most widely accepted theory in cosmology [2]. The model offers a comprehensive explanation for a broad range of observations. Fractions of a millionth of a second after the Big Bang, the universe was filled with an extremely hot and dense phase made of quarks and gluons. Gluons are the carriers of the strong force which bind quarks together. At these extreme conditions quarks and gluon were weakly bound and the medium is termed the

quark-gluon plasma. Scientists at CERN built the Large Hadron Collider in order to recreate the conditions just after the Big Bang to study the quark-gluon plasma.

1.1 The evolution of the universe

1.1.1 Initial singularity

The Big Bang theory cosmology predicts an absolute beginning of the universe about 13.8 billion years ago, whose beginning prior to the Planck-scale is uncertain. At this point all the fundamental interactions were a single unified force. This initial state was followed by inflation and then expansion. The prevailing scientific evidence to support the Big Bang model is the Cosmic Microwave Background (CMB). The red-shift measurements further support the picture of an expanding universe. Furthermore, the abundance of light elements, such as Hydrogen and Helium, in the universe also supports the Big Bang model, as described in Figure 1.1.

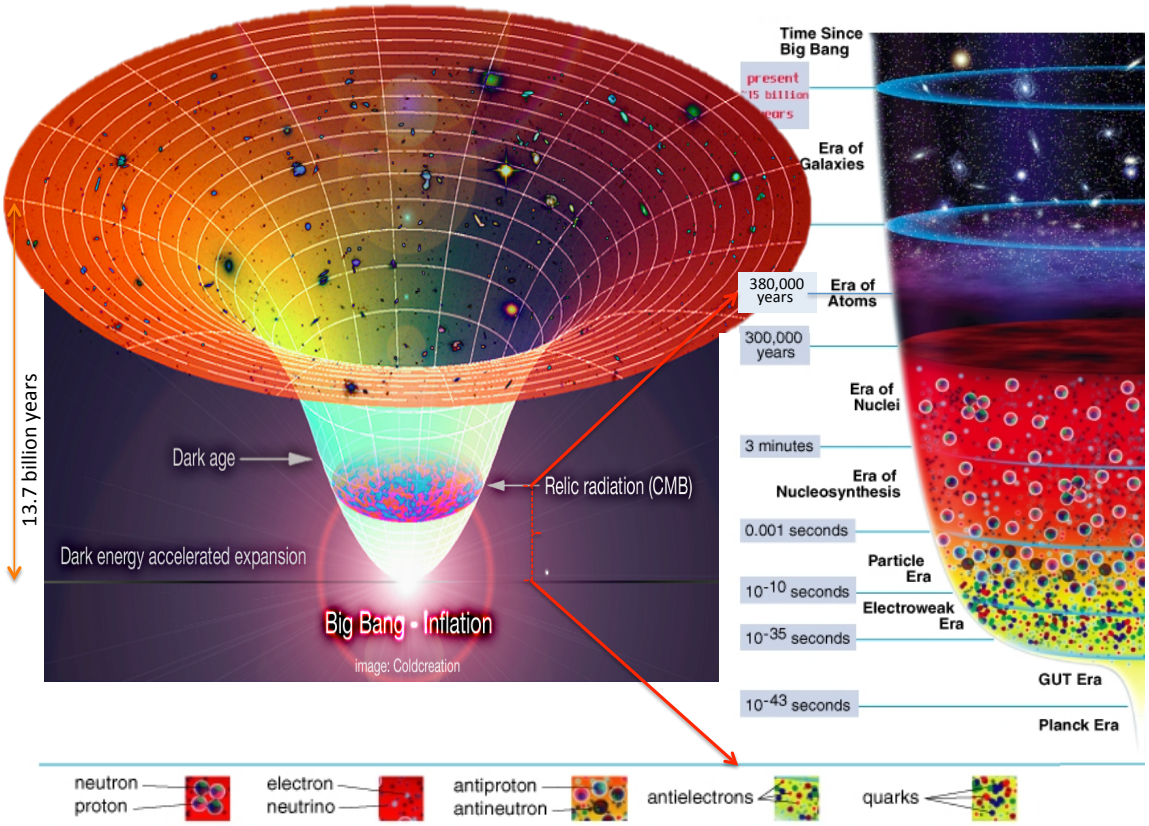

Figure 1.1: Chronology of the universe according to the Big Bang model [166].

1.1.2 Cosmic microwave background

The CMB is the thermal radiation assumed to be remnant of the Big Bang. The CMB was accidentally discovered in 1964 by two American radio astronomers Penzias and Wilson [3]. They won the Nobel prize for their discovery. This radiation was strongest in the microwave range and was detected using radio telescopes. Figure 1.2 shows the measure of temperature anisotropies in CMB based on the **W**ilkinson **M**icrowave **A**nisotropy **P**robe (**WMAP**) [178] and Figure 1.3 is the most recent

higher resolution measurement from the Planck spacecraft in 2013 [179].

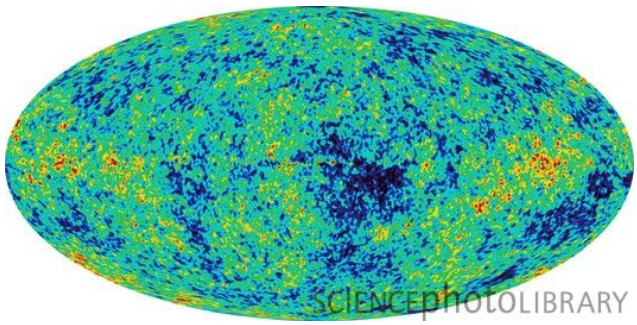

Figure 1.2: WMAP measurement of the temperature in the present-day universe [178].

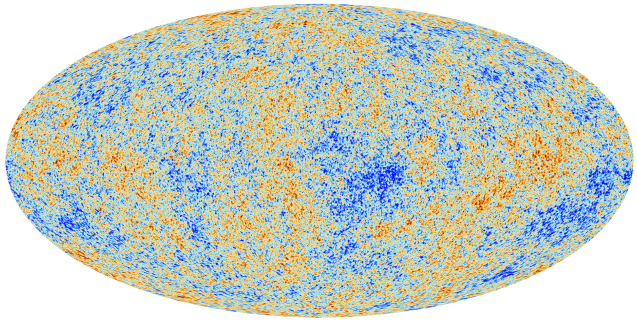

Figure 1.3: Planck measurement of the temperature in the present-day universe [179].

The discovery of the CMB was a landmark test of the Big Bang model of the universe.

1.1.3 Expanding universe

The successive evolution, after cosmic inflation, in the Big Bang model predicts a constantly expanding universe. The cosmological red shift (Hubble expansion) provides the strongest evidence for such a model.

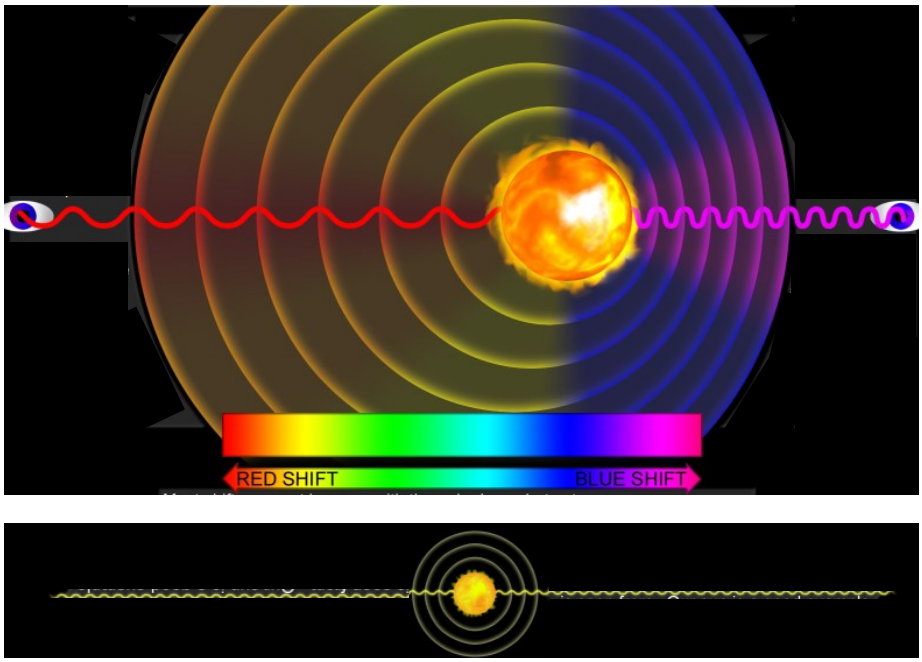

Figure 1.4: Cosmological red shift explained [167].

As explained in the Doppler effect, the receiving frequency from a source increases (tends to higher frequency) when the source is moving towards and decreases when moving away from the observer. As shown in Figure 1.4, if the light from stars or galaxies (electromagnetic radiation) received by an observer on earth is shifted to larger wavelengths, the star or galaxy is moving away from the observer. On the other hand, blue-shifted frequencies indicate that the source is moving towards the observer. The observed spectrum from distant galaxies are "red-shifted" and therefore move away from us. This observation is quantified in the Hubble law, which states that the recession velocity is a function of distance, implying that the observed universe is expanding [5].

1.1.4 The evolution of fundamental interactions

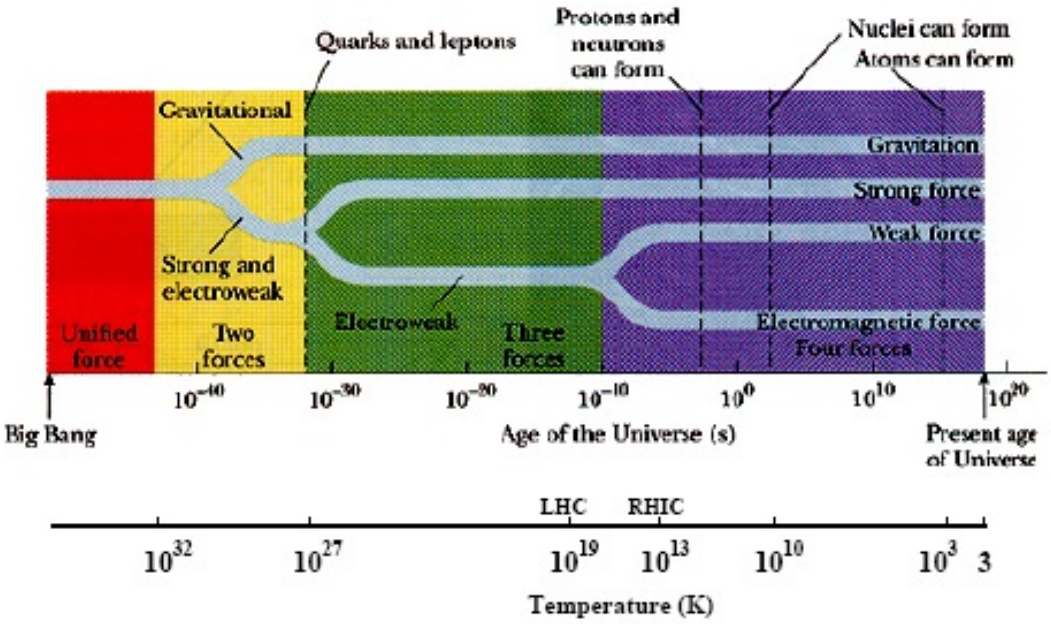

Figure 1.5: The summary of our current understanding of the time evolution of fundamental interactions.

According to the Big Bang theory, the beginning of our universe occurred around 13.8 billion years ago. Figure 1.5 shows the time evolution of the fundamental interactions. The time up to $10^{-43}s$ after the Big Bang is known as the Planck epoch. During this epoch, all four fundamental forces of nature we observe today were unified as one force, and quantum effects of gravity were significant. This unstable or transitory hot dense initial state evolved giving rise to the fundamental forces we observe today via a process known as symmetry breaking. The symmetry breaking processes took place successively giving rise to the Grand unification epoch. The Grand unification epoch ($\sim 10^{-43}s$ – $\sim 10^{-36}s$) began when and the gravitational force separated from the other fundamental forces of nature.

The electroweak epoch followed the Grand unification epoch, and the strong interaction separated from electroweak interactions. The proposed cosmic inflation period ($10^{-36}s$ – $10^{-32}s$) also occurred simultaneously, causing a rapid exponential expansion of the universe. By the end of inflationary era, the volume of entire universe increased at least by a factor of 10^{78} while filling the entire universe with dense and hot quarks, anti quarks and gluons.

The $W^{\pm}$, Z^0 [6] and Higgs bosons [7,8] were produced as a result of interactions between high energetic particles during the electroweak epoch. The successive expansion and cooling down of the universe stopped the further creation of W and Z bosons. The remaining particles decayed before the Quark epoch ($10^{-12}s$ – $10^{-6}s$) when all the fundamental interactions took on their present form. The experimental verification of the existence of W, Z and Higgs gauge bosons, which describe the electroweak interaction existed after the inflationary epoch is a milestone of modern physics.

1.2 Symmetries of Quantum Chromo Dynamics (QCD)

1.2.1 Symmetries and symmetry-breaking

The property of symmetry is associated with an observable quantity of a system. Symmetries guarantee that the observed quantity does not change (invariant) under a specific transformation. According to Noether's theorem, there is a conserved

quantity associated with each symmetry of a physical system. For instance, the conservation of linear momentum arises due to the invariance the of the laws of physics due to translation in space. The symmetry breaking of the system arises from critical infinitesimal fluctuations acting on a system. This leads to the system transforming into a different state i.e. from a disordered state into one of two definite states.

1.2.2 Spontaneous symmetry-breaking and gauge theory

Spontaneous symmetry breaking keeps the physical laws which govern the system invariant, but the system itself does not show such behavior. Such phenomena occur as a result of the system being surrounded by a vacuum. Spontaneous symmetry-breaking is often parametrized by an order parameter. In Big Bang cosmology, the underlying transformations between different field configurations result in observable quantities. As mentioned before, if the observed quantity is invariant under different field configurations, then the system preserves the symmetry and we name such symmetries as gauge symmetries (gauge invariance). In addition, we call such transformations gauge transformations and the corresponding theories as gauge theories. With the advancement of quantum field theory, scientists recognized that fundamental interactions of nature are governed by local gauge symmetry constraints. In local gauge symmetries, transformations can vary from point to point in space and time. The Lagrangian of the system is invariant under a continuous group of local gauge transformations.

1.2.3 Gauge fields and standard model in physics

The Lagrangian of a system has a certain number of degrees of freedom. Gauge can be attributed to the number of degrees of freedom in a Lagrangian. The gauge transformation in such a system results in a continuous mathematical group known as Lie group. This gauge group (or symmetry group) is associated to its group of generators through group algebra (for Lie group, it's Lie algebra). Each generator corresponds to a vector field which is known as the gauge field. The Lagrangian associates gauge fields to preserve the invariance under local gauge transformations. The quantized forms of these gauge fields are known as gauge bosons. The gauge theory is called Abelian or non-Abelian depending on whether the symmetry group is commuting or non-commuting. The standard model resembles a non-Abelian gauge theory with the symmetry group U(1)xSU(2)xSU(3), where U(1) represents an Abelian gauge theory which describes the electromagnetic field(interaction) with the photon as the gauge boson. SU(2) is a non-Abelian gauge theory describing the weak interaction with 3 weak bosons. Finally SU(3) is also a non-Abelian gauge theory describing the strong interaction with 8 gluons as gauge bosons. In this thesis work, we focus on the SU(3) non-Abelian gauge symmetry group. We study the strong interaction, and the theory is known as Quantum Chromo Dynamics or QCD. The following subsections will discuss briefly the strong interaction, and how it is studied in an experiment.

1.3 Relativistic Heavy-Ion Physics

1.3.1 Probing strong interaction at Large Hadron Collider (LHC)

The quark epoch occurred approximately ($10^{-12}s$- $10^{-6}s$) seconds after the Big Bang, when the preceding electroweak epoch ended as the electroweak interaction separated into the weak interaction and electromagnetism. Even during the quark epoch the temperature of the universe was still too high for quarks to be bound into hadrons (protons and neutrons). Thus the universe was filled with a dense, hot quark-phase, containing quarks, leptons, and their antiparticles. The fundamental interactions of electromagnetism, gravitation, the strong interaction and the weak interaction were in their present form. This energy regime has been achieved with current accelerator technology at the Relativistic Heavy Ion Collider (RHIC) at Brookhaven National Lab (BNL) and Large Hadron Collider (LHC) at CERN.

1.3.2 Quark-Gluon Plasma and SU(3) gauge group

Quantum Chromo Dynamics is a SU(3) Yang-Mills theory [9]. In the gauge group SU(3), quarks are fermions (spin 1/2) and represented as Dirac fields. The quarks carry color charge which is described in theory as the responsible feature for strong interaction. In QCD gluons are bosons (spin 1) that carry color charge and are represented via the adjoint representation 8 of the SU(3) gauge group. Hence, the strong interaction is described in QCD, as the interaction between quarks and gluons.

The theory features two special properties describing the interaction between quarks and gluons. They are known as confinement and asymptotic freedom. The non-existence of free quarks in nature can be explained via the confinement and the potential in QCD can simply be modeled as shown by equation 1.1.

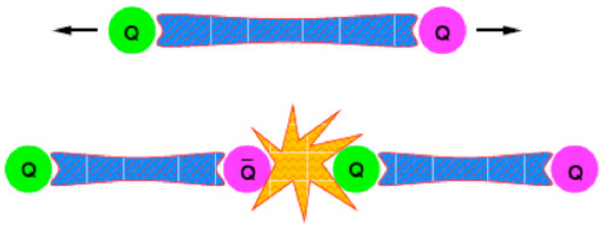

Figure 1.6: Quark confinement.

$$V(r) = -\frac{A(r)}{r} + K(r) \tag{1.1}$$

If we apply forces to pull two quarks apart, the binding force between the quarks increases linearly (see the animated cartoon in Figure. 1.6 top). If we keep pulling them apart, the strong field energy between quarks is released (fig.1.6 bottom). The released energy results in a quark anti-quark pair production. The point is, that the newly produced quark anti-quark pair is now confined in bound states with the original quarks. This feature is explained as the confinement of the quarks in the theory of QCD, and is responsible for generating color neutral hadrons called baryons (three quark combinations) and mesons (quark anti-quark pair) in nature. Figure 1.7 shows the composition of a proton a (baryon) and a π^+ (meson).

The interaction between quarks decreases when they are brought closer together. This phenomena is known as the asymptotic freedom. This prediction of QCD was

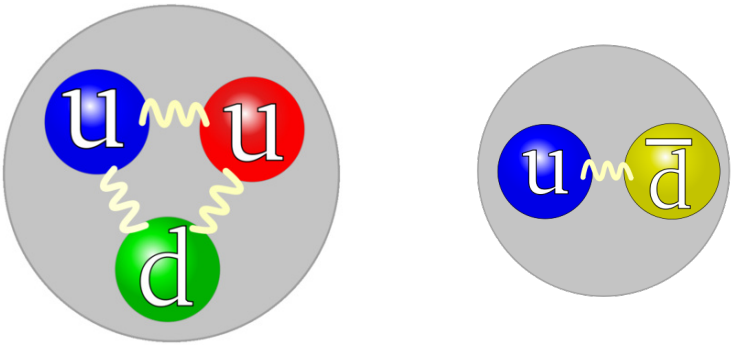

(a) Baryon (b) Meson

Figure 1.7: Quarks confined as a color neutral proton (a) and a color neutral π^+ meson (b).

first made in the early 1970s by David Politzer, Frank Wilczek and David Gross and they won the 2004 Nobel Prize in Physics for their work. This feature of the QCD theory was the basis for the creation of QGP phase of matter in the laboratory. Scientists realized that compressing and heating nuclear matter to the maximally achievable value will overcome confinement and lead to asymptotic freedom in the heated phase. These conditions can be accomplished by colliding heavy-ions close to the speed of light. The initial attempts to create a QGP were at the SPS accelerator at CERN and the AGS at Brookhaven National Laboratory (BNL). The Relativistic Heavy-Ion Collider (RHIC) was then built at BNL to increase the beam energies. Then, in order to bring the quarks even closer together, scientists at LHC attempted to generate the highest possible energy density since 2010.

Figure 1.8 above shows the energy density in a nuclear system as a function of temperature. The sharp rise in the plot signifies a the phase transition behavior from cold nuclear matter to hot dense QGP. In order to create these conditions, scientists at LHC collide Pb heavy-ions at $\sqrt{s_{NN}} = 2.76$ TeV by accelerating them

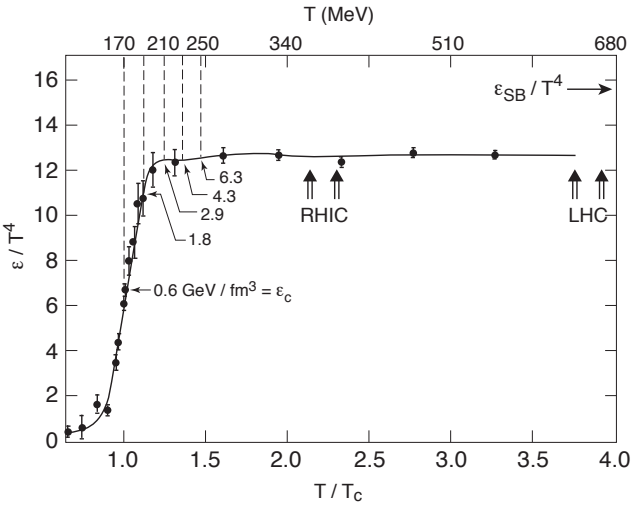

Figure 1.8: Lattice predictions for energy density as a function of temperature [10].

up to 99.999999% of the speed of light. Experimental details will be discussed in second chapter. The remainder of chapter one will discuss the time evolution of a heavy-ion collision, and important QGP signatures scientists observed at RHIC and LHC.

1.3.3 The time evolution of a heavy-ion collision

Figure 1.9 shows the final state charged hadrons detected in the TPC and ITS tracking detectors over 2π azimuth. The figure 1.10 shows the time evolution of a relativistic heavy-ion collision, which produces these final state hadrons.

Figure 1.10 shows (left) a schematic of colliding nuclei. Due to the Lorentz contraction in the beam direction at the relativistic limit, the nuclei look like sheets of nucleons (pancakes) in the Center of Mass (CM) frame. The collisions of nuclei occur

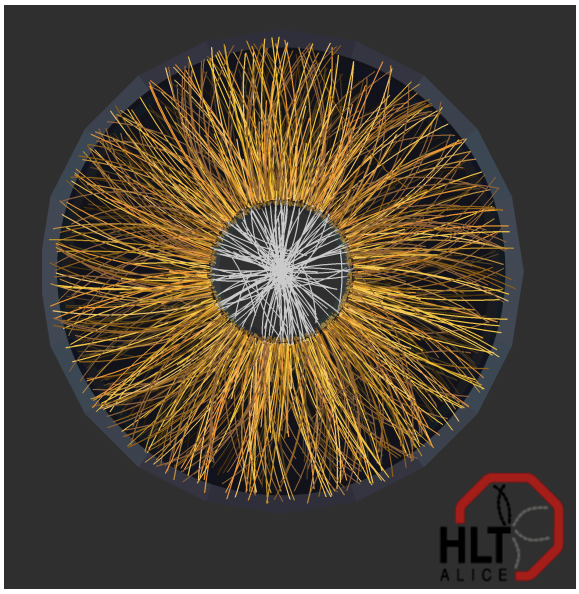

Figure 1.9: The charged particle tracks in an Pb-Pb collision at ALICE as seen in the Time Projection Chamber (TPC, yellow tracks) and Inner Tracking System (ITS, white tracks).

as high-energy inelastic collisions of individual nucleons. Many partons (quarks and gluons) are liberated. As a result high a particle density is created in these collisions, which allows for multiple re-scattering. The initial momentum distribution, which is along the beam axis, is redistributed. In this inelastic scattering process, the nuclei leave a significant amount of energy in the CM frame, producing a fireball in the central region (the region perpendicular to the beam axis). The kinetic energy deposited in the system is converted to hadrons via quark, anti-quark pair production. At this stage, the net baryon density is zero, therefore we call this a transparent collision.

The rapidity y for a particle with 4-momentum vector is defined as,

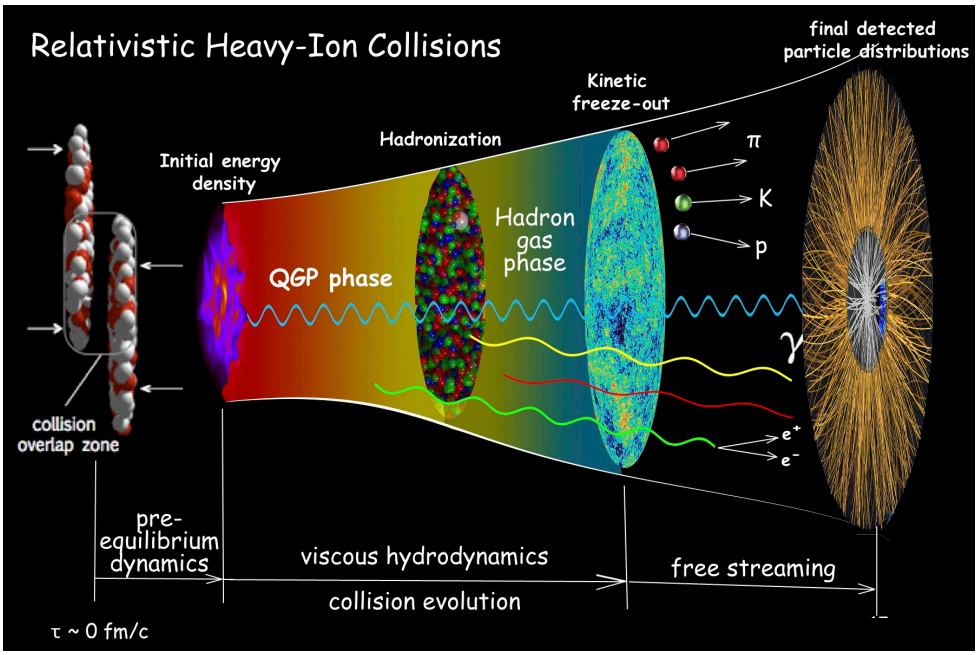

Figure 1.10: Schematic view of the various stages of a heavy-ion collision [180].

$$y = \frac{1}{2} ln \left(\frac{E + p_z}{E - p_z} \right) \tag{1.2}$$

where E is the total energy and p_z is the momentum along beam direction (z-direction) in CM the frame. This differs slightly from the definition of rapidity in special relativity, which uses $|P|$ instead of p_z. Pseudorapidity depends only on the polar angle of the particle's trajectory, and not on the mass of the particle. At relativistic speeds, the rapidity can be approximated by pseudo-rapidity η, which is widely used in all 2D di-hadron correlation studies.

$$\eta = -ln(tan(\theta/2)) \tag{1.3}$$

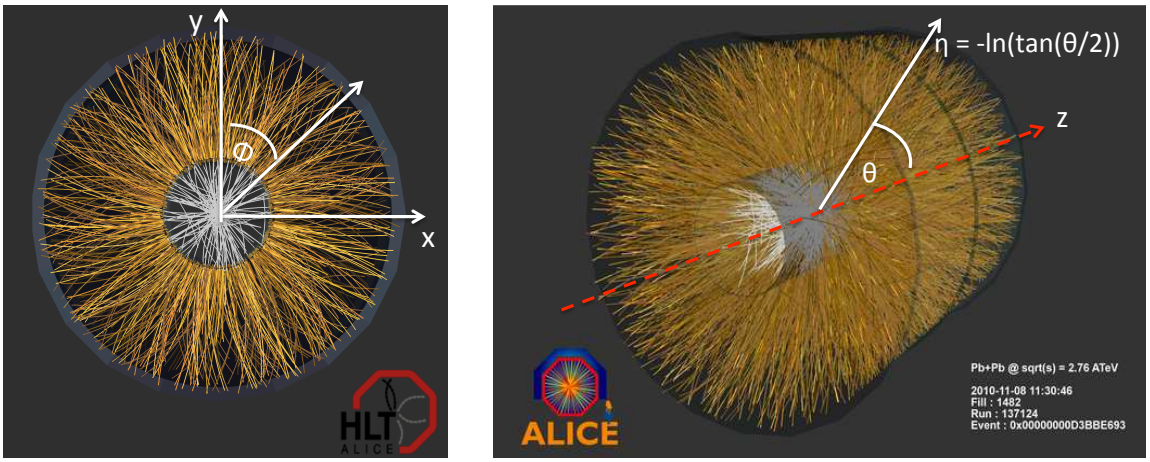

Figure 1.11: Left panel: Shows the azimuth angle as defined in the ALICE detector. Right panel: Shows the angle θ with respect to the beam direction which is used to define the pseudo-rapidity [181].

Assuming thermalization of the medium formed in a collision at the proper time τ at origin (t, z) = (0, 0), the energy density in the central region is calculated according to Bjorken, [23] as;

$$\varepsilon(\tau) = \frac{1}{\tau A}\frac{dE_{\perp}}{dy} \mid_{y=0} \tag{1.4}$$

In the equation 1.4, the area perpendicular to the beam direction (z direction) or transverse area of colliding nuclei is given by **A** and the transverse energy per unit of rapidity is given by the derivative term. Considering central collisions at the Super Proton Synchrotron (SPS) at CERN, by approximating the thermalization at τ = 1fm/c, the energy density can be calculated by the equation 1.4 as, 3 GeV/fm^3. According to lattice QCD predictions in Figure 1.8 3 GeV/fm^3 corresponds to a temperature of the order of 210 MeV, which is sufficient to create the QGP. It is likely

that at the SPS energies the lifetime of the plasma was too short to manifest into unambiguous signals of a new phase of matter. At RHIC the achievable energy density according to Bjorken was 1-10 GeV/fm^3, which then resulted in more convincing evidence of the QGP.

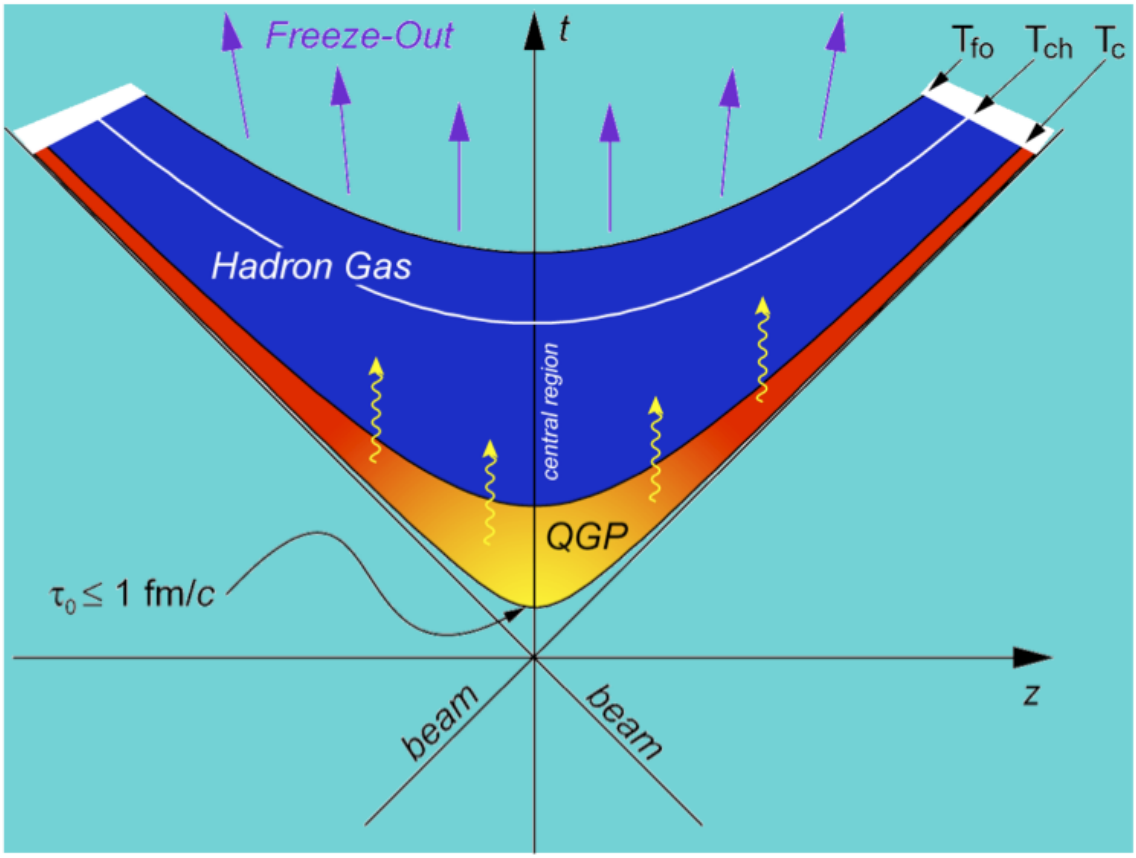

Figure 1.12: Time evolution of the collision system. T_c, T_{ch} and T_{fo} denote the critical temperature, the chemical temperature and the freeze out temperature respectively.

The time evolution of a heavy-ion collision on the light cone is shown in figure 1.12. Two energetic nuclei are traveling along the light cone and collide to create a multi-parton system. Due to the excess pressure built in the initial multi-parton

system with respect to the surrounding vacuum, the system expands. When the system temperature reaches T_c, the system will start forming hadrons (hadronization). Understanding the mechanism of hadronaization is one of the primary goals of the heavy-ion program. The majority of these hadrons are pions. These hadrons will further collide inelastically until the measured particle yields are fixed at a certain temperature. We call this the chemical freeze out (T_{ch}) temperature. The system further expands via elastic collisions until the particles do not re scatter anymore. This is called thermal freeze out (T_{fo}) and from here the hadrons will free stream towards the detectors. The detected hadrons should reveal the conditions inside the fireball.

1.4 QGP signatures at LHC

1.4.1 The energy lost in the medium

One of the ways to study the medium is to measure the partonic energy-loss in the system. By stating the analogy to ionization loss of charged particles in ordinary matter, Bjorken proposed [11], that the collisional energy loss dE/dx of the high energy quarks and gluons in nuclear collisions should carry information of the medium. Further studies revealed that the energy loss due to scattering is too small or negligible compared to energy loss due to radiation of the partons in the medium [12-14]. If we have achieved the deconfinement of quarks and gluons, the energy loss can be

attributed to the gluon density in the medium [15]. Thus a large energy loss measurement can be treated as an indirect signature of de-confinement of quarks and gluons.

1.4.2 Suppression of inclusive hadron spectra

In order to study the partonic energy loss of the medium created in relativistic heavy-ion collisions, we compare between the particle spectra of the systems where we expect (e.g., heavy-ions) and do not expect medium formation (e.g., p+p collisions). One direct comparison quantity is known as the nuclear modification factor R_{AB}. Here we compare the transverse momentum spectra of produced charged particles in Pb + Pb and p+Pb collisions to p+p reference collisions. In p + p and p + Pb systems we do not expect the high density medium formation. The nuclear modification factor is defined as follows.

$$R_{AB}(p_T) = \frac{\sigma_{pp}.d^2\sigma^{AB}/dp_T d\eta}{< N_{bin} > .d^2\sigma^{pp}/dp_T d\eta} \tag{1.5}$$

The numerator $d^2\sigma^{AB}/dp_T d\eta$ represents the integral yield in the A + B collisions in a given p_T bin, and the denominator $d^2\sigma^{pp}/dp_T d\eta$ is the corresponding p + p yield. The coefficient $< N_{bin} >/\sigma_{pp}$ scales the p + p yield by the number of binary collisions in the Pb + Pb collisions at a given centrality (centrality measures the impact parameter). In addition to partonic energy loss, the nuclear modification factor is affected by nuclear effects such as gluon shadowing and soft partonic multiple scattering in the initial state (Cronin effect). The shadowing will reduce R_{AB}

measurement, whereas the Cronin effect would increase it.

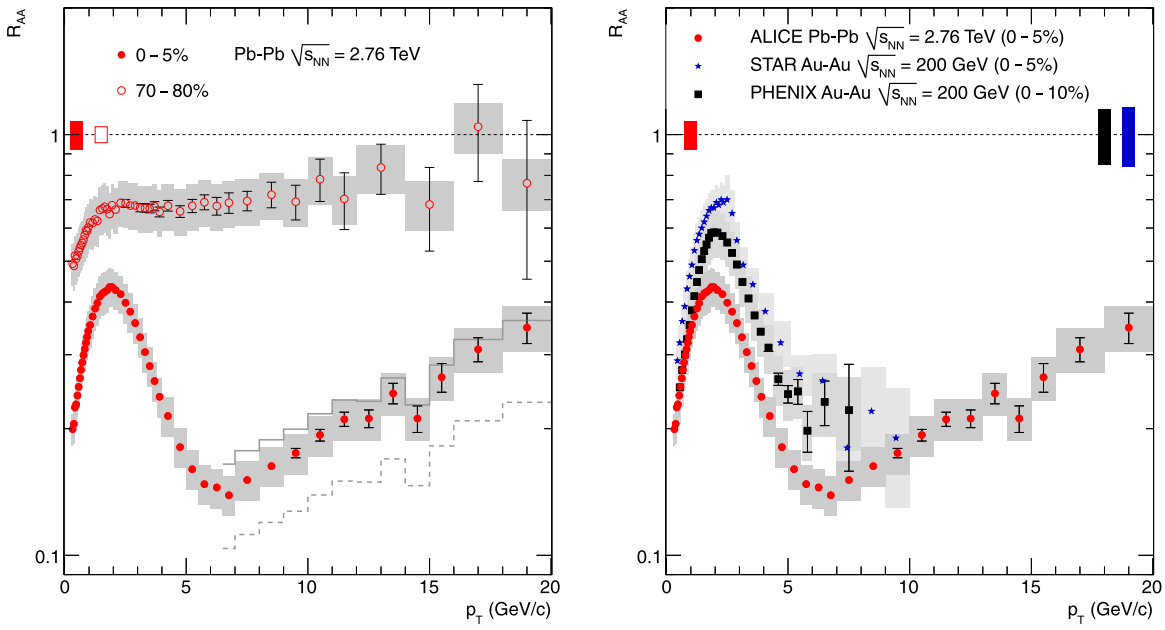

Figure 1.13: Measurement of energy loss due to the dense medium in central Pb + Pb collisions.

The left panel of figure 1.13 shows the R_{AB} measurement for the most central (refer to section 3.3.2) and peripheral Pb + Pb collisions. The dashed line at R_{AA} = 1 signifies the expected ratio if Pb + Pb collisions were only a superposition of the appropriate number of p + p collisions. As shown by fig 1.13 (left), the Pb + Pb charged particle momentum spectrum is significantly suppressed at $p_T > 2$ GeV/c. It is also observed that, only weak medium effects ($R_{AA} \approx 0.7$) are present in peripheral collisions. In central collisions, R_{AA} drops to a minimum of about 0.14 in this p_T range of 6-7 GeV/c and rises significantly at higher p_T. The right panel of fig. 1.13 shows the comparison of R_{AA} in central PbPb collisions at LHC to measurements at $\sqrt{s_{NN}}$ = 200 GeV by the PHENIX and STAR experiments at

RHIC. The measured suppression of high p_T particles is stronger than that observed at lower collision energies at RHIC, which is an indication that a higher energy density medium is formed in central PbPb collisions at the LHC. Further studies show that the observed suppression cannot be explained via hadronic interactions only [16, 17]. It requires partonic interactions and radiative and collisional energy loss in the partonic medium.

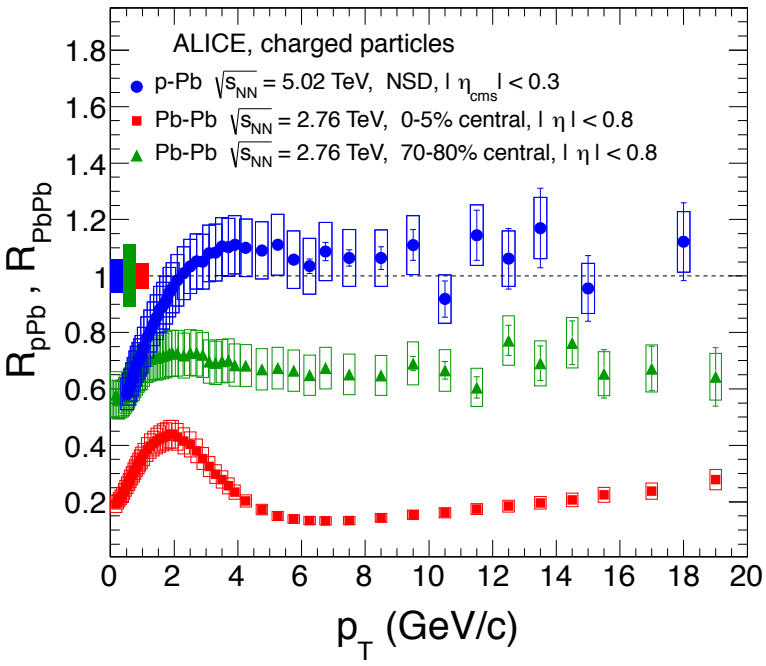

Figure 1.14: The nuclear modification factor of minimum bias p-Pb collisions at $\sqrt{s_{NN}}$ = 5.02 TeV. The data for $|\eta_{c:m:s}|$<0.3 are compared to measurements [30] in collisions at $\sqrt{s_{NN}}$= 2.76 TeV. The statistical errors are represented by vertical bars, the systematic errors by (filled) boxes around data points[26] .

The R_{AB} measurement for d + Au data at $\sqrt{s_{NN}}$= 0.2 TeV at RHIC shows no suppression. The initial enhancement we see of the charged particle spectra in the p_T < 2 GeV/c is explained as Cronin effect [18]. In the p-Pb system the Cronin effect is much smaller in magnitude and no enhancement is observed within the

systematics. In order to determine the suppression factor alone, one has to compare the p+Pb and Pb+Pb spectra in the region where the Cronin effect is insignificant (i.e. p_T >7 GeV/c). The comparison between the suppressions of Pb + Pb and p + Pb systems (see Figure 1.14) at p_T ≈8 GeV/c (i.e. analog to comparing with p + p) reveals a suppression of a factor of 5 between the two systems.

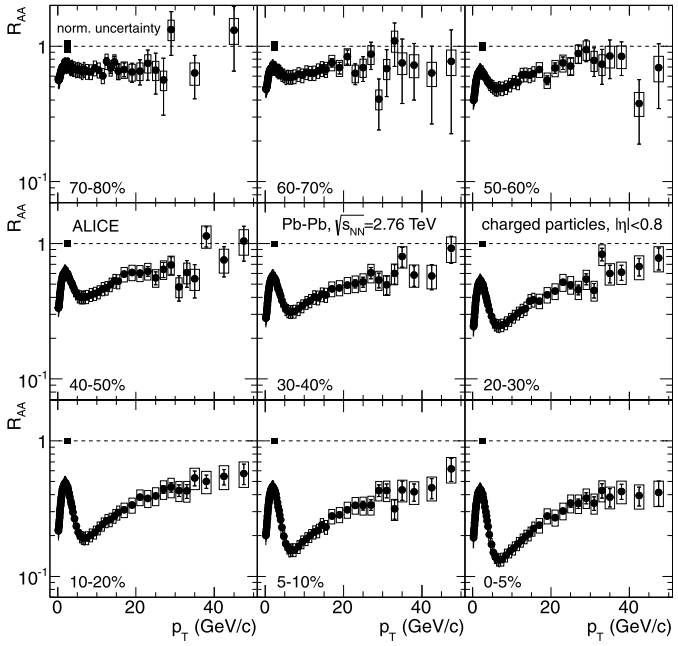

Figure 1.15: Nuclear modification factorR_{AA} of charged particles in Pb-Pb collisions at $\sqrt{s_{NN}}$= 2.76 TeV at LHC in nine centrality intervals [30].

Figure 1.15 shows the centrality evolution of R_{AA} measurement for Pb+Pb system. Despite the observed increases of R_{AA} for $p_T < 2GeV/c$ at all centralities, the results indicate a strong suppression of charged particle production in Pb+Pb and a very dense medium formation.

1.4.3 Jet-like correlations via high p_T di-hadron azimuthal correlations

One of the main particle production mechanisms in relativistic heavy-ion collisions is called jet fragmentation. In this process, collimated groups of energetic hadrons are formed due to hard scattering of high energy (high p_T) partons in the colliding system. The jets are produced within a cone (see Figure 1.16) with axis along the leading particle (highest p_T particle) in 3- dimensional space.

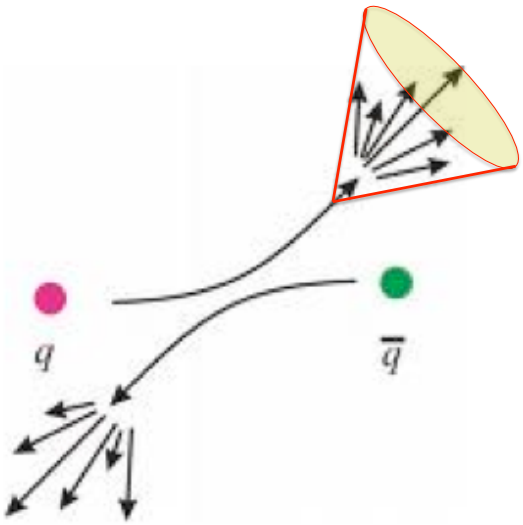

Figure 1.16: Fragmentation of a quark anti-quark pair, producing back to back jets.

The leading particles in the jet are back to back (in order to preserve the linear momentum) in the azimuthal angle ϕ (see Fig 1.16). The initial studies at RHIC energies showed that jets can be used to probe the medium [25]. Though full jet reconstruction is quite challenging due to complex background, the study of high p_T di-hadron correlations provide an additional insight into partonic energy loss in the medium.

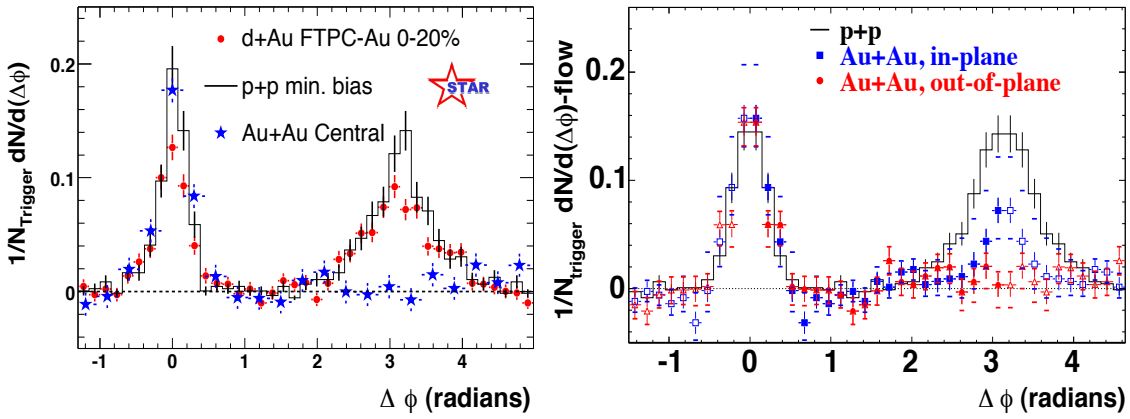

Figure 1.17: Relative angle distribution for high p_T di-hadrons at $\sqrt{s_{NN}} = 200$ GeV. Left: p + p, d + Au and central Au + Au collisions. Right: trigger particle in or out of reaction plane in non-central Au + Au collisions [19].

Figure 1.17 represents the associated yield of hadrons vs. the relative azimuthal angle:

$$\frac{1}{N_{trigger}}\frac{dN}{d(\Delta\phi)} = \frac{1}{N_{trigger}}\frac{1}{\varepsilon}\int d(\Delta\eta)N(\Delta\eta,\Delta\phi) \tag{1.6}$$

where ε is the tracking efficiency and $N_{trigger}$ is the number of leading (trigger) particles. N$(\Delta\eta,\Delta\phi)$ denotes the number of hadron pairs with relative azimuth $\Delta\phi$ (azimuthal angle difference between the two tracks) and relative pseudo-rapidity (angle relative to the beam direction) $\Delta\eta$ (see Figure 1.11). The trigger particle is selected in the momentum range $p_T^{trig} > 4GeV/c$. The trigger particle is taken as the jet axis and particles (associated particles) relative to the jet axis are selected the momentum range $2 < p_T < p_T^{trig}$ to form $\Delta\phi$ pairs. The resulting correlation structure is shown in Figure 1.17 for different systems. Due to the procedure the correlation technique is known as a triggered correlation analysis.

In Figure 1.17 left panel, we observe an approximate similarity on the near side ($\Delta\phi \approx 0$) for all the systems; p + p, d + Au and Au+Au. The absence of the away side ($\Delta\phi \sim \pi$) correlation in Au + Au compared to the other two systems thus indicates a strong suppression of the recoiling jet. The selected trigger particle is likely emitted near the medium surface on the same side and has this traversed less distance in the medium. On the other hand, the recoiling jet has to go through the dense medium of the fireball. This geometrical bias plays an important role in high p_T di-hadron azimuthal correlations. The result shown in the right panel of fig 1.17 is from a similar di-hadron analysis based on non central Au + Au collisions. The reaction plane (fig 1.18 x-z plane) of the nuclear collision has been used to calculate the in- plane and out of -plane yields. The difference between in-plane and out of plane(see fig. 1.18) in figure 1.17 is a clear indication of the path length dependence of the energy loss.

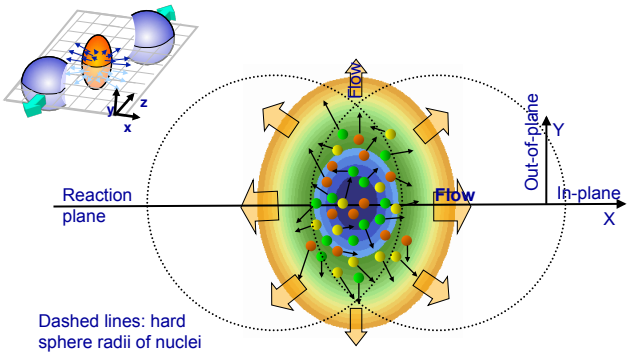

Figure 1.18: A typical non central collision of two heavy nuclei. Along the z axis is the beam direction and x-z is the reaction plane.

The azimuthal correlation approach we discussed so far can be extended into a two-dimensional ($\Delta\eta$, $\Delta\phi$) correlation analysis. Fig 1.19 presents the result obtained

for a two-dimensional correlation analysis for high p_T charged hadrons. The top panel shows p + p data, the bottom is obtained from central Au + Au collisions. In both cases a jet-like correlation is observed at $\Delta\eta$, $\Delta\phi \approx 0$. Correlations on the away side are also apparent for both cases with a broadening along $\Delta\eta$. An additional correlation structure in central Au + Au is observed at ($\Delta\phi \approx 0$) and long-ranges in pseudo-rapidity (large $\Delta\eta$).

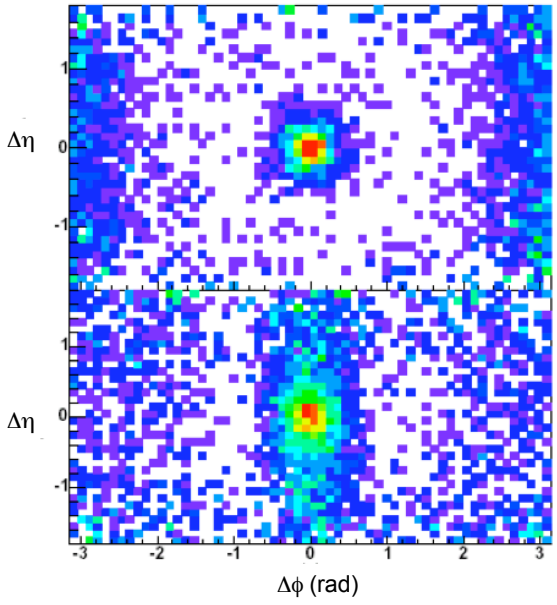

Figure 1.19: Two-dimensional ($\Delta\eta$, $\Delta\phi$) charged dihadron correlation functions from minimum bias p + p (top) and central Au + Au (bottom) collisions at $\sqrt{s_{NN}} = 200$ GeV with $3 < p_T^{trig} < 6 GeV/c$ and $2 < p_T^{assoc} < p_T^{trig}$.

It was observed in the early studies, that the long-range $\Delta\eta$ component is uniform within the detector acceptance $|\eta| < 1$ and is distinguishable from the jet-like peak. The jet-like correlations structures are similar in central Au + Au and p + p collisions for high- momentum particles ($p_T^{trig} > 6$ GeV/c) where as low-momentum (p_T^{trig}) particles exhibit medium modified broadening of the jet [25]. The same side

long-range correlations for soft hadrons ($p_T < 2GeV/c$) were also studied [22]. The physics behind the long-range correlation structure has not been resolved yet. One of the goals of my dissertation is to attempt to understand the long-range correlation phenomena .

1.4.4 Flow and viscosity: perfect fluid

In non-central heavy-ion collisions the initial volume of the interacting system is anisotropic in coordinate space (see Figure 1.18). If the system behaves collectively and can be described by fluid dynamics or multi-parton exchanges, the initial spatial anisotropy is transferred to momentum anisotropy. The momentum space can be quantified via a Fourier decomposition and known as flow harmonics v_n [61]. Estimation of flow harmonics is carried out with different analysis techniques. In this thesis work, the method of di-hadron correlations will be used to measure the v_n s.

Before the RHIC heavy-ion results, scientists thought that the increase of energy density would lead to a weakly interacting QGP (similar to ideal gas). Surprisingly, the RHIC results indicated strong jet quenching effects and flow signals of light and heavy quarks. In other words, the QGP at RHIC was strongly interacting. In order to measure the strength of interaction in fluid systems there exists a well-defined quantity. It is the ratio of the shear viscosity η (a measure of the mean free path of particles) and its entropy density s (measure of the inter-particle distances). The ratio can be used to characterize how close a given fluid is to being perfect. Studies

by Son et al. [27] indicated that, there exists a lower viscosity bound $\eta/s > 1/4\pi$ applicable for all quantum systems. The most common examples of very low viscosity (or near-perfect) fluids which are referred to as superfluids are shown in Figure.1.20. The viscosity bound (quantum limit = $\eta/s > 1/4\pi$) is shown by the red line at the very bottom.

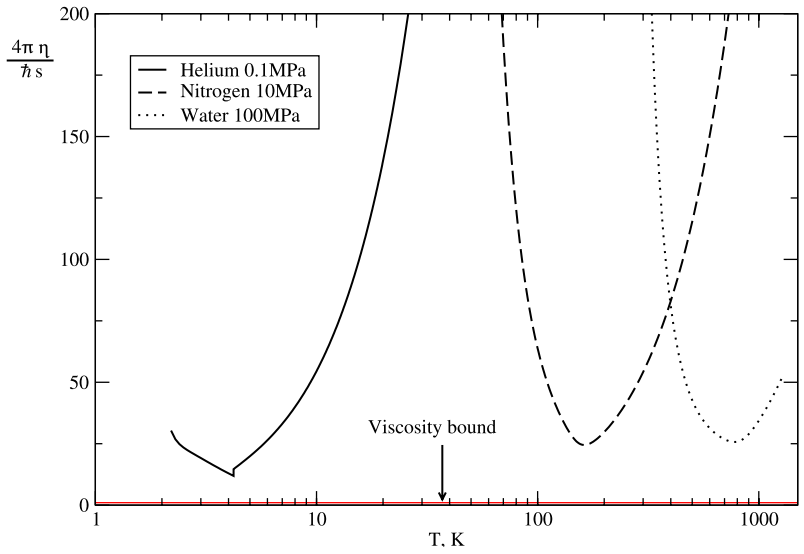

Figure 1.20: The shear viscosity to entropy density ratios (η/s) divided by the conjectured lower bound as a function of temperature in Kelvins. Shown are curves for helium, nitrogen and water.

The specific shear viscosity $(\eta/s)_{QGP}$ of the quark-gluon plasma (QGP) can be extracted from v_n data in heavy-ion collisions by comparing them to dynamical models. These models [104,105] can predict the v_n values for a given (η/s) value.

Figure 1.21 shows the theoretical (based on MC KLN model [29]) and experimental values for v_2 as a function of centrality. For RHIC data, $(\eta/s)_{QGP} = 0.16$ gives a better description for experimental results whereas $(\eta/s)_{QGP} = 0.2$ describes the LHC data. In order to measure (η/s) accurately we need both theoretical and

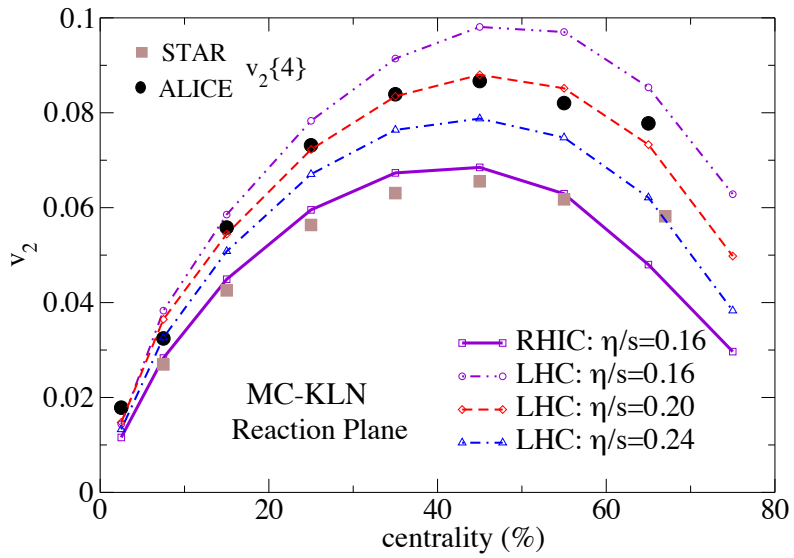

Figure 1.21: Total charged hadron elliptic flow (v_2 is the second Fourier harmonics) as function of centrality (measure of impact parameter or how violent the collision is) for LHC at $\sqrt{s_{NN}} = 2.76$ TeV Pb-Pb and RHIC at $\sqrt{s_{NN}} = 0.2$ TeV Au-Au data

experimental v_n values with high precision. In this thesis work, I will attempt to measure the experimental v_ns (upto higher order v_5) with better precision and purity.

1.4.5 Dissertation outline

In the second chapter we introduce the experimental facility, the Large Hadron Collider (LHC) at CERN accelerator complex. All stages of ion acceleration will be discussed. Next, we explain the ALICE detector and its sub detector components and their principles of operation in detail. In chapter three we discuss the physics of the di-hadron correlations. The main part of chapter four describes the di-hadron

correlation formalism and derives the correlation measurement we apply, while discussing the relation between fluctuations and correlations. The correction procedure to the correlation measure and the fitting procedure of the model is also included in this chapter. Chapter five reports the results from our model studies. In chapter six we discuss the study of systematic uncertainty estimations and present the final results. In the final chapter, we summarize and discuss the experimental findings and implications related to understand the de-confined state of matter and its medium properties.

Chapter 2

The ALICE experiment at LHC

In the quest of understanding nature at the smallest scale, accelerators have become indispensable. Accelerated beams were first produced by Crooks with his cathode ray tube experiments. At the time, the acceleration of a beam of electrons was achieved by applying DC voltage. In 1909 Geiger and Marsden, under the supervision of Ernest Rutherford, performed the historical gold foil experiment, known as Rutherford scatting experiment, with beams of α particles. The discoveries from the Rutherford experiment revolutionized the understanding of the subatomic structure. Meanwhile Louse De Broglie introduced his "De Broglie Hypothesis". The relation λ = h/p predicts that highly energetic particles (large momentum p) give finer resolution (small λ) when probing a target, where h is the Plank's constant ($6.626068 \times 10^{-34} Js$). Thus, acceleration of particles to higher momentum (or energy) became an essential task, which was first accomplished by Cockcroft and Walton (won Noble price for physics in 1951) with their circuit design and generator in

1932. Due to the limitations of the DC voltage acceleration procedure, the cyclotron was introduced by Leo Szilard and Ernest Lawrence in 1932. The cyclotron uses an AC-generated electric field and a static magnetic field to accelerate particle beams. In order to overcome the limitations of cyclotron operation at relativistic speeds, synchrotrons were introduced. In a synchrotron accelerator, bending, beam focusing and acceleration can be separated into different components. Unlike AC-generated electric fields in cyclotrons, synchrotrons are designed with Radio Frequency (RF) cavities to accelerate particles. The concept of the synchrotron, laid the foundation to the design of large scale facilities. In order to achieve higher center of mass (CM) energy systems, collider experiments are being used in modern particle physics laboratories. Today, the Relativistic heavy-ion Collider (RHIC) at Brookhaven National Laboratory (BNL), Upton, New York and the Large Hadron Collider (LHC) at CERN, Geneva, Switzerland are the most powerful particle accelerators in the world.

2.1 The Large Hadron Collider - LHC

In the 1990's the Super Proton Synchrotron (SPS) at CERN and the Alternating Gradient Synchrotron (AGS) at BNL started a new era in the search for signatures of the Quark-Gluon Plasma (QGP). In order to search for more signatures of the QGP, even higher energy densities were required. A new machine called the Relativistic Heavy-Ion Collider (RHIC) at Brookhaven National Laboratory was completed in 2000 to create such energy densities. Compelling evidence for the existence of the

QGP was observed at RHIC and turned a new page in heavy-ion physics. Until the year 2009, RHIC was the most powerful and versatile particle accelerator in the world. In 2009 the Large Hadronic Collider (LHC) at CERN was commissioned, reaching even higher (14 times) CM energies. The heavy-ion physics program at the LHC searches for new physics at the TeV scale while further investigating the findings of RHIC. Figure 2.1 shows an arial view of the CERN accelerator complex.

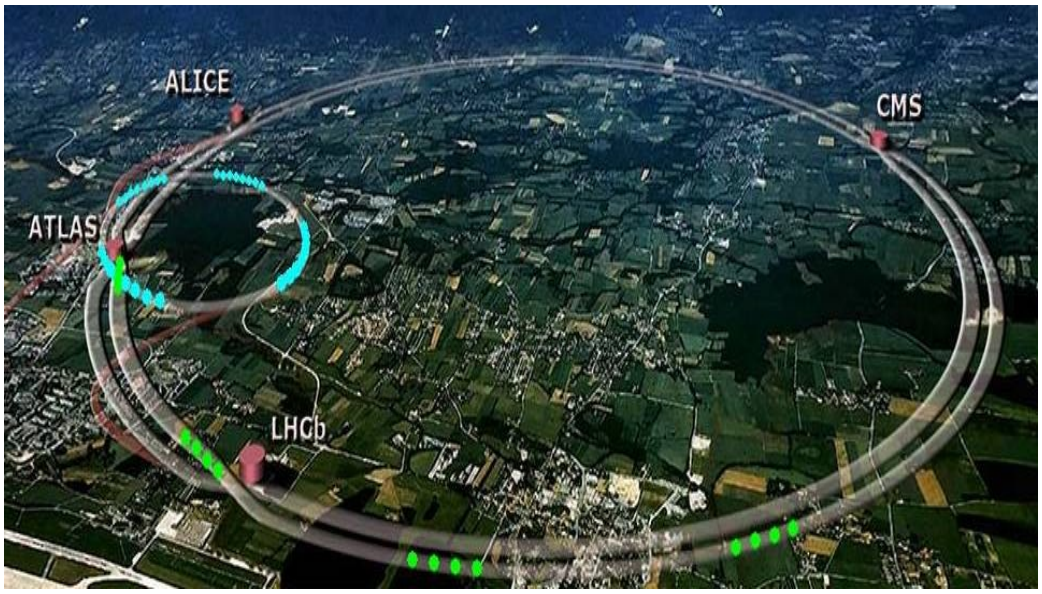

Figure 2.1: An arial view of the LHC Accelerator Complex [168]. The locations of four main experiments ALICE, ATLAS, CMS and LHCb are also shown

Brief summary of heavy-ion accelerators

The Table 2.1 presents an overview of ultra-relativistic heavy-ion accelerators. The table summarizes the last four decades of heavy-ion collision experiments. The collision energy has increased from 2 GeV (1975) to 5.5 TeV(2007) per nucleon in the CM frame. From 2015 LHC is expected to achieve energies up to 13 TeV. The field of accelerator technology has achieved tremendous advancements during the span of four decades.

Table 2.1: History of heavy-ion physics :Experimental facilities.

Experimental Facility (time period)	Laboratory	$\sqrt{S_{NN}^{max}}$	Type
BEVLAC(1975 - 1986)	LBNL	2.0 GeV	Fixed target
SIS(1989 -)	GSI	2.4 GeV	Fixed target
AGS(1986 - 1998)	BNL	4.8 GeV	Fixed target
SPS(1986 - 2003)	CERN	17.3 GeV	Fixed target
RHIC(2000 -)	BNL	200 GeV	collider
LHC(2007 -)	CERN	5.5 TeV	collider
FAIR(2014 -)	GSI	8 GeV	Fixed target
LHC(2015 -)	CERN	13 TeV	collider

The Large Hadron Collider is capable of producing both symmetric (p+p or Pb+Pb) and asymmetric collisions (p+ Pb). Asymmetric collisions are useful for distinguishing the effects of cold nuclear matter (modification of the initial state in a nucleus) versus hot nuclear matter (such as a QGP). The following paragraphs discuss in detail the individual components of the LHC complex.

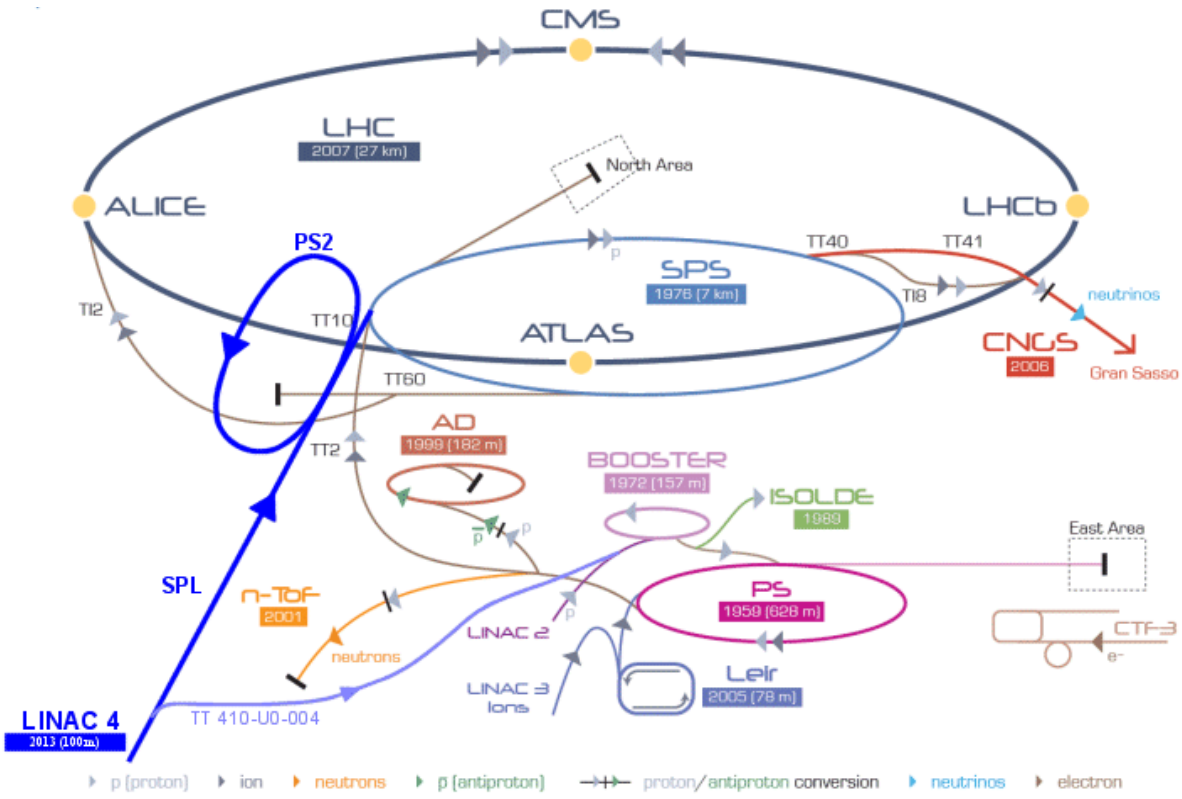

Figure 2.2: Perspective view of the LHC complex at CERN. The subsystems PS, SPS, LEIR, LINAC, Booster and four experiments are also indicated at the interaction points.

2.2 CERN accelerator complex

Figure 2.2 shows general details of the LHC complex and acceleration procedure. For example, p+p acceleration begins with Linac 2 and then goes through the Proton Synchrotron Booster before entering the Proton Synchrotron (PS). After accelerating through PS, the beam is injected to SPS and finally to LHC. The heavy-ion acceleration begins with Linac 3 and enters the Low Energy Ion Ring. Then the ion beam enters PS,SPS and LHC successively. In the following subsections, we will discuss the main acceleration subcomponents at the LHC complex. Those are: LINAC, PS

Booster, LEIR, PS, SPS, and the LHC.

2.2.1 The linear accelerators at CERN - Linac 2,3

The starting point of the proton beam of the LHC is the linear accelerator 2 (Linac 2) which started its operations in 1978. The Proton source is a bottle of hydrogen gas at one end of Linac 2. The hydrogen is passed through an electric field to strip off its electrons, leaving only protons to enter the accelerator. The protons pass through the cylindrical conductors, which are charged positively and negatively periodically. The acceleration of protons is caused by the push and the pull from the positively and negatively charged conductors kept at radio frequency. By the time they reach the other end of the conductor chain, the protons have reached an energy of 50 MeV and gained 5% in effective mass. In order to squeeze the beam, small quadrupole magnets are used. Then the beam is injected into the Proton Synchrotron Booster.The proton beams are pulsed from the hydrogen bottle for up to 10^{-4}s per pulse. The pulses are repeated until reaching the required luminosity. Linac 2 will be superseded by Linac 4 in 2017 /18.

Linear accelerator 3 (Linac 3) is the starting point for the ions used in experiments at CERN. It provides lead ions for the Large Hadron Collider (LHC) and for fixed-target experiments. Linac 3 was built to provide ions to study the quark gluon plasma. In the past, linac 3 provided ions to the Proton Synchrotron Booster. It now injects lead ions into the Low Energy Ion Ring, which prepares them for injection into the LHC complex. The accelerated Pb ions from Linac 3, are sent through a

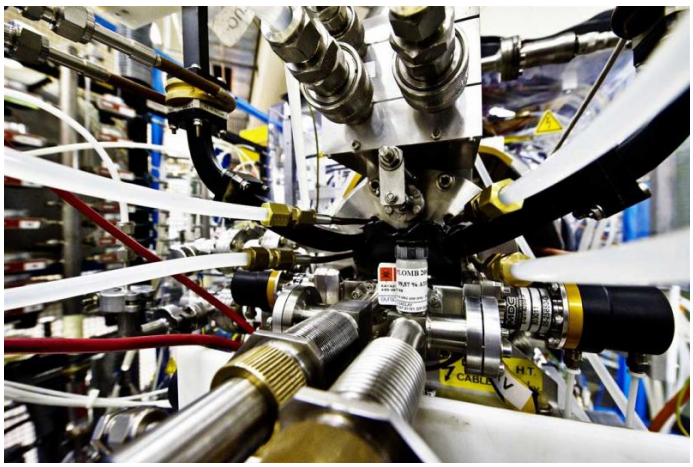

Figure 2.3: The ion source of the linac3: the starting point of the ion beam of LHC

stripping foil to transform Pb to Pb^{54+}. Linac 3 uses up about 500 milligrams of lead per two weeks of operation. Linac 3 is expected to be in use until at least 2022.

2.2.2 The Proton Synchrotron Booster

The Proton Synchrotron Booster is made up of four superimposed synchrotron rings of 157 m circumference. Figure 2.4 shows a graphical view of the PS Booster which receives beams of protons from the linear accelerator Linac 2 at 31.4% of the speed of light and an energy of 50 MeV. The original beam from linac2 is spilt into four beams and further accelerated to 91.6% of the speed of light and then squeeze into packets. The packets from four rings (with energy of 1.4 GeV) are recombined and injected into the Proton Synchrotron (PS).

Before the construction of the Booster in 1972, protons were injected directly from the linac into the PS. The number of protons the PS could accept was limited due to the low injection energy of 50 MeV. The Booster has increased the acceptance

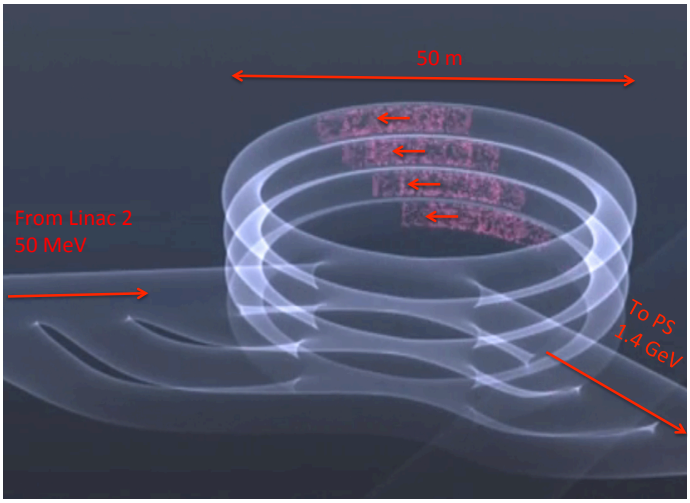

Figure 2.4: A graphical view of the Proton Synchrotron Booster rings.

of PS by two orders of magnitude. Consequently, the beam's use for experiments has enhanced significantly.

2.2.3 The Low Energy Ion Ring (LEIR)

The Low Energy Ion Ring (LEIR) receives long pulses of lead ions from Linac 3, then transforms them into the dense, short bunches for injection to PS, SPS and finally the Large Hadron Collider. LEIR splits each long pulse from Linac 3 into four shorter bunches, each containing 2.2×10^8 lead ions. The LEIR accelerates the bunches (with charge Pb^{54+}) from 4.2 MeV to 72 MeV in 2.5 seconds. Then the ions are at an optimal energy to be injected to the Proton Synchrotron (PS). The LHC uses 592 bunches (each bunch with 9×10^7 lead ions) of ions per beam, so it takes around 10 minutes for LEIR to provide enough for a complete fill. In 2006 and 2007 LEIR was being used to re-commission the PS and SPS to handle ions. Finally, in

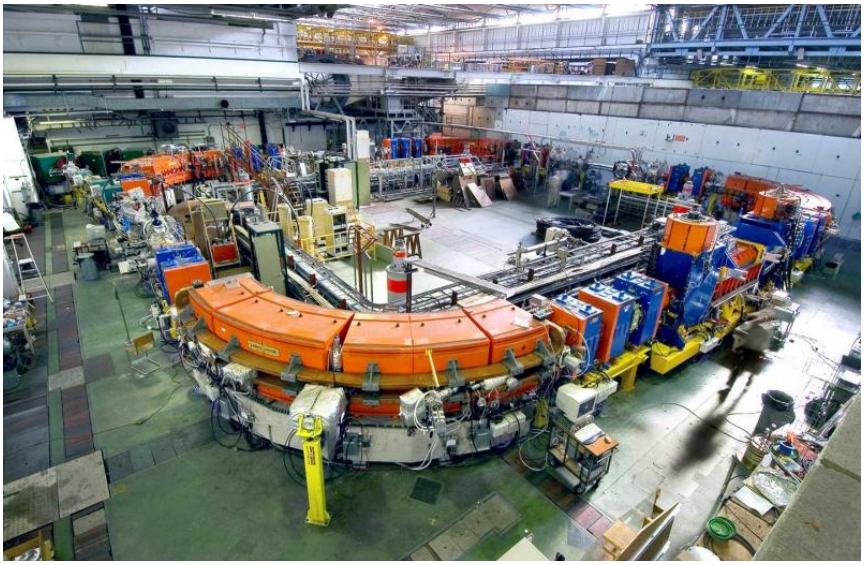

Figure 2.5: The Low Energy Ion Ring facility at CERN

November 2010, the Low Energy Ion Ring provided the lead ion beam for LHC for the first time.

2.2.4 The Proton Synchrotron (PS)

The Proton Synchrotron (PS) is a key accelerator in CERN's accelerator complex. Despite the name, the Proton Synchrotron is capable of accelerating heavy-ions from the Low Energy Ion Ring (LEIR) and protons delivered by the Proton Synchrotron Booster. Figure 2.6 shows the schematic view of the Proton Synchrotron. With a circumference of 628 meters, the PS is composed of 277 conventional (room-temperature) electromagnets, including 100 dipoles to bend the beams around the ring. The ion beam from LEIR is accelerated to 5.9 GeV and proton beams from PS Booster (entering with 1.4 GeV) are accelerated up to 25 GeV. After extraction

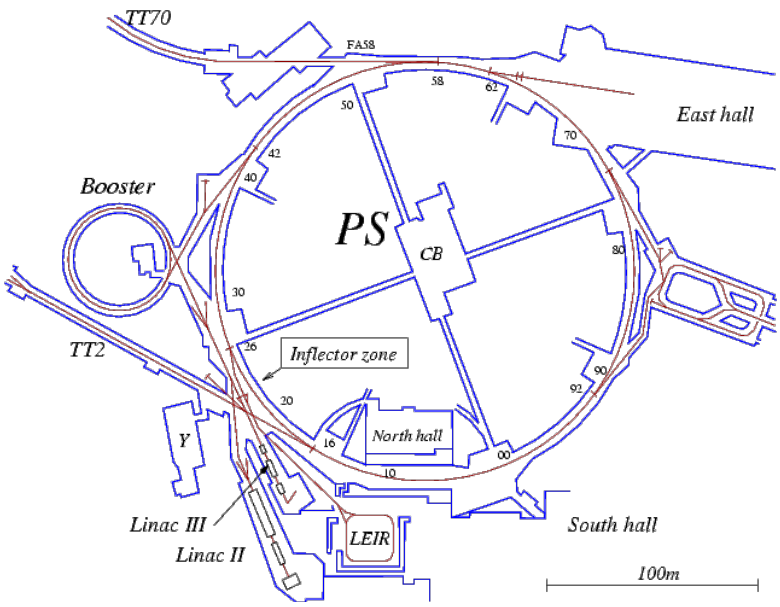

Figure 2.6: The schematic view of Proton Synchrotron

from the PS, the Pb^{54+} beam is fully stripped to Pb^{82+} by using a 0.8 mm aluminum foil.

The PS first accelerated protons in 1959, becoming the world's highest energy particle accelerator for a short period time. The PS was CERNs first synchrotron and was its flagship accelerator. The introduction of new accelerators in the 1970s changed the role of the PS, which became to supply particles to the new machines. Over five decades, it has undergone many upgrades and modifications. The intensity of its proton beam has increased by three orders of magnitude. Since 1959, the PS has accelerated many different kinds of particles for experiments or passed to more powerful accelerators (SPS), such as protons, alpha particles, oxygen,sulphur nuclei, electrons, positrons and antiprotons. Furthermore, the PS provides beams to test detector prototypes for future detector upgrade projects.

2.2.5 Super Proton Synchrotron (SPS)

Figure 2.7: Inside the Super Proton Synchrotron tunnel

The Super Proton Synchrotron (SPS) is the second-largest accelerator in the CERN complex. Measuring 6.9 kilometers in circumference, SPS takes particles from the Proton Synchrotron and accelerates them to provide beams for the Large Hadron Collider and other smaller scale experiments. It has 1317 conventional (non-superconducting) electromagnets, including 744 dipoles to bend the beams around the ring. The SPS accelerates proton beams from 25 GeV to 450 GeV (99.9998% of the speed of light) and lead beams from 5.9 GeV to 177 GeV.

When the SPS was commissioned in 1976, it became the workhorse for the particle physics program at CERN. The Nobel Prize-winning discovery of W and Z particles in 1983 was the major highlight (1983) of the SPS while running as a proton-antiproton collider. The accelerator has also handled many different types of particles pre-accelerated through the PS.

2.2.6 The Large Hadron Collider

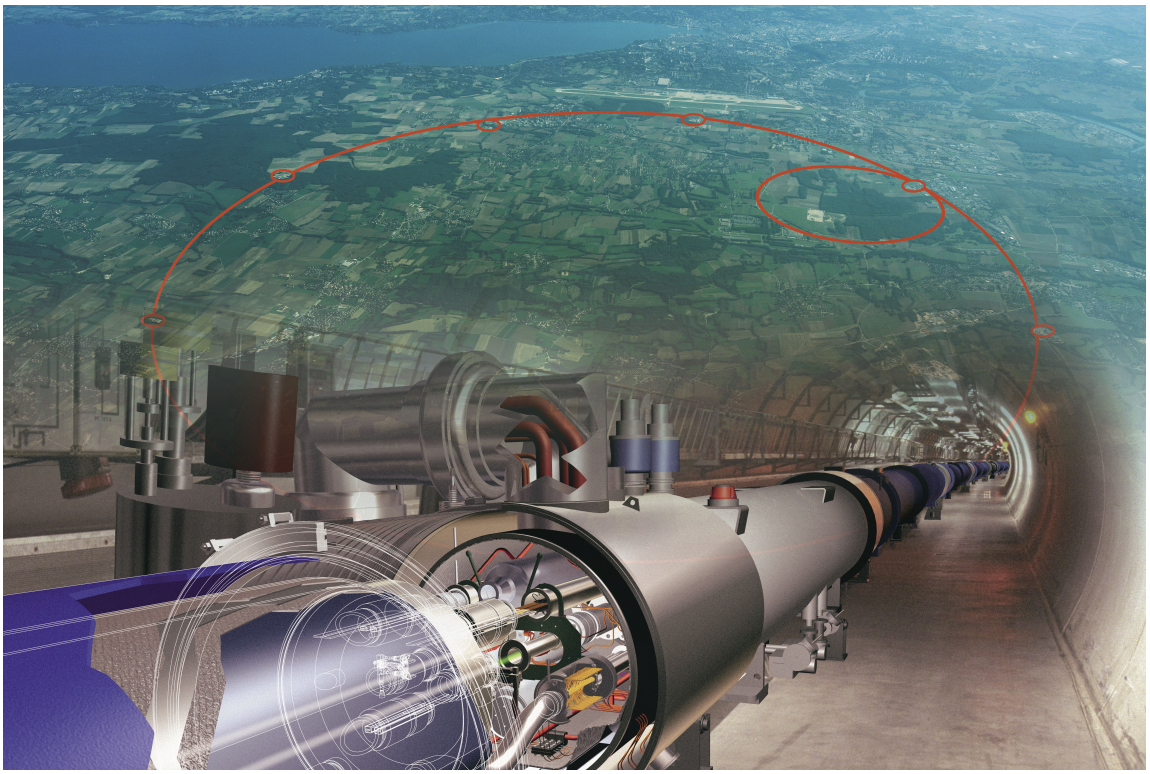

Figure 2.8: The accelerator ring of Large Hadron Collider

The Large Hadron Collider (LHC) is the largest and most technologically advanced particle accelerator in the world. It first started up on 10 September 2008, and remains the latest addition to CERNs accelerator complex. The LHC consists of a 27-kilometer ring of superconducting magnets with Radio Frequency (RF) cavities to boost the energy and storage of the particles along the way.

The LHC is not a perfect circle. It consists of eight arcs and eight insertions. Figure 2.9 shows the layout of the LHC, the LHC tunnel is made 100 m underground

and consists of eight 545 m-long straight sections, and eight 2.45 km-long arcs. Each arc section, contains 154 dipole magnets for bending the beam. The LHC is also equipped with 392 quadrupole magnets to focus the beams. The exact layout of each straight section depends on the specific use of that section, e.g., for physics experiments. Figure 2.10 shows the design of cryogenic dipole magnet and the figure 2.11 shows the testing if the modules before installing at the LHC tunnel.

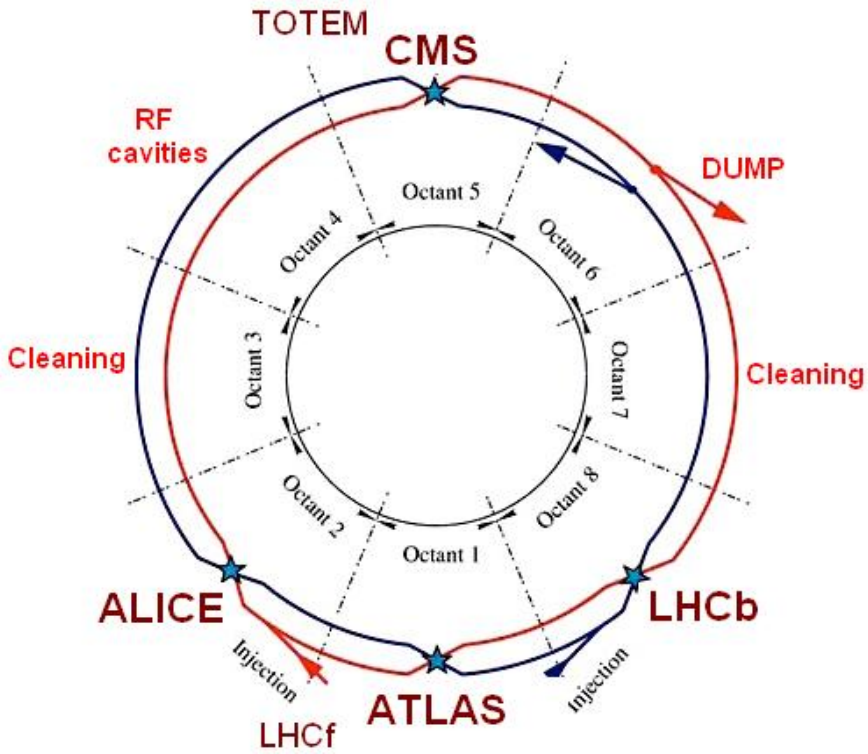

Figure 2.9: The LHC layout: The arc sections and the straight sections

The LHC design consists of two independent beams which travel at 99.9999% of the speed of light in clockwise and counterclockwise directions in separate beam pipes kept at ultrahigh vacuum. A vacuum of 10^{-13} atm is maintained in the beam pipes in order to avoid interactions between the gas molecules and relativistically moving

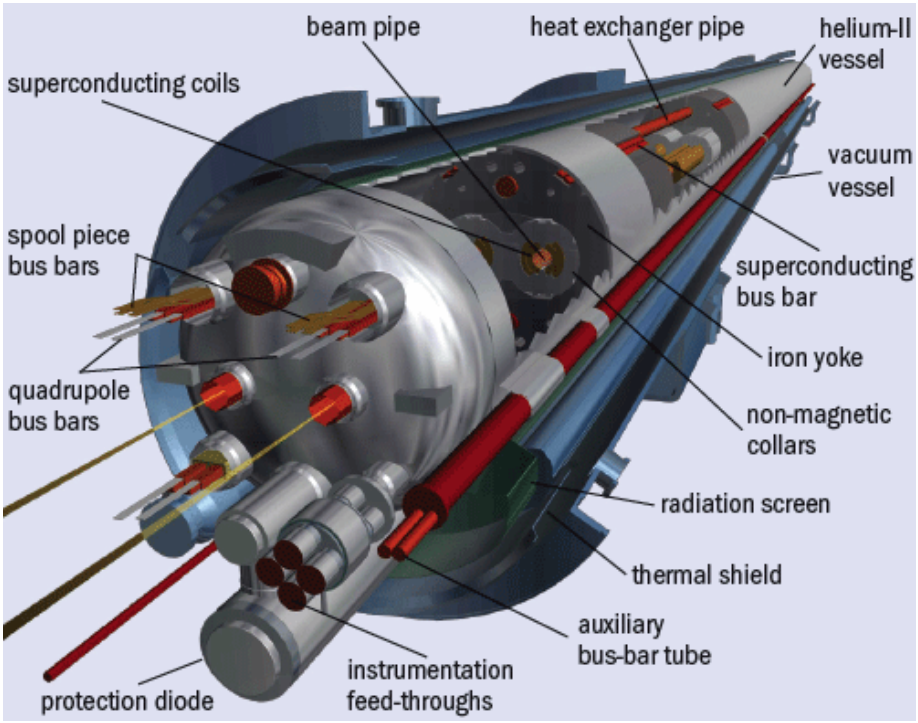

Figure 2.10: The cryodipole magnets of the LHC [182]

ions. In the curved sections, dipole magnets steer the ion beam along the curvature of the pipes. In the straight sections, quadrupole magnets guide the beam along the beam axis. All the magnets in the LHC are superconducting electromagnets. They are cooled by superfluid helium to maintain an operational temperature of 1.9 K which is even colder than outer space (2.7 K). Radio Frequency (RF) cavities with 400 MHz frequency located in the straight sections of the rings generate a high frequency electromagnetic field, which is used either to accelerate or to store the bunches of particles at each pass around the ring. In the middle of each straight section is an intersection region where the beam pipes cross, allowing the particle beams to collide. Just prior to collision, another type of magnet is used to "squeeze" the particles closer together to increase the chances of collisions. At these intersection

points, the experiments (ALICE, ATLAS, CMS and LHCb) are located. Table 2.2 lists important parameters for the LHC.

Figure 2.11: The cryodipole magnets testing before the installation at LHC

Table 2.2: Important LHC parameters

parameter name	value
Circumference	26 659 m
Dipole operating temperature	1.9 K
Number of magnets	9593
Number of main dipoles	1232
Number of main quadrupoles	392
Number of RF cavities	8 per beam
Nominal energy, protons	7 TeV
Nominal energy, ions	2.76 TeV
Peak magnetic dipole field	8.33 T
Min. distance between bunches	$\sim$7 m
No. of bunches per proton beam	2808
No. of protons per bunch (at start)	1.1×10^{11}
Number of turns per second	11245
Design luminosity	1×10^{34} cm^{-2} s^{-1}
Number of collisions per second	600 million

2.2.7 Experiments at LHC

In this section the other main experiments at the LHC will be introduced briefly. The ALICE experiment will be discussed in section 2.3 in detail including all relevent sub detector components.

CMS experiment

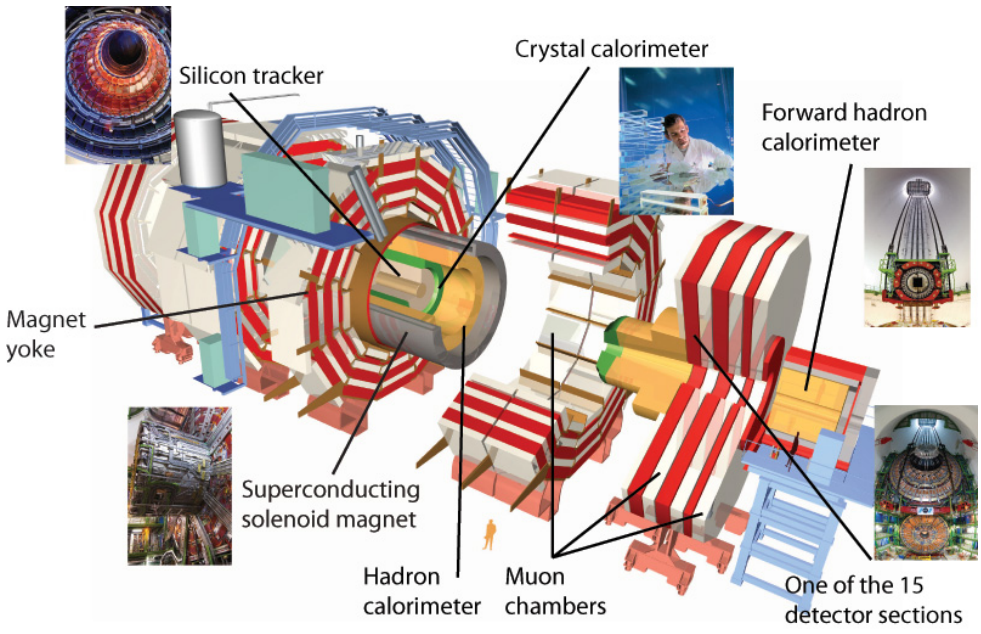

Figure 2.12: A schematic view of CMS detector at CERN [182].

The Compact Muon Solenoid (CMS) is a general-purpose detector at the Large Hadron Collider (LHC). It is designed to investigate a wide range of physics, including the search for the Higgs boson, extra dimensions, and particles that could make up

dark matter. Although it has similar scientific goals as the ATLAS experiment, it uses a quite different detector design. The Nobel prize winning discovery of the Higgs boson in 2013 was the major highlight of the CMS experiment. ATLAS confirmed the results, and the final results were reported together.

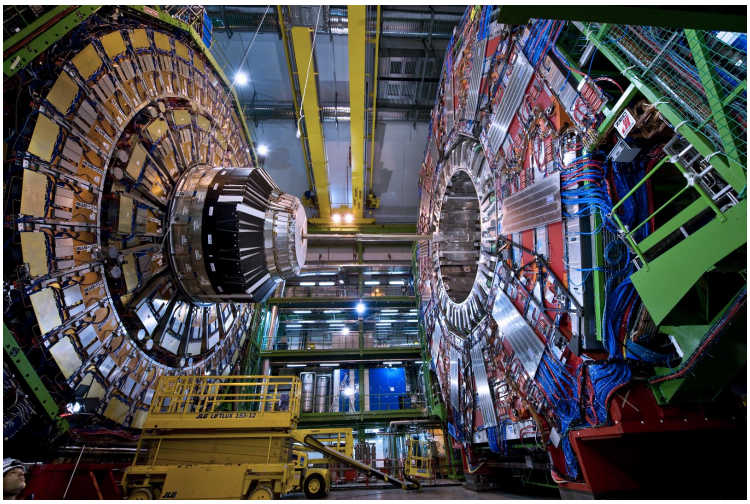

Figure 2.13: CMS detector under construction

CMS is the second largest detector built for the LHC. The detector is 21 meters long, 15 meters wide, 15 meters high and weights 12,500 tons. The CMS detector is built inside a huge solenoid magnet, which generates a magnetic field of 4 T. Figure 2.13 shows the CMS detector in the underground cavern before the final assembly.

ATLAS experiment

A Toroidal LHC Apparatus (ATLAS) is the other general-purpose detectors at LHC. And it is the largest particle detector ever built. It also investigates a wide range of

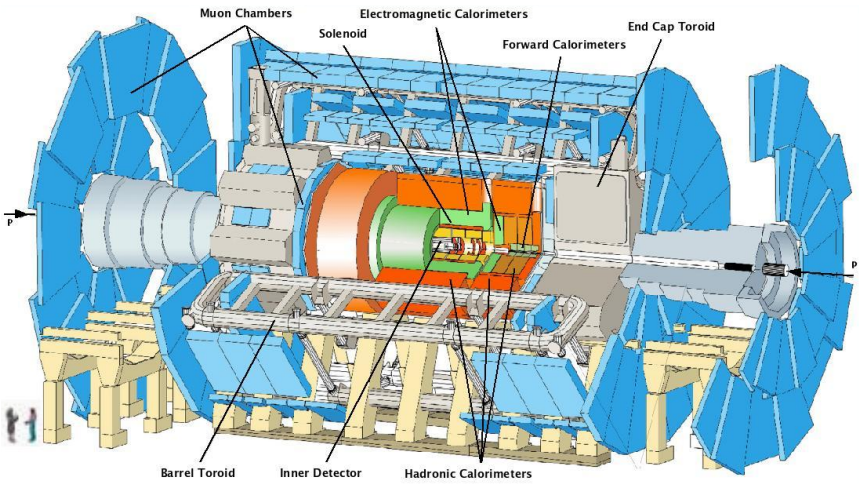

Figure 2.14: A schematic diagram of the ATLAS detector [35].

physics. The search for the Higgs boson was a primary physics goal of the ATLAS collaboration. In addition, searches for existence of extra dimensions and particles that could make up dark matter will be conducted. As of today, ATLAS experiment has confirmed the existence of the Higgs boson, which enhanced the validity of the standard model. Figure 2.14 shows the gigantic ATLAS detector. It is 46 m long, 25 m diameter and weighting 7000 tons.

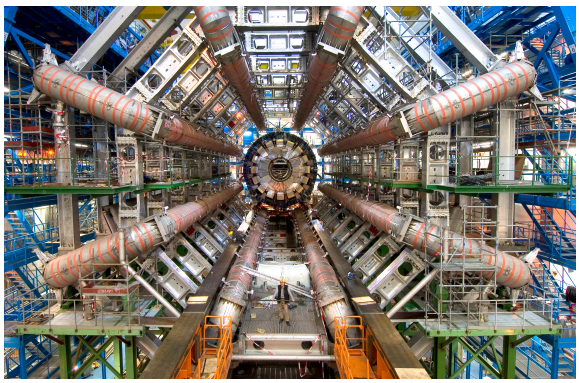

Figure 2.15: ATLAS detector under construction [35]

LHCb experiment

The Large Hadron Collider beauty (LHCb) experiment specializes in investigating the Matter-Antimatter asymmetry of the universe. The design of the LHCb detector uses a series of sub detectors to detect mainly forward particles whereas, ATLAS ,ALICE and CMS are designed to capture the complete azimuth of 2π with the collision point entirely enclosed. Figure 2.16 shows the graphical and schematic view of the LHCb detector.

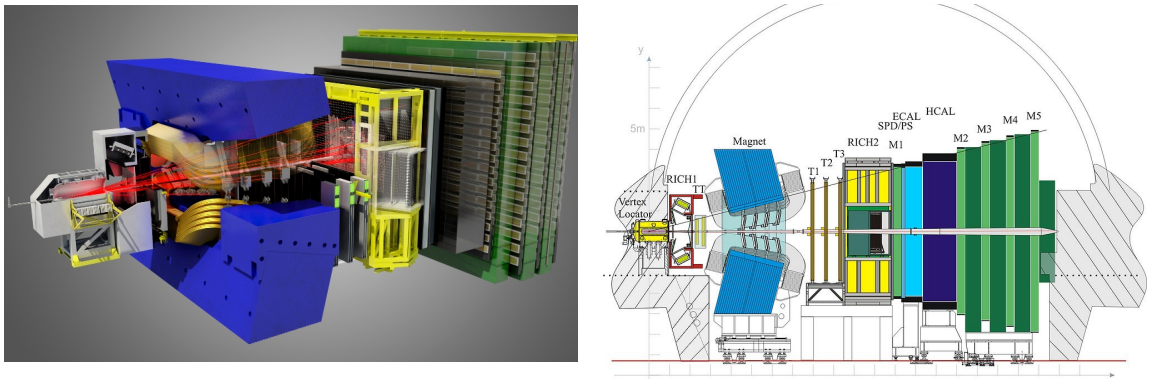

Figure 2.16: The LHCb detector design [182].

2.3 The ALICE experiment

A Large Ion Collider Experiment (ALICE) is the dedicated heavy-ion experiment to study the Quark Gluon Plasma at the LHC. Its detector components can be classified into three categories, namely tracking devices, calorimeters and particle identification devices. In this thesis work the most important sub detector components are the tracking devices.

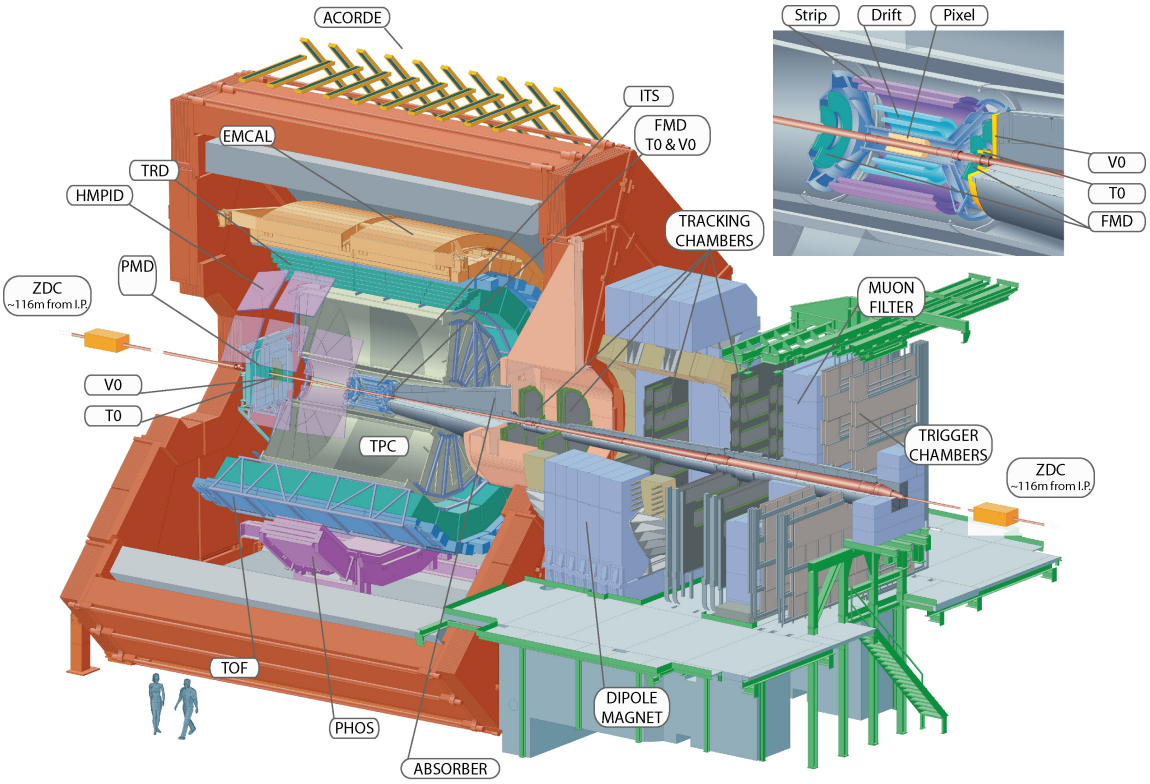

Figure 2.17: The A Large Ion Collider Experiment [183].

In the following section we discuss the ALICE tracking devices in detail. Then the calorimeters and Particle Identification (PID) devices will be introduced briefly.

2.3.1 ALICE TPC - The main tracking detector in ALICE

The Time-Projection Chamber (TPC) [29,30] is one of the most important sub systems in ALICE. It is also the main tracking device in ALICE, and the largest TPC ever constructed for a particle detector. The time-projection chamber has a cylindrical shape and is separated in two volumes by a central cathode (see Fig. 2.18). It is 5 m long (the length alongside the beam direction) and has an innermost radius of 0.85 m and outermost radius of 2.50 m. Multi-wire proportional chambers with (MWPC) cathode pad readout are mounted at each end plate into 18 trapezoidal sectors covering the complete azimuth of 2π .

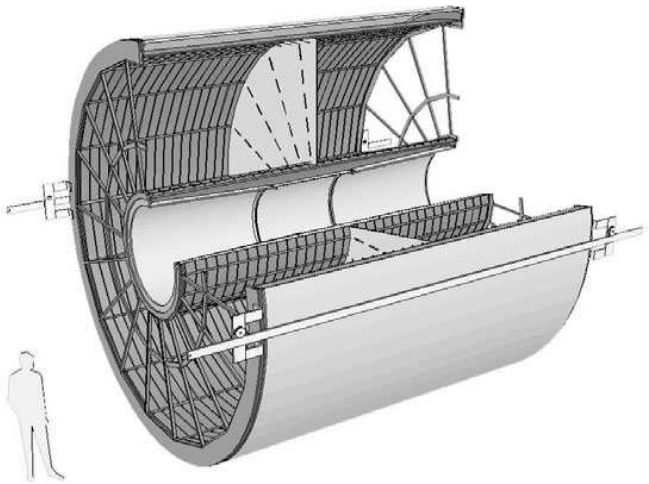

Figure 2.18: Time-Projection Chamber of ALICE [183].

The TPC is a gaseous detector filled with a 90 m^3 gas mixture of $Ne/CO_2/N_2$ (90/10/5), which is kept slightly above atmospheric pressure to prevent the entering of the atmospheric gases to the active TPC volume. The TPC gas is being ionized by the traversing charged particles, after which the liberated electrons drift towards

the end plates. The drift time (z coordinate) information together with the position of the electron cloud at the end plates (x,y coordinate) can be used to determine the 3D space points along the trajectories of charged particles.

Due to the presence of a 0.5 T magnetic field, a charged particle traversing the chamber follows a helical path. The traversing charged particle ionizes nearby atoms and liberated electrons drift towards the nearest end of the chamber at ≈ 2.7 cm/μs under the influence of a 400 V/cm electric field between the central high voltage electrode and end caps of the TPC. The cathode captures positive ions at the center while the clouds of electron drift towards the end cap. The positive ions are being neutralized at the central cathode plane. A Multi-wire Proportional Chamber (MWPC) near the end caps amplifies the electron clouds, before the electrons meet a gating grid at the end of the drift region. Beyond the gating grid, lies a proportional region, as shown in figure 2.19. If an event needs to be recorded based on the triggering criteria, the gating grid is opened (see fig. 2.19 right).

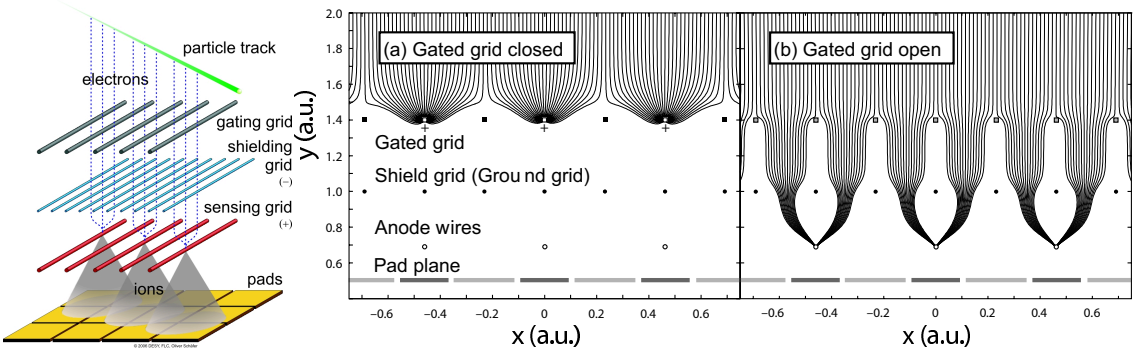

Figure 2.19: The MWPC gating procedure

The TPC pads (with Front End Cards FEC) are laid out in trapezoidal sectors

that cover 20 ° in azimuth. There are 18 sectors mounted on the East and West ends of the TPC. Each sector contains inner ($848 < r <$1321 mm) and outer ($1346 < r <$ 2466 mm) readout chambers. In order to improve the two track resolution the inner sector pads are made smaller. The inner readout chamber has 63 rows containing a total of 5504 pads and the outer chamber has 96 rows with 9984 pads. Based on the trigger selection the drifting charge is taken as the signal. The charge collected on the TPC pads is amplified and integrated by a low-input impedance amplifier circuit and digitized.The recorded x, y, z position is known as a hit. After applying further corrections to the inhomogeneities of the electric and magnetic fields, we proceed to the track reconstruction phase.

Track reconstruction is done in two stages. In the first stage, regions of ionization are localized within the same pad row and recorded as the center of gravity of the charge distribution. The final outcome of this stage is a set of space points, where the drift of electrons is initiated. In the next stage, a set of points due to a single particle trajectory has to be identified. Then the points are combined to form tracks. Since the charged particles move in a solenoidal magnetic field, tracks are fitted using a helical path. The curvature of the helix in the transverse plane (x,y) is used to calculate the momentum of the charged particles. Therefore the momentum resolution directly depends on the spatial resolution of the TPC.

$$\frac{dE}{dX} = -\frac{2\pi N_A z^2 e^4}{mc^2\beta^2}\frac{\rho Z}{A}\left\{ln\frac{2mc^2\beta^2 E_M}{I^2(1-\beta^2)} - 2\beta^2\right\} \tag{2.1}$$

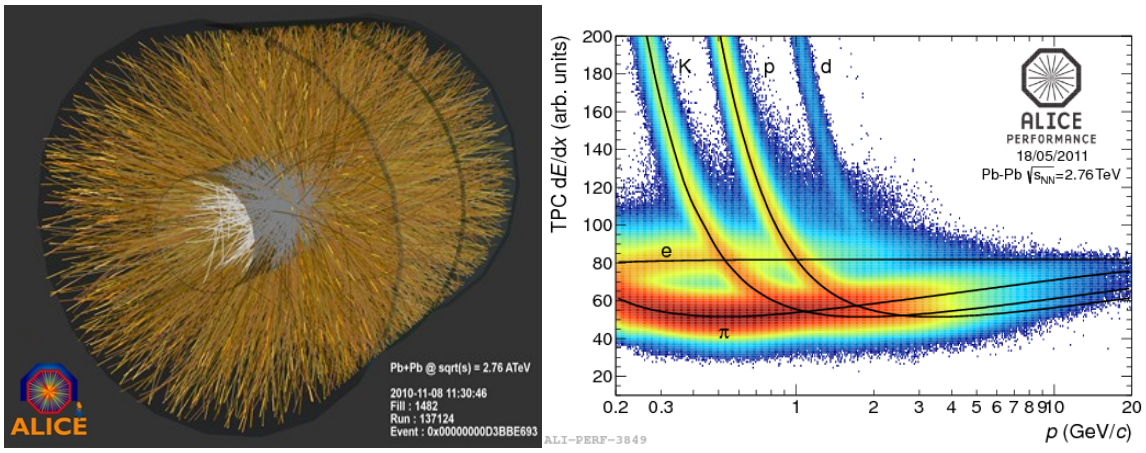

Figure 2.20: A reconstructed event display for a single Pb-Pb collision (left) and the energy loss distribution for primary and secondary particles in the TPC as a function of the momentum of the primary particle (right) [48].

The TPC can also be used for particle identification. As described by the Bethe-Bloch formula (Eq. 2.1.), a TPC can measure the specific energy loss of charged particles in a medium. The only particle properties entering the formula are its charge z and the velocity β of the particle traversing the TPC gas. The medium related drift gas properties are atomic number Z, mass number A, specic ionization I and density ρ. E_M is the maximum energy transfer in one interaction. The charge e and mass m of the electron, the speed of light c and the Avogadro number N_A enter into the Bethe-Bloch formula as described in [47]. As most of the particles seen by the TPC carry a single unit charge e, the ionization is simply a function of the velocity β of the particle. Figure 2.20 shows the specic energy loss for different particle species.

Due to the drift time in the TPC which is about 90 μs, the maximum luminosity which ALICE can handle is limited. For Pb+Pb The TPC was designed to cope

with a large number of particles per event in Pb-Pb collisions. In the most central collisions, it was designed to cope with reach about 20,000 primary and secondary particles. The TPC is capable of detecting the particles in the transverse momentum range $0.15 < p_{\mathrm{T}} < 100$ GeV/c. The transverse momentum resolution is around 6% for $p_{\mathrm{T}} < 20$ GeV/c in central Pb-Pb collisions, and around 4.5% for $p_{\mathrm{T}} < 20$ GeV/c in p-p collisions [29]. The TPC has a pseudo rapidity coverage of $|\eta| < 0.9$ if only the tracks with maximum radial track length are being considered.

2.3.2 The Inner Tracking System (ITS)

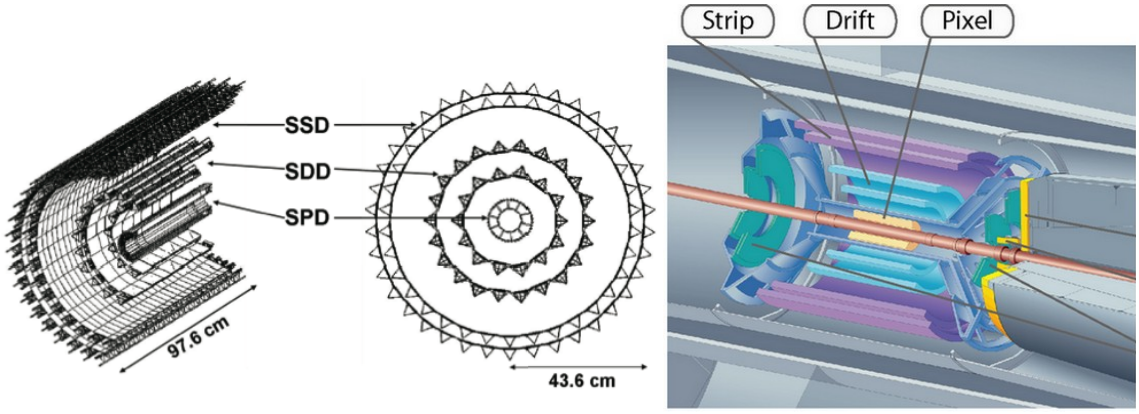

Figure 2.21: The schematics of inner tracking system in ALICE [183]

The Inner Tracking System (ITS) is the innermost set of tracking detectors and the main design goal of the ITS is to locate the collision vertex with maximum accuracy (better than 100 μm spatial resolution). The ITS consists of six layers of silicon detectors, arranged in three pairs of layers. As shown in Figure 2.21, each of these sub detector double layers is different from each other and designed to cope with the rapid change in particle density as a function of radius. In order to keep

the channel occupancy low, detectors are designed with very high granularity.

As shown in Fig. 2.21 the innermost two silicon layers are made of Silicon Pixel Detector (SPD) and the third and fourth layer consist of Silicon Drift Detectors (SDD), and the outermost two layers are Silicon Strip Detectors (SSD). The ITS is inserted inside the TPC. With a diameter of 6 cm, the beam pipe provides the lower physical boundary for the SPD. Transverse momentum is covered within the range $0.1 < p_{\mathrm{T}} < 3$ GeV/c with a resolution of (<2% for pions) [29]. In the high momentum region (for $p_{\mathrm{T}} > 3$ GeV/c), ITS still can be used to improve the transverse momentum resolution of the tracks which traverse the TPC. The ITS coverage in pseudo-rapidity is $|\eta| < 0.9$, over the full azimuth (2π).

Any charged particles traversing through the dead zones of the TPC and low p_{T} particles which do not read the TPC, can be reconstructed with the ITS alone. The ITS is also capable of particle identification via dE/dx using its (SDD) and (SSD) layers. In addition, the innermost SPD layer is being used as a centrality estimator and an online trigger.

2.3.3 VZERO detectores

The VZERO is a forward detector [29,33] which consists of two separate arrays of scintillator counters, V0A and V0C.The V0 counters are placed on opposite sides of the central barrel detectors along the beam line (see Figure 2.22). V0A and V0C are placed asymmetrically with respect to the interaction point: V0A is located 340 cm from the interaction point , while V0C is placed 90 cm from the interaction point on

the opposite side from V0A. Due to this asymmetry, V0A and V0C have different pseudo-rapidity coverages. V0A covers the pseudo-rapidity range $2.8 < \eta < 5.1$, while V0C covers $-3.7 < \eta < -1.7$. Each set of VZERO arrays contains 32 elementary counters arranged in 4 rings and 8 sectors of $\pi/4$ (see Figure 2.22).

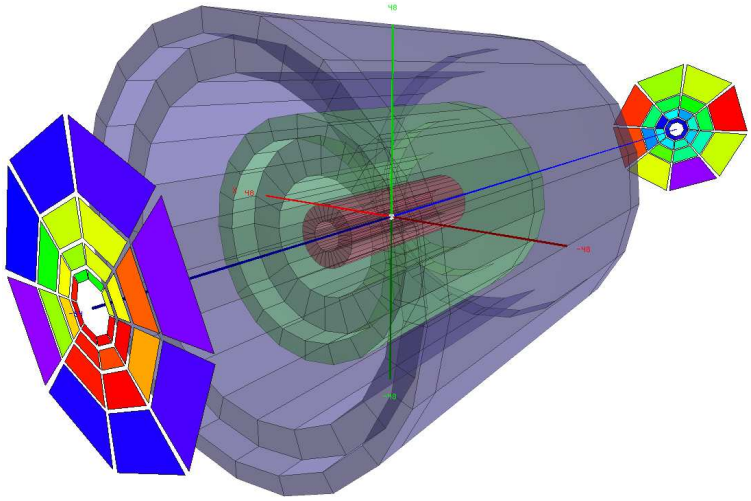

Figure 2.22: The VZERO detector layout with V0A and V0C [183].

The VZERO detector serves various purposes within the ALICE experiment. It provides several online triggers, namely: Minimum Bias trigger (MB), Multiplicity Trigger (MT), semi-Central Trigger (CT1) and Central Trigger (CT2). The VZERO detector is also utilized for centrality determination, with a resolution of about 0.5% of the centrality bin width in the most central collisions, and a resolution of better than 2% of the centrality bin width for peripheral collisions [84].

2.3.4 Summary of other sub detectors

Time-of-Flight Detector (TOF)

Particle identification using dE/dx gives (see Figure 2.20 right panel with TPC) relatively poor hadron separation in momentum range p_{T} =1- 2.5 GeV/c. Thus the task of TOF is to a better PID resolution in that range.

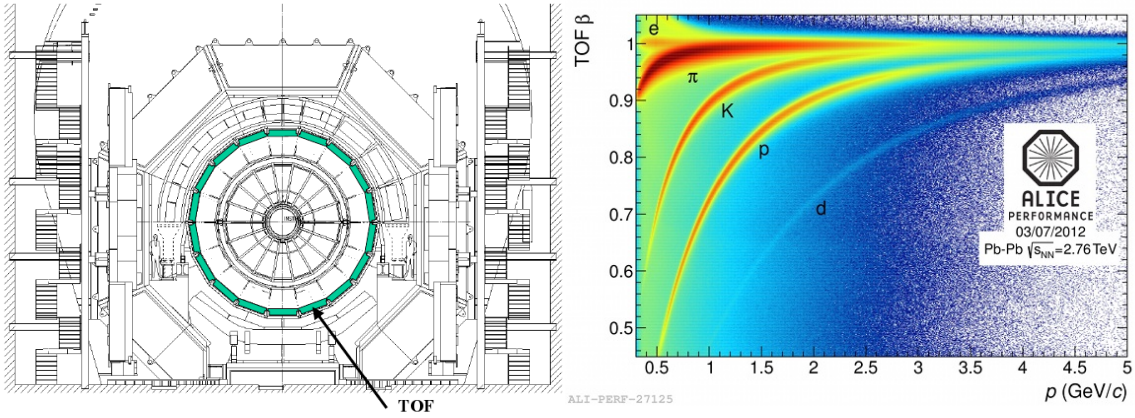

Figure 2.23: 18 sectors of the TOF system from the front view of the ALICE detector(left) and its PID capabilities(right panel) [183].

The TOF detector occupies the central interaction region of ALICE, covering $|\eta| < 0.9$ with full coverage in ϕ. The detector has an innermost radius of 370 cm and an outermost radius of 399 cm. It is divided into 18 azimuthal sectors and five modules of three different types are grouped in a line to form one sector. Each TOF module consists of a gas region which contains Multi-gap Resistive Plate Chambers (MRPC). These measure the time-of-flight of hadrons. The main aspect of the MRPC technology is to keep a high electric field uniform over the whole sensitive gaseous volume of the detector. Unlike in the TPC which uses atmospheric

pressurized gas, any ionization produced by a charged particle traversing the TOF detector will immediately start a gas avalanche which eventually generates a faster signal in the readouts. The basic unit is a MRPC pad of size 3.5 $\times$ 2.5 cm^2. The pads are organized in large modules and a full barrel has 18 (in rϕ) $\times$ 5 (along z) modules, covering an active area of $\approx 140m^2$. The MRPC resolution is measured to be in the 45$-$60 ps range, with an efficiency over 99%.

High-Momentum Particle Identification Detector (HMPID)

The High-Momentum Particle IDentification (HMPID) system pushes the PID capabilities of ALICE to a higher momentum range than possible by the energy loss measurements from ITS, TPC, and by the TOF. The HMPID detector is designed to extend the useful range for identification of ratios such as ϕ/K up to 3 GeV/c and K/p up to 5 GeV/c, on a track-by-track basis. A Ring Imaging Cherenkov detector (RICH) is used in the HMPID detector, which is placed at a distance of 4.5 m from the beam axis and consists of seven modules, each with an area of 1.5 $\times$ 1.5 m^2. It uses a liquid C_4F_{14} radiator and a multi-wire proportional counter (MWPC). The photo-cathode is a thin layer of CsI coated onto the pad plane. Figure 2.24 shows the schematics of the RICH operation.

The Cherenkov photons refract out of the liquid radiator and reach the CsI-coated pad cathode located at a distance (proximity gap) chosen to reduce the geometrical aberration of the Cherenkov angle measurement. This proximity gap is filled with

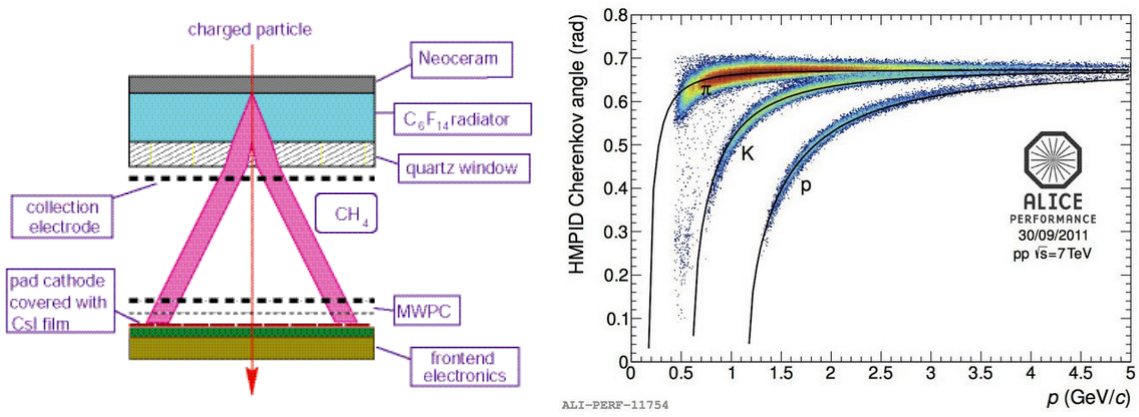

Figure 2.24: The working principle of RICH (left panel) and its PID capabilities (right) [183].

CH_4, and electrons released by ionizing particles in this gap, are prevented from entering the MWPC sensitive volume by a positive polarization of the collection electrode positioned close to the radiator.

Zero-Degree Calorimeter (ZDC)

The Zero-Degree Calorimeter measures forward energy, which is inferred to correspond to the number of neutrons from spectators. Thus, the measure provides another tool to estimate the centrality of collision. The number of participant nucleons is estimated as N_{part}= A- $N_{spectators}$, where A is the total number of nucleons in the nucleus (or the mass number). The ZDC is located 116 cm from the beam interaction point. This distance allows spectator protons and neutrons to be separated by the magnetic elements of the collider ring. The ZDC consists of three calorimeters. Two of them are hadronic, the ZN (which measures neutrons) and the ZP (which

measures protons) calorimeters. The third is an electromagnetic calorimeter ZEM (which measures the total energy).

Transition-Radiation Detector(TRD)

The Transition-Radiation Detector is located at a radius of 2.9 m, between the TPC and TOF detectors. It is the main detector for electron identification and consists of six layers of radiator foil stacks followed by Time Expansion Chambers filled with Xe/CO_2 gas. It uses the photons emitted via transition radiation to distinguish particles of different masses.

Forward Multiplicity Detector (FMD)

The FMD is a forward detector composed of 5 rings of semiconductor detectors. The design consideration was to detect the multiplicity of charged particles emitted at forward rapidities ($1.7< |\eta| <5.1$). The FMD is also used to study multiplicity fluctuations and elliptic flow.

The Electromagnetic Calorimeter (EMCal)

Calorimeters are devices that measure the energy of particles by stopping them and measuring the amount of energy released. Calorimeters provide the main way to identify neutral particles such as photons and neutrons, which are not visible in tracking devices. The EMCAL, is located outside of the TOF detector and covers

the pseudo rapidity of $|\eta| < 0.7$ region and azimuth of 107°. The EMCAL identifies particles using the electromagnetic showers they trigger in scintillators. Using the cell locations and energy deposited in each cell, shower shapes can be reconstructed and analyzed. It can also be used for jet energy reconstruction and jet events triggering.

2.3.5 ALICE trigger

The process of selecting particular collisions (events) is known as triggering and is useful for collecting rare or specific events without the need for recording vast quantities of unwanted data. The ALICE Central Trigger Processor (CTP) is designed to select events of different features at rates which can be scaled down to suit data recording requirements. The restrictions imposed by the bandwidth of the Data Acquisition (DAQ) system and the High-Level Trigger (HLT) has also to be taken into account when selecting trigger criteria. The challenge for the ALICE trigger is to make optimize the use of the detector components. Trigger selections are optimized for several different running modes: ion (Pb-Pb and several lighter species), pA, and pp, and the corresponding counting rates vary by almost two orders of magnitude. The first response from the trigger system has to be fast to suit the detector requirements. Three levels of hardware trigger are used in ALICE, called Level 0 (L0), Level 1 (L1) and Level 2 (L2). The first two triggers are fast triggers. The L0 trigger is sent to the relevant detectors to instruct them to start the readout, while the L1 trigger instruct them to either continue proceeding with the readout, or discard the event. The necessity for the existence of two triggers arises from the different speed of trigger input detectors and the necessity for some readout detectors (that

is, detectors on the receiving end of the trigger) to start processing the event early. The L0 trigger is sent 1.2μs after the event, while the L1 trigger is sent 6.5 μs later and is based on detectors that are too slow to participate in the L0 decision. The L2 trigger is of a different nature. It is sent after a much longer time has passed since the collision ($\approx 88\mu$s) and serves the role of past-future protection. It sends the signal that the event has been rejected or accepted based on the presence or absence of pile-up, (i.e., multiple collisions registered as a single event by the readout detectors).

2.3.6 ALICE Online systems

The ALICE experiment contains five online systems, Data Acquisition (DAQ), High-Level Trigger (HLT), Detector Control System (DCS), Experiment Control System (ECS) and the CTP. The purpose of the DAQ system is to collect the data readout from the detectors, process it and archive it. It is designed to provide the bandwidth required for the large data size of frequent Pb-Pb trigger (minbias, central or mid-central events), as well as collecting the highest possible event count for rare triggers. The data transfer between the detector readout systems and the DAQ is carried out by Detector Data Links (DDL). The front-end electronics (Local Data Concentrators, LDCs) assemble this data into sub-events and ship them to a farm of machines called Global Data Collectors (GDCs), which collect the sub-events into a whole event before eventually sending them to the storage network. The DAQ is also able to send BUSY signals to the CTP, as well as enable (or disable) some triggers to maximize detector availability of rare events.

2.3.7 ALICE analysis framework

The analysis presented in this thesis performed by software code in the ROOT[74] and AliROOT framework. ROOT is an object-oriented software toolkit which includes a set of statistical analysis libraries, a C interpreter and a GUI. ROOT is widely used in the field of high-energy physics. It is written in C++ with an interface to FORTRAN. ROOT stores analysis data structures in objects equipped with methods appropriate for the convenient treatment of these data structures and extraction of parameters. It includes mathematical libraries for integration, Fourier transform, minimization and fitting, and many other complex operations. ROOT is also equipped with a powerful graphing tool for the display of its data structures which has been used for many of the figures presented in this thesis. The ALICE experiment developed a specialized ROOT version called AliROOT. The core analysis functionalities are based on the processing of events stored in 3 types of data structures, called MC (for events created by Monte Carlo simulations), Event Summary Data (ESD) and Analysis Object Data (AOD). The ESD format is the result of the event reconstruction process (i.e. tracking, etc.) and contains all the data produced by that process. It includes a header containing general event and run information such as run number, magnetic field configuration, trigger information, reconstruction software version, various collision vertex and centrality estimations, multiplicity, etc. It also contains the complete arrays of tracks, V0 vertices and clusters found in all the detectors. The AOD format is obtained by filtering ESD events and selecting specific tracks, vertices and clusters. In this thesis work data files using the AOD format are used. CERN provides for the LHC users a distributed computing network

called the Grid. It is based on a collaboration of computing centers located in many places around the world (statistics can be found on the Grid status page found in [69]). Each computing center provides data storage, which, when taken globally, can host the 15 yearly petabytes of data produced by the LHC. These centers also provide computing power for analysis tasks. The UH computer cluster (TLC^2) is an ALICE grid point and actively participates in the grid computing. The ALICE Environment software (AliEn) provides an interface to the Grid for ALICE users, including various routines and shell environments to browse the data stored on the Grid and manage them. Individuals and groups in the ALICE collaboration write their own codes to analyze data and submit the analysis task jobs to the computing grid via AliEn. The job dispatcher in AliEn, divides the jobs into smaller sub jobs which can be executed within short periods of time.

Chapter 3

Physics of correlation functions

3.1 Physics of di-hadron correlations

In this chapter, physics conclusions that can be drawn from analyzing di-hadron correlations will be discussed. If the system created in a heavy-ion collision is homogeneous, static, and isotropic, then one could expect a uniform correlation structure in di-hadron correlations (see Figure 3.1). In this case, each particle produced will have an equal probability to be emitted in any direction. One can expect particular correlation structures due to known physical processes in high-energy nuclear physics. We model these processes into two categories; flow and non-flow. Then we use a fit model to extract parameters characterizing the flow and non-flow.

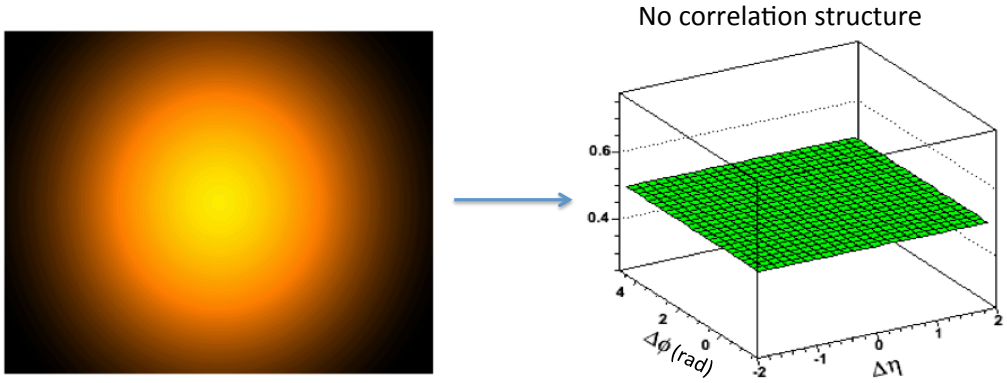

Figure 3.1: Left: A stationery isotropic homogeneous system. Right: Corresponding correlation structure in $\Delta\eta - \Delta\phi$.

3.1.1 Away-side momentum conservation

In chapter one, jet-like correlations were discussed. For a near side trigger parton, there exists a back to back recoil associated partner which is $180°$ opposite in azimuth. Since in p+p collisions we do not observe a medium formation, this associated parton on the away-side fragments similarly to the trigger parton. This requires another term to model the correlation structure on the away side as well (see Figure 3.5).

In relativistic heavy-ion collisions, the associated particles on the away-side undergo medium interactions (see Figure 3.2 middle). In azimuthal correlations, studies show that an enhanced yield with a broader away-side (compared to the near side width) peak occurs for low momentum particles. Regarding high p_T particles, a relatively strong depleted yield occurs [19]. As we discussed in section 1.4, this indicates that our recoil jet interacts with a medium, loses energy and changes its scatter direction in ϕ. One can characterize the away-side momentum conservation using a

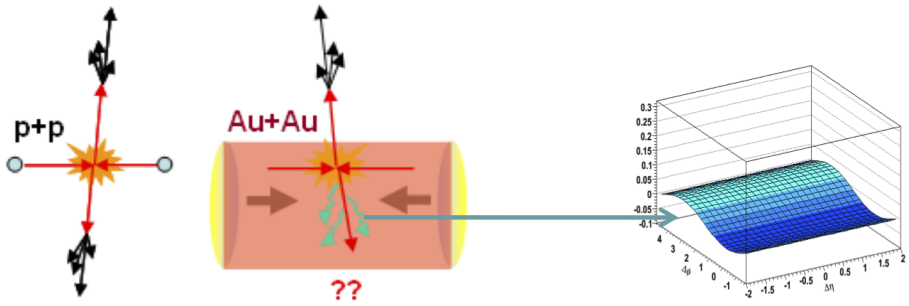

Figure 3.2: A schematic of hard-parton scattering in p + p(left) and heavy-ion (center) collisions. In p + p the associated partner does not traverse a medium whereas in heavy-ion system it does. The corresponding correlation structure is shown on right.

-cos($\Delta\phi$) component in the fit function as shown in Figure 3.2. This term models both global and local momentum conservation phenomena in such collisions. It is also important to note that, the first term in a Fourier expansion (which will be discussed next) of the angular distribution, known as dipolar asymmetry [62 - 68], takes the same mathematical form as the above mentioned away-side momentum conservation [163]. Here we have not made any attempts to separate the momentum conservation and dipolar asymmetry correlation phenomena from the extracted -cos($\Delta\phi$) model component.

3.2 Anisotropic Flow

3.2.1 Elliptic flow

In non-central heavy-ion collisions, the initial volume of the colliding system is anisotropic in coordinate space. It can be described by an almond shape. If the

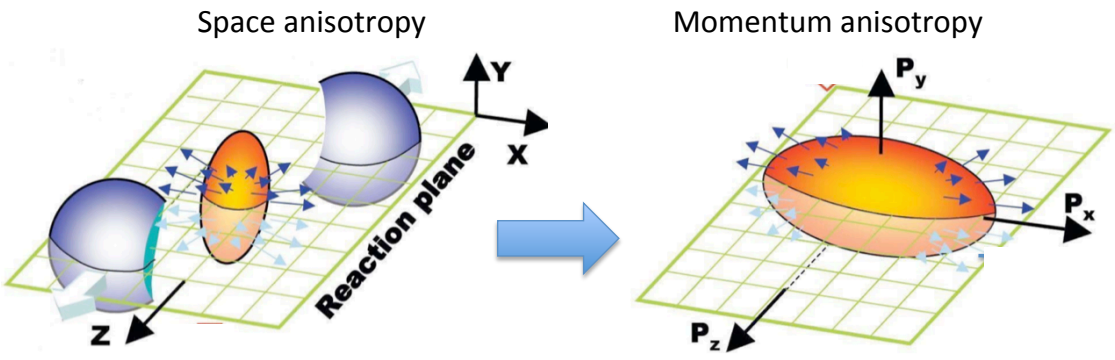

$$E\frac{d^3N}{d^3p} = \frac{1}{2\pi}\frac{d^2N}{p_T dp_T dy}(1+\sum_{n=1}^{\infty} 2v_n \cos(n(\phi-\Psi_{RP})),$$

$$v_n = \langle \cos(n(\varphi_i - \Psi_{RP})\rangle,$$

Figure 3.3: Left top: A mid-central heavy-ion collision in coordinate space has an almond shape. Right top: The initial coordinate space anisotropy is converted in to a momentum space anisotropy due to the collective nature of the medium. bottom: The momentum space anisotropy can be Fourier decomposed.

system behaves collectively, this initial coordinate space anisotropy is converted into a momentum space anisotropy for all measured final state charged hadrons. The strength of the resulting anisotropy in momentum space is a measure of the interaction strength. In a Fourier expansion of the angular distribution, the second harmonic component (v_2) directly relates to the elliptic shape of the initial system's coordinate space geometry, and was discussed as a key signature for the existence of a QGP [61]. In di-hadron (a pair correlation) measurements, this phenomena is expected to give a $\cos(2\Delta\phi)$ structure and we included the term in the fit model.

3.2.2 Higher-order harmonics

The importance of higher-order terms in the Fourier decomposition of an anisotropic angular distribution shown in Figure 3.3 has been discussed in recent theoretical publications [71,72,73]. Figure 3.4 shows a schematic diagram, which describes the underlying physical origin of higher-order harmonics.

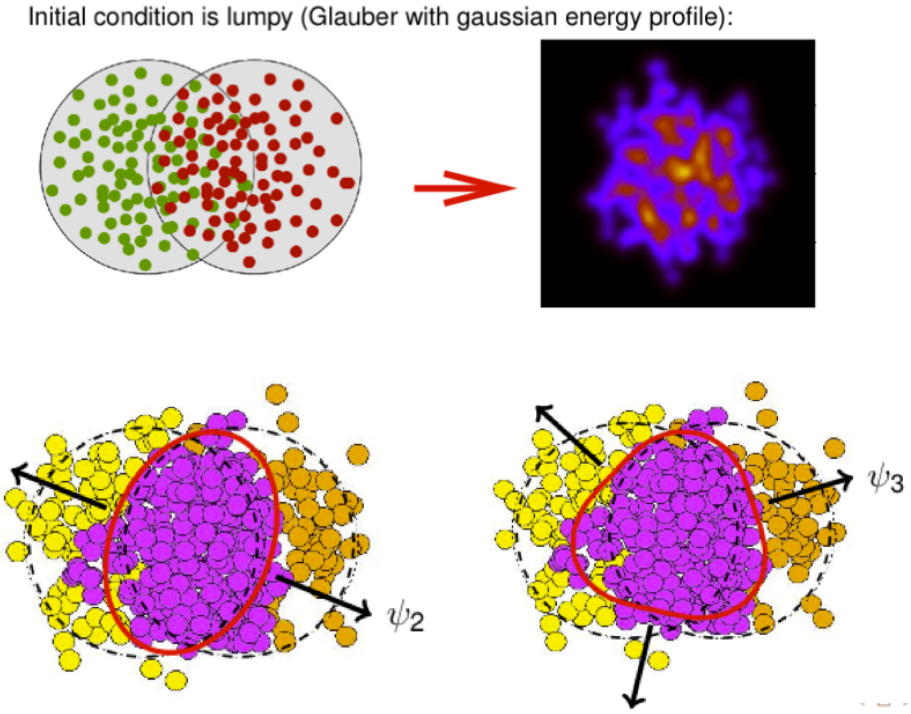

Figure 3.4: Top: Shows the initial nucleon and the corresponding energy distribution from a heavy-ion collision. Bottom: Shows possible initial nucleon distributions which generates higher harmonics flow (from M. Luzum QM 2011).

This follows the same reasoning as the elliptic flow, the 2nd harmonic in the azimuthal decomposition, but is more sensitive to the energy-density fluctuations in the colliding nuclei. In other words, rather than using hard sphere nuclei in a Glauber calculation, a realistic nucleon distribution is assumed. For instance, the Woods-Saxon

potential for the nuclear surface will lead to energy density fluctuations beyond the simple almond shape in the overlap region of the incoming nuclei. The bottom panel of Figure 3.4 shows an example of the third-order harmonic deduced from the same initial nucleon distribution than v_2. The series can be expanded to include all harmonics up to the order where they are believed to contribute to the correlation function. The higher-order fluctuations are predicted to become comparable to the 2nd Fourier coefficient. In our p_T evolution study, we will search for such evidence and incorporate model components ($\cos(n\Delta\phi)$; n $>$ 2) to extract the contributions to the correlation function.

3.3 Other contributions to the correlations

3.3.1 Parton fragmentation

Hard parton scatterings are expected to occur in elementary as well as heavy-ion collisions. In heavy-ion collisions, only the non-thermalized high momentum fraction of the fragmentation process should be visible above the bulk particle correlations from flow.

The left-hand side of Figure 3.5 illustrates a back to back hard scattering, and the resulting fragmentation of both partons in p + p collisions. The right-hand side of the Figure shows the corresponding di-hadron correlation on near and away side. In heavy-ion collisions, we do not observe the away side jet peak due to the medium modification (jet quenching). Therefore we include a 2d Gaussian model component

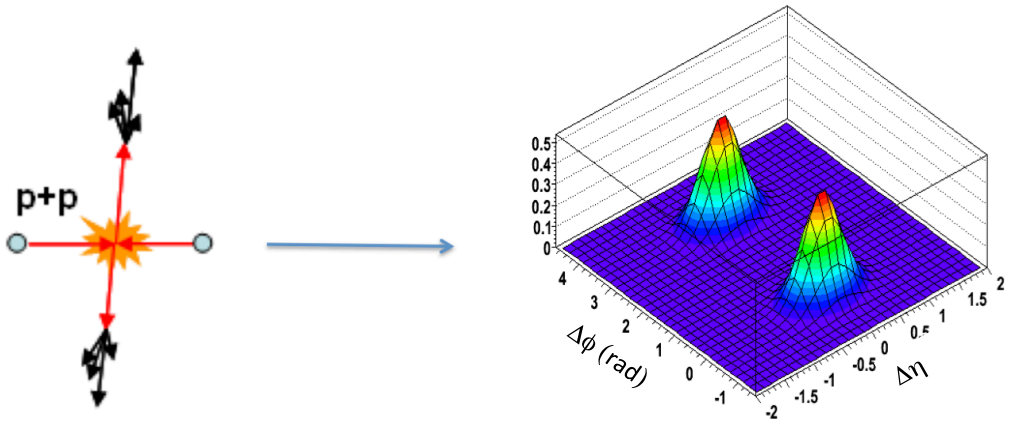

Figure 3.5: Left: Back-to-back parton hard scattering in p + p collisions. Right: The corresponding near and away side correlation structure in $\Delta\eta - \Delta\phi$ space.

in our fit model only in near side. It takes the following mathematical form:

$$a_3 exp\left\{-\frac{1}{2}\left[\left(\frac{\Delta\eta}{a_4}\right)^2 + \left(\frac{\Delta\phi}{a_5}\right)^2\right]\right\} \tag{3.1}$$

where a_3 is the amplitude, a_4 is the $\Delta\eta$ width and a_5 is the $\Delta\phi$ width. Although the jet peaks are measured to be symmetric in $\Delta\eta$ and $\Delta\phi$ in elementary collisions, we leave both widths as free parameters in order to accommodate any jet medium modification in heavy-ion collisions.

3.3.2 String fragmentation

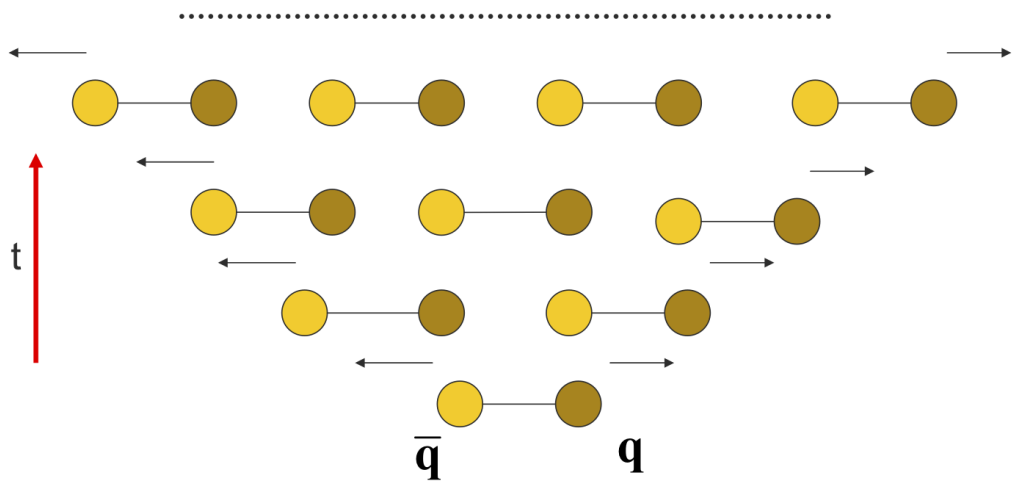

Figure 3.6: Time evolution of the Lund string fragmentation phenomena [69].

String fragmentation phenomena can be understood using the Lund model [162]. As we described regarding Figure 1.6, pulling apart a confined quark anti-quark pair (color neutral $q\bar{q}$ pair) generates a color force between the two quarks. The color force lines are constrained in a narrow tube connecting the two quarks with a string tension of ≈ 1 GeV/fm. In a collision, the low momentum partons create such $q\bar{q}$ pairs which undergo oscillations due to string tension and the resulting fragmentation occurs as shown in Figure 3.6. In the $q\bar{q}$ rest frame, these fragments are moving along the longitudinal direction with the possibility of arbitrary azimuthal orientation. This process is expected to generate a structure, which is uniform in $\Delta\phi$ and having a narrow width in $\Delta\eta$ as shown in Figure 3.7.

Therefore we include a 1d Gaussian model component in $\Delta\eta$ which has the following form:

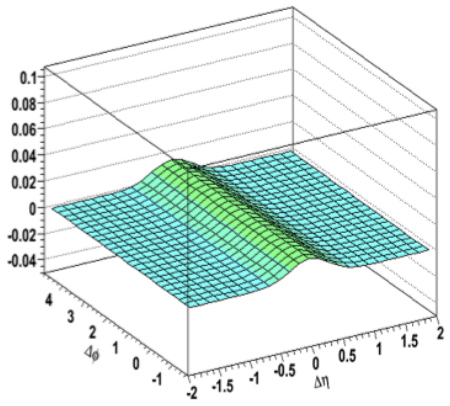

Figure 3.7: The 1d Gaussian structure in $\Delta\eta$ that represents Lund string fragmentation.

$$a_6 exp\left[-\frac{1}{2}\left(\frac{\Delta\eta}{a_7}\right)^2\right] \tag{3.2}$$

where a_6 and a_7 are the amplitude and width of the 1d Gaussian, respectively. It is also important to mention that the correlation contribution due to this phenomena becomes negligible in central (0-10%) heavy-ion collisions and at high p_T.

3.3.3 The Hanbury-Brown-Twiss (HBT) effect, $\gamma \rightarrow e^+e^-$ and resonances

In brief, quantum interference effects between particles with small differences in relative momentum (or similar momentum) give rise to small angle correlations. These effects result in a narrow peak around $\Delta\eta$, $\Delta\phi = 0$. Further studies of the HBT phenomena in heavy-ion physics can be found elsewhere [70]. A similar correlation structure can be expected from resonance decays. Resonances are excited states of

hadrons which decay via strong force. Since a strong decay is allowed (i.e., conserves all quantum numbers), the lifetime of hadronic resonances is comparable to the lifetime of the plasma (on the fm/c scale). The examples of such hadronic resonances and their decays are; $\Delta \to \rho\pi$, $k^* \to k\pi$, $\phi \to k^+k^-$ and $\rho \to \pi^+\pi^-$.

At the decay vertex, the daughter particles are close to each other in coordinate space. As a result, the di-hadron correlation structure contains small angle correlations produced via resonances. Finally, gamma conversions in the detector material ($\gamma \to e^+e^-$) also generate small angle correlations. A combination of these contributions are modeled using a 2d exponential model component centered around $\Delta\eta$, $\Delta\phi = 0$ which has the following form:

$$a_8 exp\left\{-1\left[\left(\frac{\Delta\eta}{a_9}\right)^2 + \left(\frac{\Delta\phi}{a_{10}}\right)^2\right]^{1/2}\right\} \tag{3.3}$$

where a_8 is the amplitude, $\Delta\eta$ and $\Delta\phi$ are widths of the 2d exponent respectively. It is also important to mention that all narrow peak contributions are low momentum phenomena.

Chapter 4

Methods and approach to analysis

Based on data from **SPS** experiments, in 2001 a press release from **CERN**[49] presented compelling evidence for the existence of a new state of matter. This evidence was awaiting confirmation at higher energies using **RHIC** data. It took several years for RHIC to obtain the existence of a new state of matter (**QGP**). We discussed these signatures of the **QGP** in chapter one. Today at the LHC we are on solid grounds regarding these signatures at an order of magnitude higher center of mass collision energy. In this chapter we discuss in detail one particular set of measurements, namely fluctuations and correlations [50] used to study the Quark Gluon Plasma.

4.1 Fluctuations and correlations

The study of fluctuations and correlations is a primary concern when characterizing a physical system, providing essential information about the effective degrees of freedom of the system. Furthermore, the susceptibilities, which characterize the correlations and fluctuations, predict the response of the system to applied perturbations. In general one can classify three types of fluctuations.The most fundamental level of fluctuation is the quantum fluctuations, which plays a lesser role in the context of heavy-ion collisions. The second category is dynamical fluctuations which relate to the dynamics of the system. For instance, density fluctuations are dynamical fluctuations governed by the compressibility of the system. The final category, called "statistical" fluctuations are due to a number of reasons such as limited statistics, acceptance, efficiency etc. In order to analyze the dynamical fluctuations, one needs to have a control over the statistical fluctuations. In an analysis, these fluctuations can be subtracted to isolate the dynamical fluctuations. In the context of heavy-ion collisions, a given observable can be measured on an event by event basis and the fluctuations can be studied over an ensemble of events. The most relevant measurements in heavy-ion collisions are based on transverse momentum, multiplicity, particle ratio and the net-electric charge fluctuations.

The study of transverse momentum fluctuations is a standard event by event measurement. In a single event one can define the average transverse momentum as:

$$\langle p_T \rangle = \frac{1}{N} \sum_{i=1}^{N} p_{t,i} \tag{4.1}$$

where N is the total number of tracks in an event (also called multiplicity) and index i is used to index a particle or a track. The multiplicity of an event is impact parameter dependent and shows random statistical fluctuations event-wise. In addition, the measured quantity is dependent on the detector acceptance. In general terms, the fluctuation measure has a scale dependence. In order to suppress the statistical fluctuations, a fluctuation measure was developed [51] to express the variance.

The improved fluctuation measure is defined as follows:

$$\Delta\sigma^2_{p_t:n} \equiv \frac{1}{\epsilon} \sum_{j=1}^{\epsilon} n_j [\langle p_t \rangle_j - \hat{p_t}]^2 - \sigma^2_{\hat{p_t}} \tag{4.2}$$

$$\equiv 2\sigma_{\hat{p_t}} \Delta\sigma_{p_t:n} \tag{4.3}$$

Considering all charged-particles from all the events, mean and variance of the p_t distribution are defined as $\hat{p_t}$ and $\sigma^2_{\hat{p_t}}$, where, j is the event index and $\langle p_t \rangle_j$, n_j are the mean p_t and multiplicity of the j^{th} event, respectively. The number of events per centrality bin is denoted as ϵ. More detailed studies of this fluctuation measure were performed in the STAR experiment at RHIC [51]. Here we adopt the same techniques for the ALICE experiment.

In order to study the dependence of the scale, the improved fluctuation quantity is measured as a function of $\delta\eta$ and $\delta\phi$, as shown in the left panel in Figure 4.1. The

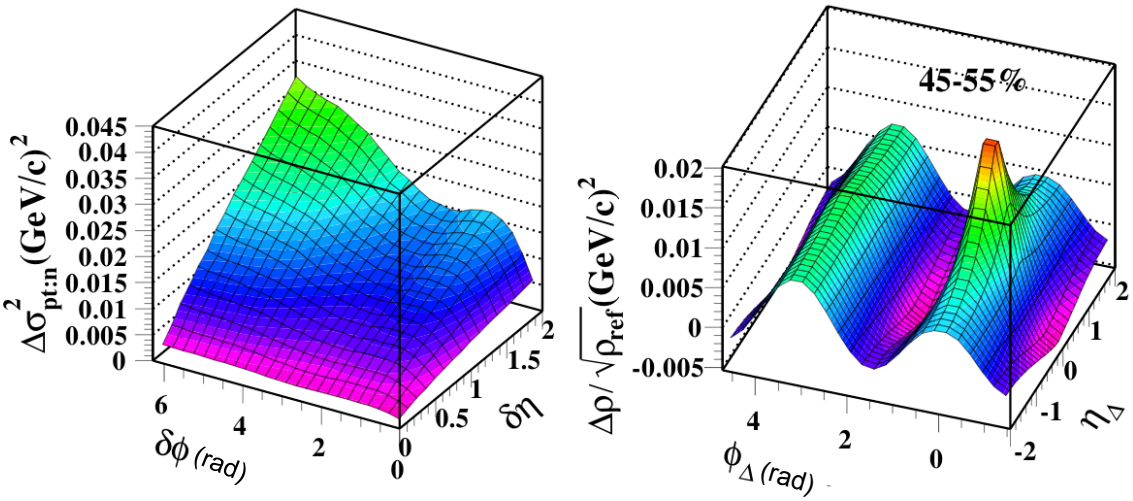

Figure 4.1: Left panel: $\delta\eta - \delta\phi$ scale dependence of $\Delta\sigma^2_{p_t:n}$. Right panel: The corresponding p_t correlation from inversion.

structure contains significant information. Therefore an interpretation of the results is not straightforward. It is easier to understand as integral of the covariance. In this procedure, a correlation measure is constructed by computing the covariance and a proper normalization. Here we form the well known Pearson's correlation coefficient [53]. This way the study of fluctuations becomes a study of correlations. The inverted fluctuation measure [52] is shown by Figure 4.1 in the right panel. Then we concentrate on studying the angular distribution of correlated particles in $\Delta\eta$ and $\Delta\phi$. A comprehensive mapping from fluctuations to correlations has been carried out in [54]. The governing mathematical relationship between fluctuations and correlations can be expressed as:

$$\Delta\sigma^2_{p_t:n}(\delta\eta,\delta\phi) = 4\epsilon_\eta\epsilon_\phi \sum_{i,j} K \frac{\Delta\rho(p_t:n)}{\sqrt{\rho_{ref}(n)}}(i\epsilon_\eta, j\epsilon_\phi) \tag{4.4}$$

On the right hand side we have the per-particle correlation density expressed by Pearson's correlation coefficient $\frac{\Delta\rho}{\sqrt{\rho_{ref}}}$. Here K is a kernel which contains two dimensional histogram binning information, ϵ_x is a bin width with indices i and j corresponding to a correlation bin. The right panel on Figure 4.1 shows the correlation structure with correlated angular distributions providing more visualization. As we discussed in chapter 3, one can distinguish. The apparent flow signal in Figure 4.1 right panel is a good example of a non-statistical or dynamical fluctuation.

4.2 Formalism

In this section, we discuss the formalism of sampling random variables to construct the Pearson's correlation coefficients.

4.2.1 Pearson's correlation coefficient

The mean or the average of a given x_i (i = *1,2,3, ... N*) set of data is defined as:

$$\bar{x} = \frac{1}{N}\sum_{i=1}^{N} x_i \tag{4.5}$$

and the variance is defined as:

$$\sigma_x^2 = \frac{1}{N}\sum_{i=1}^{N}(x_i - \bar{x})^2 \tag{4.6}$$

In statistics, covariance is used to determine the relationship between two random variables. For two sets of data x_i and y_i the covariance is defined as:

$$Cov(x,y) = \frac{1}{N}\sum_{i=1}^{N}(x_i - \bar{x})(y_i - \bar{y}) \tag{4.7}$$

When y=x, the above definition reduces to the variance of a random variable. When we normalize the covariance by the standard deviation of each distribution we construct the Pearson's correlation coefficient.

$$R_{xy} = \frac{Cov(x,y)}{\sigma_x \sigma_y} \tag{4.8}$$

$$= \frac{\sum_{i=1}^{N}(x_i - \bar{x})(y_i - \bar{y})}{\sqrt{\sum_{i=1}^{N}(x_i - \bar{x})^2 \sum_{i=1}^{N}(y_i - \bar{y})^2}} \tag{4.9}$$

The range of above measure R can oscillate between -1 and +1, which can be shown via direct substitution of $y_i = \pm x_i$ in the equation. For perfectly correlated random variables, R reaches +1 and in the case of perfectly anti-correlated data R reaches -1. If the random variables are uncorrelated R takes the value 0. This can be further understood by looking at Figure 4.2

Autocorrelations in heavy-ion physics

In the statistical description of Brownian motion, Einstein introduced the concept of autocorrelations in 1905 [55, 56]. Later scientists including Wiener, and Langevin, also contributed to the development of the concept and its applications. Today this concept has become a standard analysis tool which is commonly used in diverse fields, such as signal processing,statistical applications, regression analysis, etc.

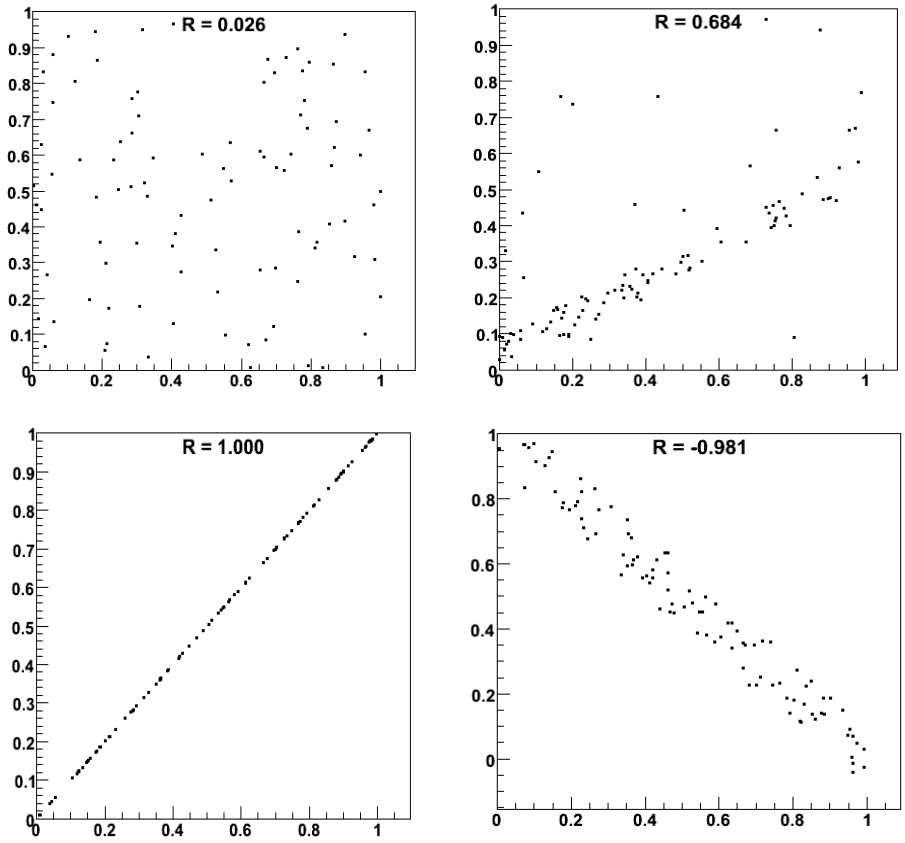

Figure 4.2: Degree of correlations using few data points.

The key concept of autocorrelation is to invoke correlations within the same distribution rather than two different variables. In other words, one determines the cross-correlation of a signal with itself. Going back to equation 4.9, by studying the amplitude at the time step i denoted as x_i, and the correlation between the measured quantities at time step i+1 (of the same quantity), the autocorrelations (or correlations for the same variable) are studied. Setting $y_i = x_i + 1$ in equation 4.9, R_{xy} determines the independence of a single point and the averaged next point in a two dimensional histogram bin. Considering an arbitrary time difference k, the equation 4.9 becomes,

$$R_k = \frac{\sum_{i=1}^{N-k}(x_i - \bar{x})(x_{i+k} - \bar{x})}{\sum_{i=1}^{N-k}(x_i - \bar{x})^2} \tag{4.10}$$

Since we detect particles from a heavy-ion collision with a finite resolution as a subset of a parent distribution containing all the particles from all the events, the autocorrelation method is applicable for heavy-ion physics. Considering an arbitrary quantity x a two dimensional histogram is binned with n detected particles. Defining $\mathbf{n_i(a)}$ as the number of particle counted in bin $\mathbf{a}$ for i^{th} event, the correlation between two histogram bins $\mathbf{a}$ and $\mathbf{b}$ averaged over all N events can be expressed as follows:

$$R_{ab} = \frac{1}{N}\sum_{i=1}^{N}\left\{n_i(a) - \overline{n(a)}\right\}\left\{n_i(b) - \overline{n(b)}\right\}/\sigma_a\sigma_b \tag{4.11}$$

$$= \overline{(n-\bar{n})_a(n-\bar{n})_b}/\sigma_a\sigma_b \tag{4.12}$$

The over-bar in the equation 4.12 represents the event averaging with bin indices as subscripts. An autocorrelation among these histogram bins can be defined by measuring the relative displacement. In order to test the correlation between $\mathbf{n(}\boldsymbol{x}\mathbf{)}$ in bin $\mathbf{a}$ and $\mathbf{n(}\boldsymbol{x} + \Delta x\mathbf{)}$ in bin $\mathbf{a} + \mathbf{k}$ as a function of Δx, we embedded a test particle and average over x. This measurement determines the particle distribution around the test particle on average. Thus, the time series autocorrelation of equation 4.11 can be re-written as follows:

$$R_k = \frac{1}{x_{max} - k}\sum_{a=1}^{x_{max}-k}\overline{(n-\bar{n})_a(n-\bar{n})_{a+k}}/\sigma_a\sigma_{a+k} \tag{4.13}$$

In di-hadron correlation analysis, particle pairs are selected and the correlation is evaluated per pair. If we use pre-binned distributions, some practical concerns should be taken into account. In histograms we have a lower limit for bin width depending on the available statistics. Then we have to approximate the position as the bin center causing a shift of the actual position. In other words we lose information in the process of binning. Furthermore, if two tracks are too close, we have to deal with additional inefficiencies.

Therefore the use of direct binning is preferred over the use of pre-binned particle distributions. In the next step the measure of covariance is expressed in terms of particle pairs. Considering the numerator in equation 4.12, the covariance can be re-written as:

$$\overline{(n-\bar{n})_a(n-\bar{n})_b} = \overline{n_a n_b} - \overline{n_a}.\overline{n_b} \tag{4.14}$$

The first term on the right-hand side of equation 4.14 represents the total number of pairs in bin (**a**, **b**), averaged for a two-dimensional histogram of particle pairs (e.g. η_1, η_2) event by event. The second term calculates the expectation of **a** and **b** for the uncorrelated case. Particles in a particular event are combined to form all possible correlations by constructing pairs in a two-dimensional histogram. The first term on the right hand side of equation 4.15. is referred to as sibling pairs. The second term is measured by taking the two particles from uncorrelated events and which we call mixed pairs. A detailed discussion of the histogram binning using single particle and particle pairs can be found in [57]. By defining $n_{i,a}$ as the number of particles in bin

a for event i with ϵ total events, one can simply derive the equivalence between the single particle bins and particle pairs in terms of sibling and mixed events:

$$
\begin{aligned}
Cov(a,b) &= \overline{n_a n_b} - \overline{n_a}.\overline{n_b} \\
&= \overline{n_a n_b} - \frac{1}{\epsilon^2}\sum_{i=1}^{\epsilon}\sum_{j=1}^{\epsilon} n_{i,a} n_{j,b} \\
&= \overline{n_a n_b} - \frac{\epsilon(\epsilon-1)}{\epsilon^2}\frac{1}{\epsilon(\epsilon-1)}\sum_{i=1}^{\epsilon}\sum_{j=1,j\neq i}^{\epsilon} n_{i,a} n_{j,b} - \frac{1}{\epsilon^2}\sum_{i=1}^{\epsilon} n_{i,a} n_{i,b} \\
&= \left(1-\frac{1}{\epsilon}\right)\overline{n_a n_b} - \frac{\epsilon-1}{\epsilon}\frac{1}{\epsilon(\epsilon-1)}\sum_{i=1}^{\epsilon}\sum_{j=1,j\neq i}^{\epsilon} n_{i,a} n_{j,b} \\
&= \frac{\epsilon-1}{\epsilon}\left[\overline{n_a n_b} - \frac{1}{\epsilon(\epsilon-1)}\sum_{i=1}^{\epsilon}\sum_{j=1,j\neq i}^{\epsilon-1} n_{i,a} n_{j,b}\right] \\
&= \frac{\epsilon-1}{\epsilon}[\overline{n_a n_b} - \overline{n_a}.\overline{n_{b mixed}}]
\end{aligned}
\tag{4.15}
$$

The factor in front of the square brackets approaches unity for a large number of events. In order to determine the denominator in equation 4.12, we need to express it in terms of particle pairs. In our approach, the number of particles we are detecting in a given detector volume during a very short period of time is discrete. Therefore this rather challenging task can be achieved by approximating the particle detection to a Poisson process. In a Poisson distribution the mean and variance take the same value. We can then re-write the denominator of equation 4.12 as $\sigma_a\sigma_b \approx \sqrt{\overline{n_a}.\overline{n_b}}$. The particle pair quantity (**a**, **b**) from mixed pairs is given by the term inside the square root.

4.2.2 Correlation measure

Equation 4.12 is now expressed in terms of sibling and mixed pair densities as shown follows:

$$\frac{\Delta\rho}{\sqrt{\rho_{ref}}} = \frac{\overline{(n-\bar{n})_a(n-\bar{n})_b}}{\sqrt{\overline{n_a}.\overline{n_b}}} \tag{4.16}$$

Here $\Delta\rho \equiv \rho_{sib} - \rho_{ref}$ where ρ_{sib} ,ρ_{ref} denote the sibling pair-density and mixed pair-density, respectively. Since ρ_{sib} contains both correlated and uncorrelated pairs, one should subtract ρ_{ref} from ρ_{sib}. Then the correlated pair density is given by $\Delta\rho$. ρ_{ref} is the number of uncorrelated pairs, which is proportional to the number of particles. Thus our correlation measure is proportional to the correlated pairs per particle.

When using experimental data we have take into account experimental artifacts, such as tracking efficiency, detector acceptance etc. Those factors influence both sibling and mixed pair distributions. In the case of sibling pairs one needs to consider two track inefficiencies. In order to correct for common experimental artifacts for both sibling and mixed pair distributions, we construct the ratio $r = \frac{\rho_{sib}}{\rho_{ref}}$. We can re-arrange the correlation measure as:

$$\frac{\Delta\rho}{\sqrt{\rho_{ref}}} = \sqrt{\rho_{ref}}\frac{\Delta\rho}{\rho_{ref}} \tag{4.17}$$

$$= \sqrt{\rho_{ref}}(r-1) \tag{4.18}$$

Still, some of these artifacts remain due to the multiplication of $\sqrt{\rho_{ref}}$ (i.e., the pre-factor). An idealized $\rho^{'}_{ref}$ can be constructed. This idealized $\rho^{'}_{ref}$ can be formed using $\frac{dn}{d\eta}$ at $\eta = 0$ to get rid of the remaining art effects [58]. The corrections due to two track efficiencies will be discussed briefly under section 4.4.2.

We need to make sure that we treat the sibling and mixed-event distributions in the same way. This is taken care of by analyzing events in appropriate windows of the event centrality Δn and primary z vertex location Δz. In section 4.2.4 we will discuss these techniques in detail. These calculations allow us to determine the final correlation measure as:

$$\frac{\Delta\rho}{\sqrt{\rho_{ref}}}(a,b) = \sqrt{\rho^{'}_{ref}}[r(a,b) - 1] \tag{4.19}$$

4.2.3 Triggered and untriggered di-hadron correlations

Measurements of untriggered di-hadron correlations explore the bulk correlation structures in heavy-ion collisions. All charged hadrons with $p_{\mathrm{T}} > 0.15\mathrm{GeV/c}$ are used to form a correlation function, which for this analysis is defined as follows:

$$\frac{\Delta\rho}{\sqrt{\rho_{ref}}}(\Delta\eta,\Delta\varphi) = \left[\frac{d^2N_{ch}}{\Delta\eta\Delta\varphi}\left(\frac{\rho_{sib}}{\rho_{ref}} - 1\right)\right] \tag{4.20}$$

The denominator is the square root of the number of background pairs($\sqrt{\rho^{'}_{ref}}$), which represents the number of charged hadrons, i.e $d^2N_{\mathrm{ch}}/d\eta d\phi$. The correlation

function therefore measures the number of correlated pairs per particle. In this analysis we also use the definition $C(\Delta\eta, \Delta\varphi)$ and its relation to equation 4.21 is:

$$C(\Delta\eta, \Delta\varphi) = \left[\frac{\Delta\rho}{\sqrt{\rho_{ref}}}(\Delta\eta, \Delta\varphi) + 1\right] \tag{4.21}$$

4.2.4 Sibling and mixed event distributions

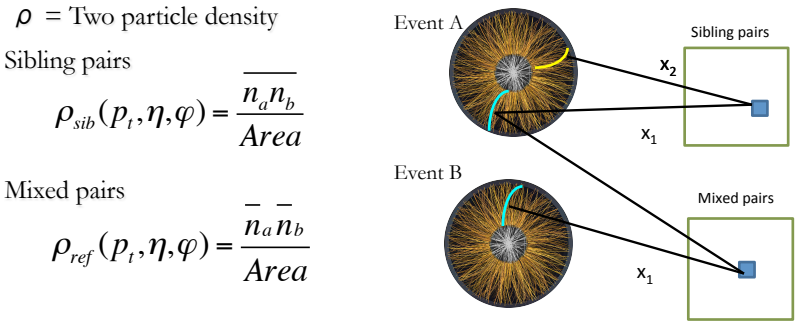

Figure 4.3: track selection of same and mixed events

Figure 4.3 shows a schematic of sibling and mixed event distributions. First, we determine the background by using tracks in $\Delta\eta$ and $\Delta\phi$ with pairs from different events to generate uncorrelated pairs. One needs to carefully perform the mixed event distribution by mixing events with similar event population, such as particle multiplicity. Therefore, we select the events based on the primary vertex location and the centrality percentile. Events within $|\Delta PVz| = 0.4cm$ and 1% of the centrality are used for the background determination. Furthermore, the mixed-event distribution can be improved with multiple event mixing. In terms of computing, multiple event mixing is time consuming, though we found that mixing one event with five

other events optimizes the background determination. In addition, the pair distributions are constructed in a charge dependent manner: NN (negative,negative), NP, PN and PP(positive, positive). This procedure gives us the possibility for further charge-dependent studies. In order to obtain a $0-10\%$ centrality bin, we combine the first ten 1%-wide centrality bins. Figure 4.4 shows the same and mixed events

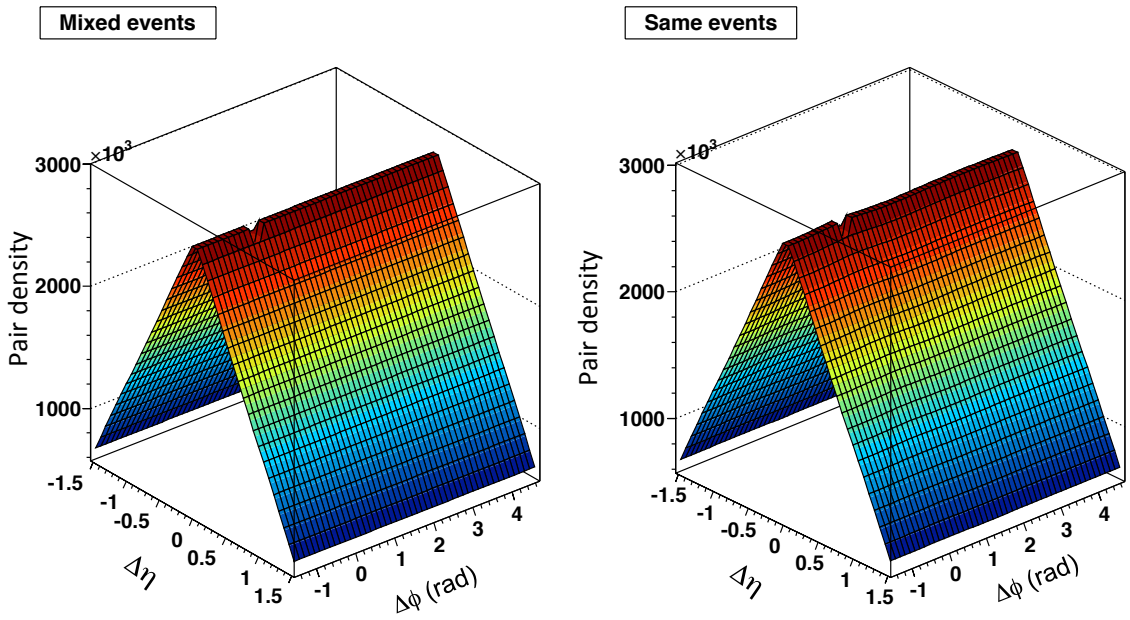

Figure 4.4: Same and mixed event distributions

as a function of $\Delta\eta$ and $\Delta\phi$ for the $0-10\%$ event class .

4.2.5 Correlation function

Figure 4.5 shows the extracted correlation function for all charged-particles with $p_{\mathrm{T}} > 0.15\mathrm{GeV/c}$. The most prominent structure is a short range nearside spike,

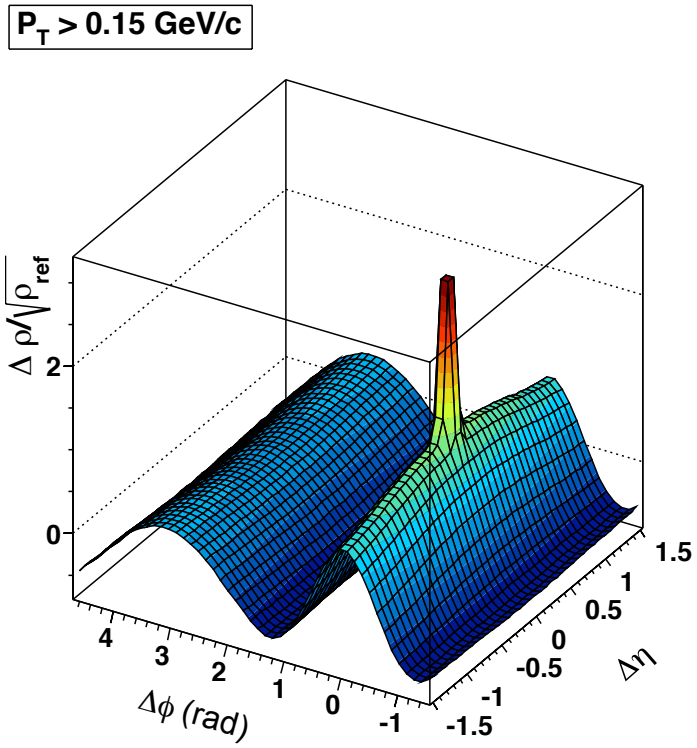

Figure 4.5: The measure $\frac{\Delta\rho}{\sqrt{\rho_{ref}}}$ in minimum bias events for charged-particles with p_{T}> 0.15 GeV/c

which can be attributed to **H**anbury-**B**rown-**T**wiss (HBT) effect, $\gamma \rightarrow e^{+}e^{-}$ and resonance decay. The prominent elliptic flow is represented by the $cos(2\Delta\phi)$ structure, which is independent of $\Delta\eta$.

4.3 System, Events and track selection

In this section we mainly discuss the specific event selection and track selection cuts used in the analysis. The set of data is LHC10h, which classifies the heavy-ion run

in 2010. We list here the set of specific run numbers in the data set.

139510, 139507, 139505, 139503, 139465, 139438, 139437, 139360, 139329, 139328, 139314, 139310, 139309, 139173, 139107, 139105, 139038, 139037, 139036, 139029, 139028, 138872, 138871, 138870, 138837, 138732, 138730, 138666, 138662, 138653, 138652, 138638, 138624, 138621, 138583, 138582, 138579, 138578, 138534, 138469, 138442, 138439, 138438, 138396, 138364, 138275, 138225, 138201, 138197, 138192, 138190, 137848, 137844, 137752, 137751, 137724, 137722, 137718, 137704, 137693, 137692, 137691, 137686, 137685, 137639, 137638, 137608, 137595, 137549, 137544, 137541, 137539, 137443, 137441, 137440, 137439, 137434, 137432, 137431, 137430, 137366, 137243, 137236, 137235, 137232, 137231, 137230, 137162, 137161, 137135.

Reconstruction pass2, for Analysis Object Data (AOD086) is used (14M events). For Monte Carlo corrections and cross checks, the AMPT production LHC12a11a AOD081 is used. Regarding software versions, the data and MC productions have been analyzed using AliRoot, ALICE's native software.

4.3.1 Event selection based on primary vertex

The results presented here are based on three data sets taken by the ALICE detector at LHC. Data from Pb+Pb $\sqrt{s_{NN}}$ = 2.76 TeV collisions (minimum bias triggered events) has been analyzed. In addition, a cut on z vertex position is imposed. We reject events with a z vertex position greater than ± 7 cm from the TPC center. For studies of systematic uncertainties, a looser cut (10cm) and a tighter cut (5cm) were

applied. Further details will be discussed in Chapter 6 in the systematics uncertainty estimation section.

4.3.2 Event centrality

Event centrality is a classification based on the impact parameter of a heavy-ion collision. The impact parameter b is defined as the relative distance in radial direction of the centers of the colliding nuclei. Collisions with a smaller impact parameter produce a higher number of tracks and those events are called "central collisions". A higher b leads to events called "mid-central" or "peripheral" collisions. In the analysis presented in this dissertation, the centrality determination will be based on the multiplicity obtained in the VZERO detector. Measurements performed using other detectors will be also analyzed for systematic uncertainty estimations. Figure 4.6 shows the VZERO multiplicity distribution and the resulting centrality definition using the Glauber model.

4.3.3 Track selection cuts

In general, we can classify track selection cuts into three categories: reconstruction cuts, kinematic cuts and particle identification cuts. Table 4.1 summarizes the applied track cuts accordingly.

The lower p_T cut value 0.15 GeV/c is set considering the applied magnetic field strength in the TPC. Lower-momentum charged-particles can't reach the inner field cage of the TPC since their radius of curvature in the field is too small. In an event, all

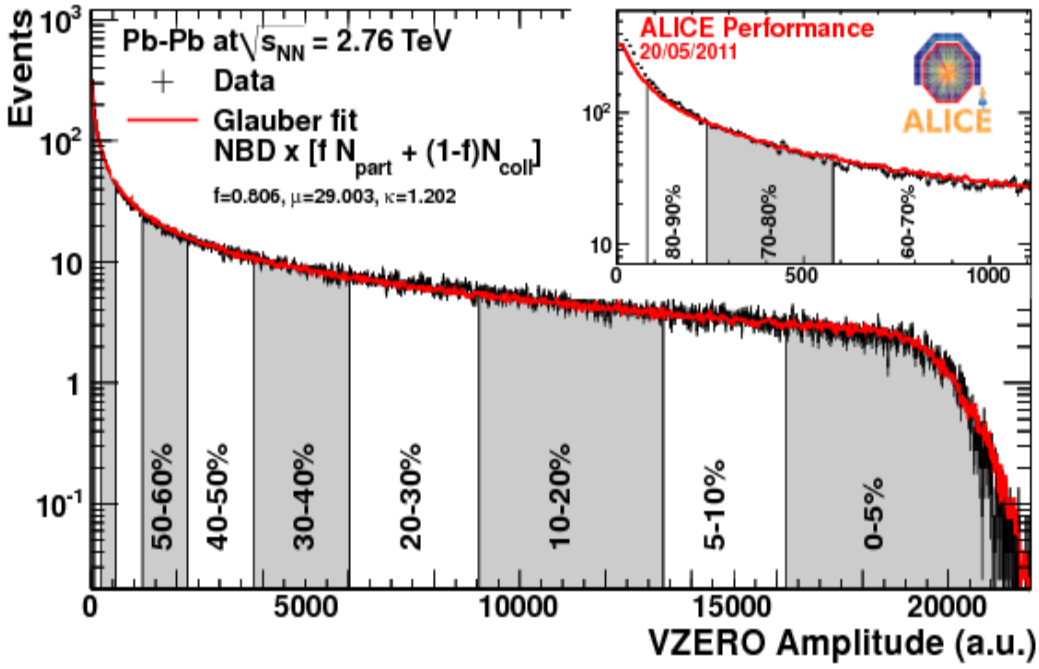

Figure 4.6: V ZERO estimated Multiplicity distribution and the fit based on Glauber model.

primary charged-particle tracks emerge from a single collision vertex. We refer to this as the primary vertex. In contrast, there are secondary charged-particle tracks which do not point towards the primary vertex. These tracks are produced by decaying parent particles or by interaction of primary particles with detector materials. In order to select primary particles from the primary vertex we apply a **D**istance-of-**C**losest **A**pproach (**DCA**) cut. The DCA cut rejects the particles (secondaries) which do not point towards the primary event vertex. In this analysis, tracks with a DCA_z above 3.2cm and DCA_{xy} above 2.4cm are removed. Track reconstruction is done using the Kalman filtering procedure [42]. By setting a minimum number of cluster points and maximum $\chi^2/cluster$ required for in reconstruction, the purity of

Table 4.1: Summary of track cuts applied in the analysis

Category	Track cut	Range	Description
Reconstruction	$cluster >$	70	Number of fit points per track
	$\chi^2/cluster <$	4.0	Reconstructed track quality
	$DCA_z <$	3.2 cm	Minimum distance from a reconstructed vertex to the track
	$DCA_{xy} <$	2.4 cm	Minimum distance from a reconstructed vertex to the track
Kinematic	p_{t}(GeV/c)	0.15	p_{t} range used in the minimum bias analysis
	ϕ	$\pm\pi$	Full azimuthal acceptance
	$\lvert\eta\rvert$	0.80	Optimal η acceptance in TPC for our analysis
PID	Charge (e)	±1	Includes tracks with only a charge of ±1
	NSigmaElectron	±1.5	Rejects background electrons

the reconstructed track is enhanced. In our analysis, we use the angular variables η and ϕ. Though we have a lager acceptance in η, we restrict our acceptance in $|\eta| < 0.8$ due to reduced reconstruction efficiencies in larger η. We use the full azimuth acceptance of the ALICE detector.

We only accept charged-particle tracks with the magnitude of electronic charge of $\pm e$ when constructing the correlation function. Even though the contribution from hadrons with higher electric charge is negligible, we reject those hadrons. We have

to minimize the electron contamination by using a restriction on the TPC energy loss, which is given by the Bethe-Bloch formula in equation 2.1.

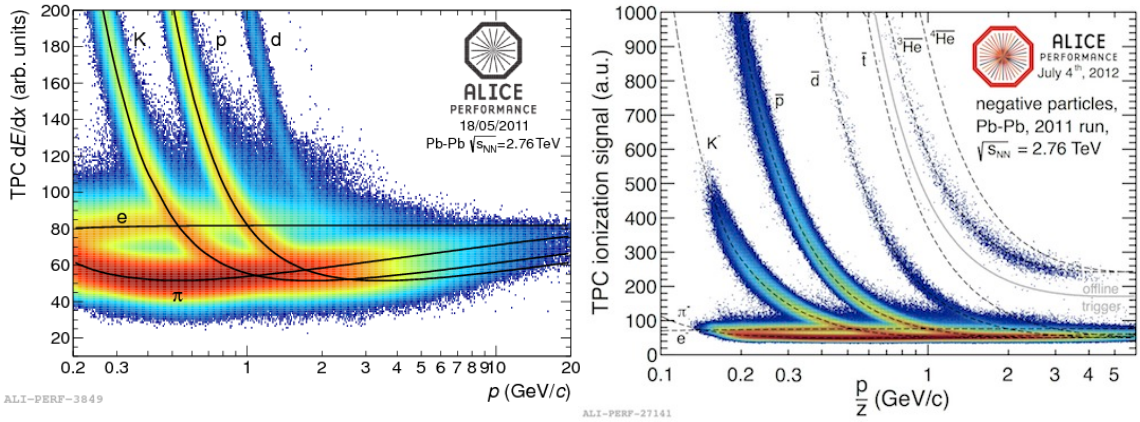

Figure 4.7: $\frac{dE}{dx}$ distributions for different species in TPC along with the corresponding predicted curves using Bethe-Bloch formula.

4.4 Correction procedure

4.4.1 Efficiency correction

In order to draw precise physics conclusions, results need to be corrected for limited efficiencies due to finite detector acceptance and specific analysis procedures. In principle to achieve this, a differential study needs to be done as a function of p_T, η and ϕ. As we discussed in the formalism, in order to cancel out the inefficiencies in the active detector volume, we form a pair ratio in which most acceptance effects cancel out. This technique does not correct for the inefficiencies and acceptance loss caused by the tracks which do not pass through the active detector volume. For this effect we perform a Monte Carlo (MC) simulation study in two stages. In the first stage, we generate a heavy-ion event using an event generator called HIJING [76]. We call this the Generator level MC. In the second stage we do a detector response simulation using GEANT [77] for the generator level particles. After the second stage, we obtain the Reconstructed MC. Finally the Reconstructed to Generated ratio gives the efficiency. We then correct the results with the obtained efficiency by applying the factor in the pre-factor $\sqrt{\rho'}$. In principle the Reconstructed level tracks should be similar to those seen the actual data. Otherwise, we lose confidence in the simulation and the model.

Figure 4.8 (left panel) shows the single particle tracking efficiency as a function of p_{T} obtained with HIJING for different centrality classes. The right panel shows a comparison of tracking efficiency for p-p and Pb-Pb systems.

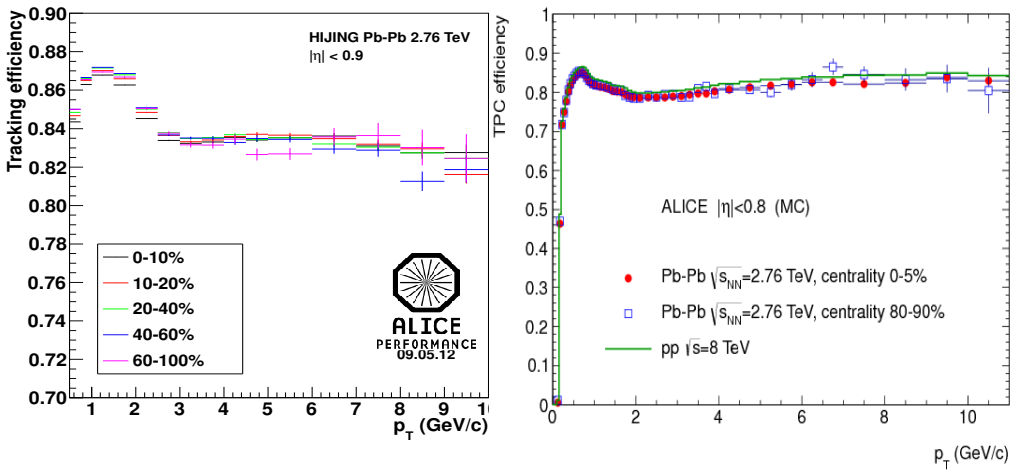

Figure 4.8: HIJING simulation for the tracking efficiency in ALICE detector [176].

4.4.2 Two-Track Efficiency

When TPC tracks with similar momentum and angle cross and/or share TPC clusters, the efficiency at small angles can be reduced due to merging. Thus, we are trying to increase the efficiency by increasing the purity of the sample. By applying a two-track efficiency cut, which removes pairs with tracks that are too close to each other. This cut is applied to the same event as well as the mixed event correlations in order to remove two track effects for the correlation function.

4.4.2.1 Merging correction

This method has been developed by the another working group in the ALICE collaboration, and is widely used in di-hadron correlations (triggered jet shape[176], pp, etc). It is based on cuts on the distance of closest approach of the two tracks within

the TPC. This distance is calculated from the track parameters using:

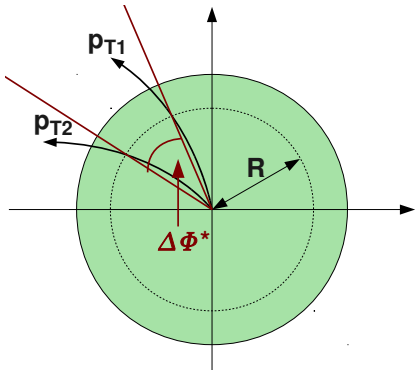

Figure 4.9: angular distance in transverse plane

$$\Delta\varphi^* = \Delta\varphi + arcsin\frac{z_1 eB_z r}{p_{\mathrm{T},1}} - arcsin\frac{z_2 eB_z r}{p_{\mathrm{T},2}} \tag{4.22}$$

where e is the electron charge, B_z the magnetic field in z direction, z the sign of the particle, and r the radius in the TPC. For the nominal field of 0.5T, r in m and p_T in $GeV/c, B_\mathrm{z}e = 0.075$. The two arcsin terms consider the curvature in the magnetic field, thus $\Delta\varphi^*$ is the distance in φ -direction at the radius r. To cut on the distance of closest approach, $\Delta\varphi^*_{\mathrm{min}}$, the smallest $\Delta\varphi^*$ within the TPC radius (0.8 - 2.5 m), has to be found. Pairs are removed which satisfy the condition:

$$|\Delta\varphi^*_{\mathrm{min}}| < 0.02, |\Delta\eta| < 0.02 \tag{4.23}$$

4.4.3 Wing correction

The di-hadron correlation structure has a relative rise in the region $\Delta\phi = \pi$ along $\Delta\eta$, and this is not expected from a known physical process. This structure is known as the "wing". Our understanding regarding the origin of the wing structure in the correlation function is not complete at the moment. Nevertheless, studies show that we can minimize the effect by applying strict cuts to the event-mixing procedure. Generally, we mix events with less than a 2 cm primary vertex difference and within 5% centrality. In this analysis, however, we have used very tight mixing criteria (within 0.4 cm and 1% centrality). Consequently, statistics will be reduced, but this is not a big concern since for untriggered correlations we take all the charged hadrons; therefore, we are not statistically limited. We explored the effect of changing the number of events we mix, since it is possible that the ratio of the same events to mixed events causes a rise in large $\Delta\eta$ as a result of a slightly narrower mixed event distribution. This was actually the case in the high p_{T} region, but we were able to fix the issue by implementing multiple event mixing. This gives at least one possibility of the origin of the wing structure. Still, the strongest wing is at the lowest $p_{\mathrm{T}} > 0.15 GeV/c$, so further understanding and studies explanation are needed. Since we have observed wings in other analyses (triggered, jet shape,..etc), it was decided to look at the generated and reconstructed level in a more sophisticated MC event generator called AMPT (A Multi Phase Transport model [96]).

4.4.4 Monte Carlo Simulations

The AMPT model uses the Heavy Ion Jet Interaction Generator (HIJING) to generate the initial conditions, then it propagates the parton through Zhangs Parton Cascade (ZPC)for modeling partonic scatterings, before using the Lund string fragmentation model or a quark coalescence model for hadronization and finally A Relativistic Transport (ART) model for treating hadronic scatterings. The model gives a comprehensive description of all dynamic stages of a relativistic heavy-ion collision.

4.4.4.1 Monte Carlo (AMPT)

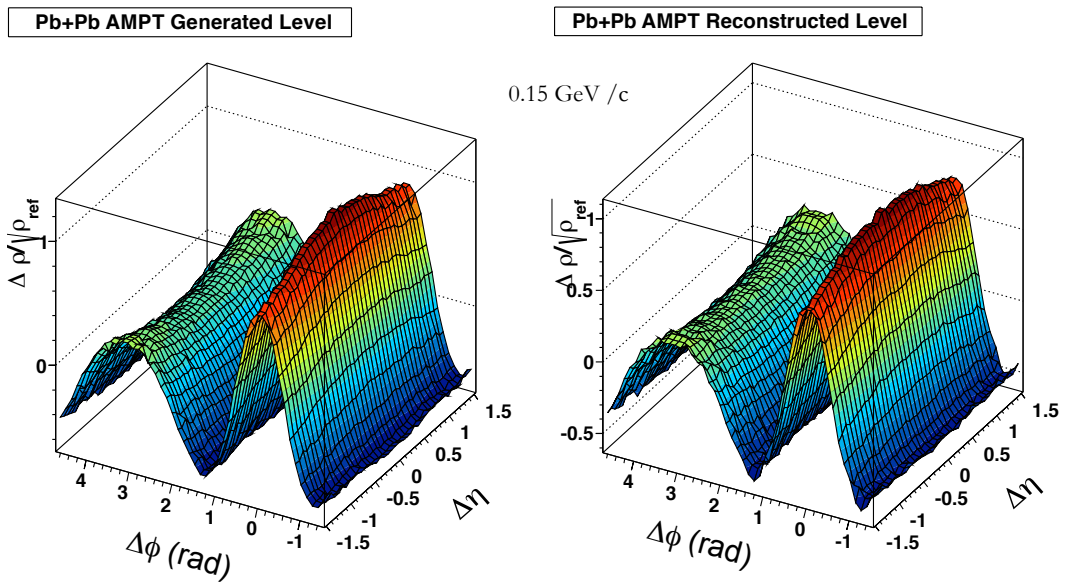

Figure 4.10: Generated and reconstructed level AMPT

As shown in Figure 4.10, even in the MC model, we can clearly see the wings at generator level.

4.4.4.2 Momentum evolution of AMPT

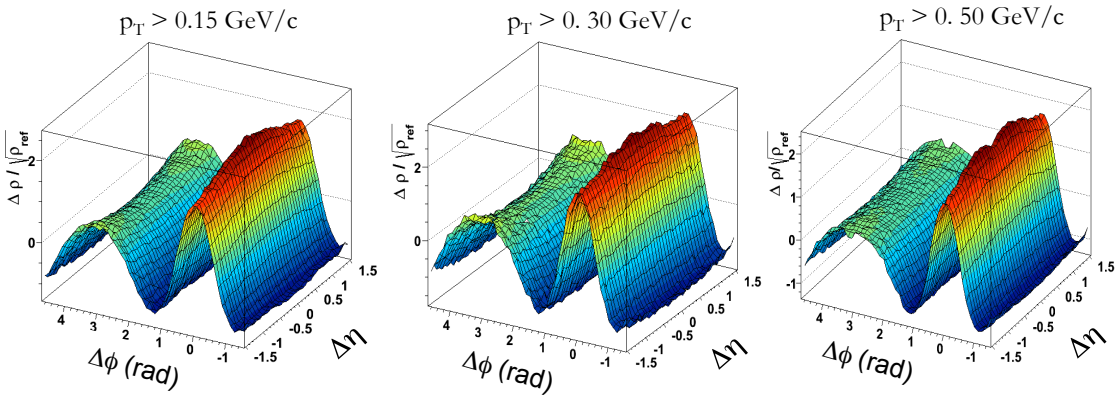

Figure 4.11: Generated level AMPT as a function of p_T

In order to obtain more information on the wing structure we have studied its momentum dependence. Figure 4.11 shows the first three bins of the momentum evolution for the MC events. It is observed that the wing structure indeed has a momentum dependence. On the reconstructed level, we observe similar effects (Figure 4.12). Furthermore, a double-hump like structure on the same side is observed in this low p_T range.

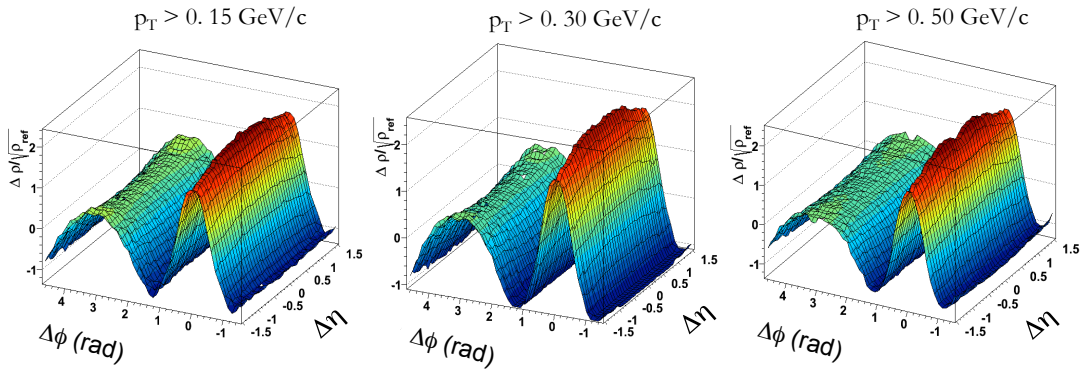

Figure 4.12: Reconstructed level AMPT as a function of p_T

Centrality dependence of the wing

In Figure 4.13, we show an away-side projection to investigate the centrality dependence of the wings. It appears the wings are relatively stronger in central events.

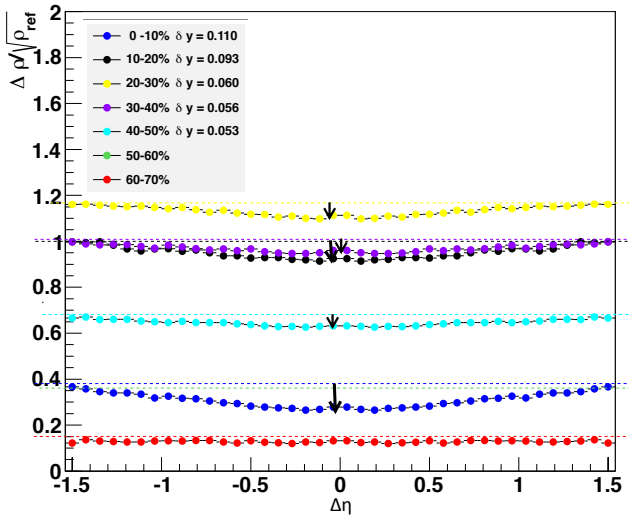

Figure 4.13: The centrality evolution of the away-side wing.

At this point our understanding is that the structure could either be caused by a physics process or by the way the correlation function is constructed. Since the effect is small, in either case we decided to report the wings as a systematic uncertainty and to subtract the wing structure in the analysis by using a simple functional fit (polynomial).

Wing correction via subtraction

The subtraction of the fit function results (see Chapter 5) from the data yields a residual, as shown in the upper-right frame of Figure 4.14. This residual is projected

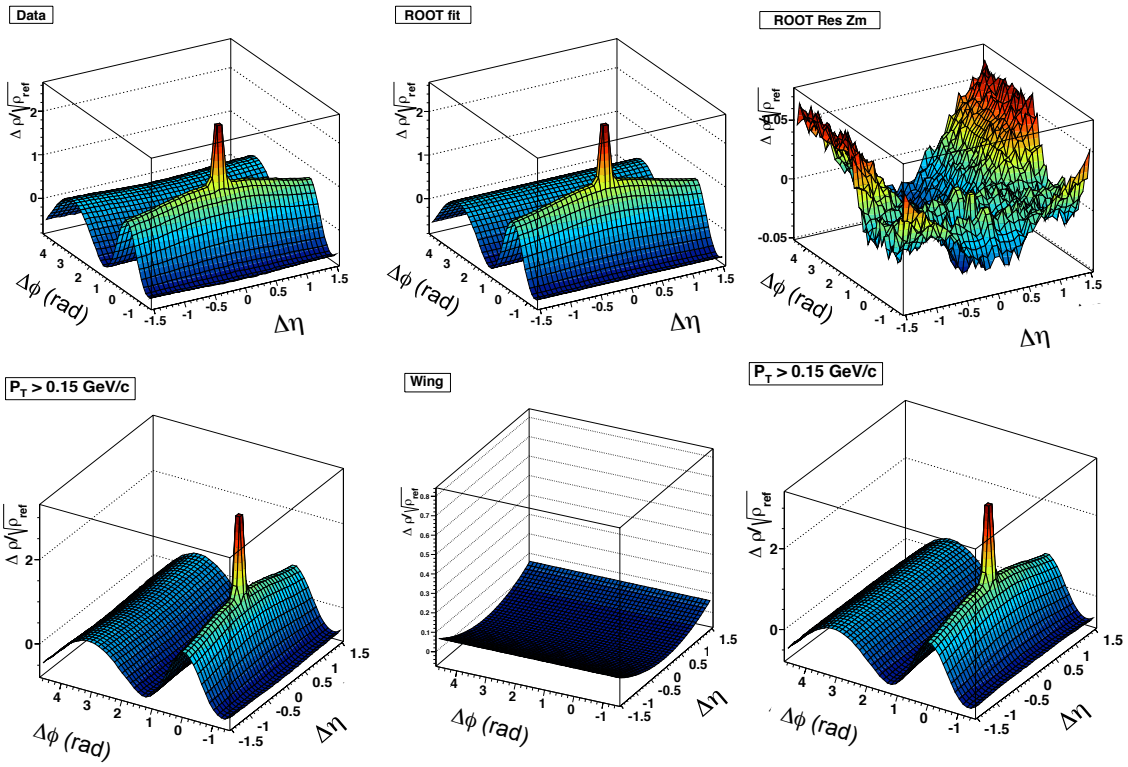

Figure 4.14: Wing correction technique applied

and fitted with a quadratic polynomial. Then, the modeled wing (bottom middle plot) is subtracted from the data. Here the correlation structure for $p_{\mathrm{T}} > 0.15$ GeV/c is shown as an example. Figure 4.15 shows the correlation structure before and after the acceptance correction.

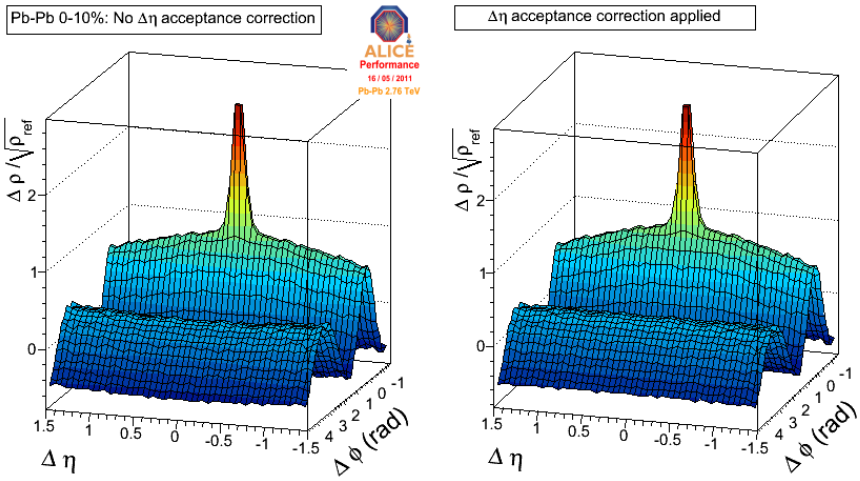

Figure 4.15: $\Delta\eta$ acceptance (wing) correction [174].

4.5 Fit model and procedure

In this section we discuss the modeling of the untriggered di-hadron correlation functions in terms of flow and non-flow. We are modeling the flow with a Fourier decomposition, and are modeling the non-flow with an asymmetric 2D Gaussian on the nearside.

4.5.1 Direct Fourier decomposition

4.5.1.1 Using a 2D fit

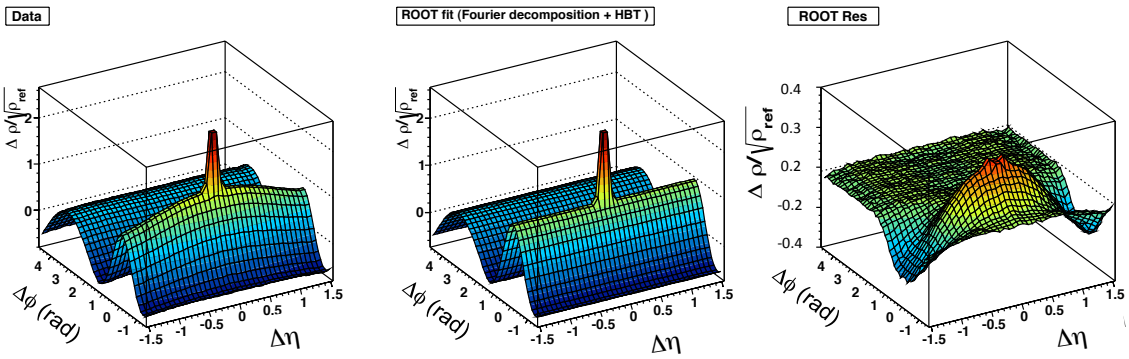

Figure 4.16: The fit function with a Fourier decomposition only.

When using only the Fourier series in our fit (see Figure 4.16), it is evident that we need another component to model the data. Ideally, as this residual should be as flat. Consequently, we modeled the non flow with another Gaussian. .

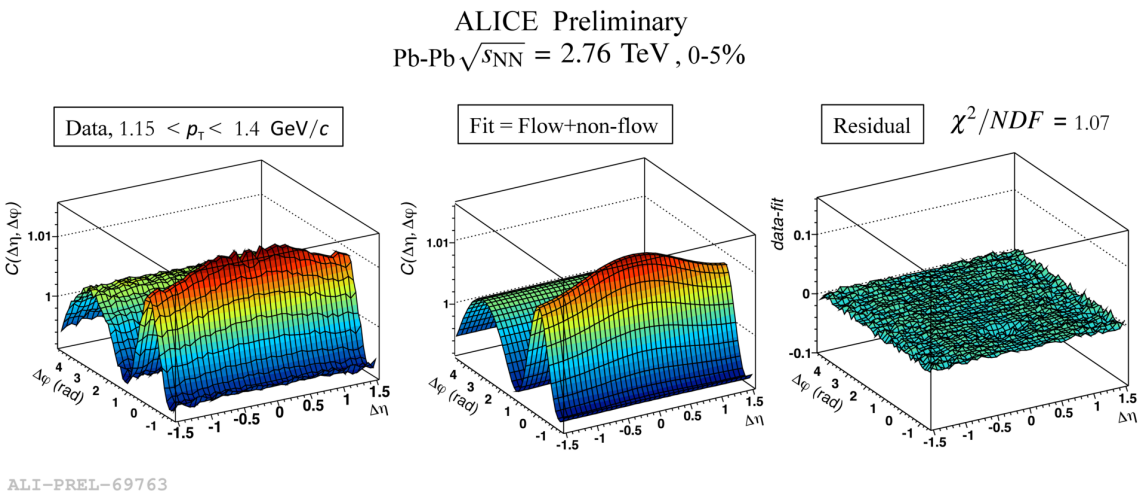

Figure 4.17: The fit function with a Fourier decomposition and a 2D Gaussian.

4.5.2 Fourier decomposition with a 2D Gaussian

Figure 4.17 shows the effect of using a fit function with a Fourier decomposition and a 2D Gaussian. The right frame shows the residual, which is a significant improvement over Figure 4.16. The residual is much flatter, as evidenced by the much lower χ^2/NDF of the second fit. When we projected the residue on either $\Delta\eta$ or $\Delta\phi$, there was no significant structure left. At low momentum, $p_{\mathrm{T}} < 1GeV/c$, the HBT (this will be described later) peak is visible. In this analysis, we remove this narrow peak by fitting a exponential function at $\Delta\eta$,$\Delta\phi$=0.

Final fit decomposition

Figure 4.18 shows the decomposed components of the fit function and Eq. 4.24 shows the mathematical form of the fit function. The well known HBT phenomena, quantum interference effects between detected identical particles with similar relative

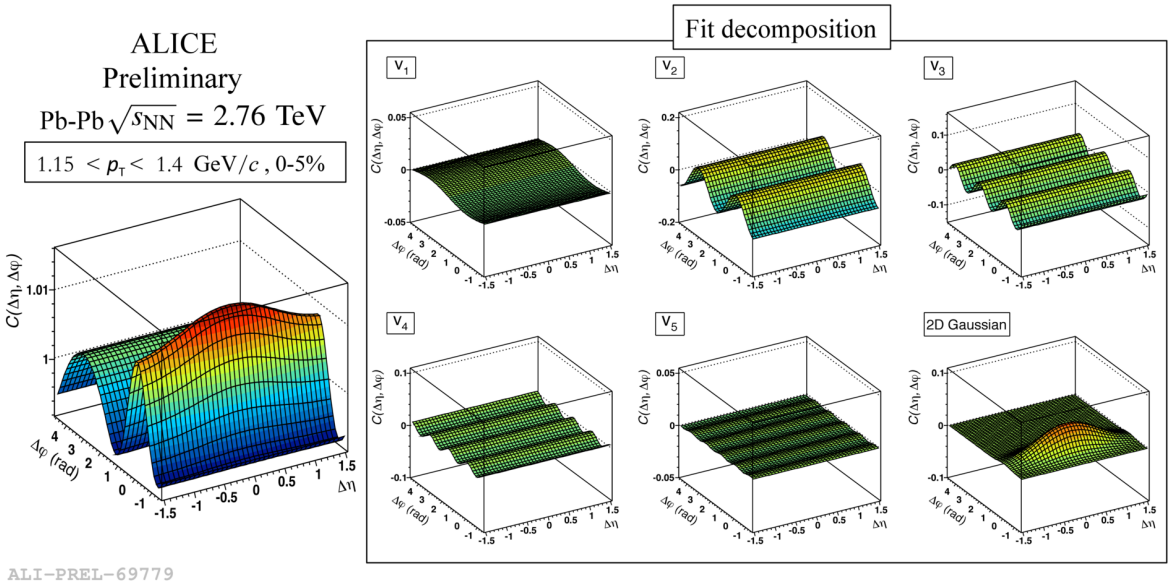

Figure 4.18: The fit function with v_n (n = 1, 2, 3, 4, 5) and 2D Gaussian

momentum, gives rise to small angle correlations in our correlation function. This results in a narrow peak around $\Delta\eta$, $\Delta\phi = 0$. In order to model the HBT peak(can be seen in Figure. 4.5) at low p_{T}, another exponent (see Eq. 4.25) is added to the equation 4.24.

$$F = a_0 + a_1 cos(\Delta\phi) + a_2 cos(2\Delta\phi) + a_3 cos(3\Delta\phi) + a_4 cos(4\Delta\phi) + a_5 cos(5\Delta\phi) + a_6 exp\left\{-\frac{1}{2}\left[\left(\frac{\Delta\eta}{a_7}\right)^2 + \left(\frac{\Delta\phi}{a_8}\right)^2\right]\right\} \tag{4.24}$$

$$a_9 exp\left\{-1\left[\left(\frac{\Delta\eta}{a_{10}}\right)^2 + \left(\frac{\Delta\phi}{a_{11}}\right)^2\right]^{1/2}\right\} \tag{4.25}$$

Table 4.2 shows the interpretation of the fit parameters used in equations 4.25 and

Table 4.2: A brief summary of the fit parameters

Parameter	Parameter name	Description
a_0	Offset	Estimates a negative offset for positive correlation structures in the data
a_1	-cos($\Delta\phi$) amplitude	local and global momentum conservation
a_2	cos(2$\Delta\phi$) amplitude	elliptic flow
a_3	cos(3$\Delta\phi$) amplitude	triangular flow
a_4	cos(4$\Delta\phi$) amplitude	quadrangular flow
a_5	cos(5$\Delta\phi$) amplitude	pentagonal flow
a_6	2D Gaus. amplitude	amplitude of the ridge
a_7	2D Gaus. $\Delta\eta$ width	$\Delta\eta$ width of the ridge
a_8	2D Gaus. $\Delta\phi$ width	$\Delta\phi$ width of the ridge
a_9	2D Expo. amplitude	amplitude of the HBT peak
a_{10}	2D Expo. $\Delta\eta$ width	$\Delta\eta$ width of e^+e^- contamination
a_{11}	2D Expo. $\Delta\phi$ width	$\Delta\phi$ width of e^+e^- contamination

4.26. In the fitting procedure a χ^2 minimization is used by applying the standard package in the ROOT [74] . All the parameters were fitted simultaneously without constraining the parameters except the Gaussian widths were set to be positive.

Chapter 5

Results

In this chapter, we first described the previous studies of di-hadron correlations and the related measurements. As mentioned in section 1.4, the motivation behind the analysis of relativistic heavy-ion collision data is to study the QGP signatures. In this thesis work, the key signatures we analyze are classified as flow and non-flow measurements. Firstly, previous studies of non flow will be introduced. Then, previous measurements of flow will be shown. Finally, the results from this analysis will be shown. The implications of the results related to formation of QGP and the properties of QGP will be discussed in chapter seven.

5.1 Previous studies of di-hadron correlations

As introduced in chapter 4, correlations and fluctuations can provide essential information on the nature of the medium produced in ultra- relativistic heavy-ion

collisions. An enhanced correlated yield on the near side ($\Delta\phi \approx 0$) at large pseudo rapidity separations ($\Delta\eta >> 0$) has been observed in previous di-hadron correlation studies at RHIC [22,76,77] and were quite surprising. The correlation structure corresponding to this yield, which is referred to as the "ridge", was first observed in [22] for all charged-particle pairs in the low p_t ($p_t < 2$ GeV/c) region. Later on it was also observed for trigger particles in the intermediate p_t ($4 < p_t < 6$ GeV/c) range [76]. In order to further investigate the dependence of the jet production and successive hard scattering on the novel ridge structure, the transverse momentum region was pushed p_T up to 9 GeV/c [77]. It was observed that the ridge structure exists up to the highest possible trigger p_t within the given statistical reach.

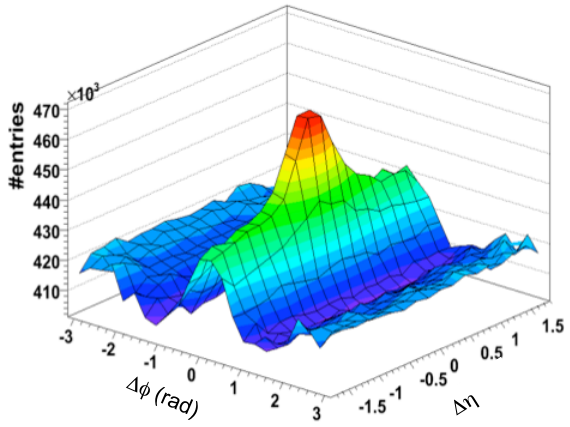

Figure 5.1: Raw $\Delta\phi$ x $\Delta\eta$ di-hadron correlation function in central Au + Au collisions for $3 < p_T^{trig} < 4$GeV/c and $p_T^{assoc} > 2$GeV/c. (Background and flow subtracted).

Figure 5.1 displays the main result, namely a near side yield that exhibits (a) a distinguishable peak around ($\Delta\eta$,$\Delta\phi$) = (0, 0) which is expected from jet fragmentation, and (b) an enhancement of correlated yield at large $\Delta\eta$.

Further studies were carried out at LHC with the ALICE experiment with higher

center of mass energy. Figure 5.2 shows the di-hadron correlation function at 2.76 TeV at higher momentum trigger. The flow and non-flow components of the correlation functions were extracted by placing an $\Delta\eta$ gap in the correlation structure. This technique does minimize the non-flow presence in the flow measurements.

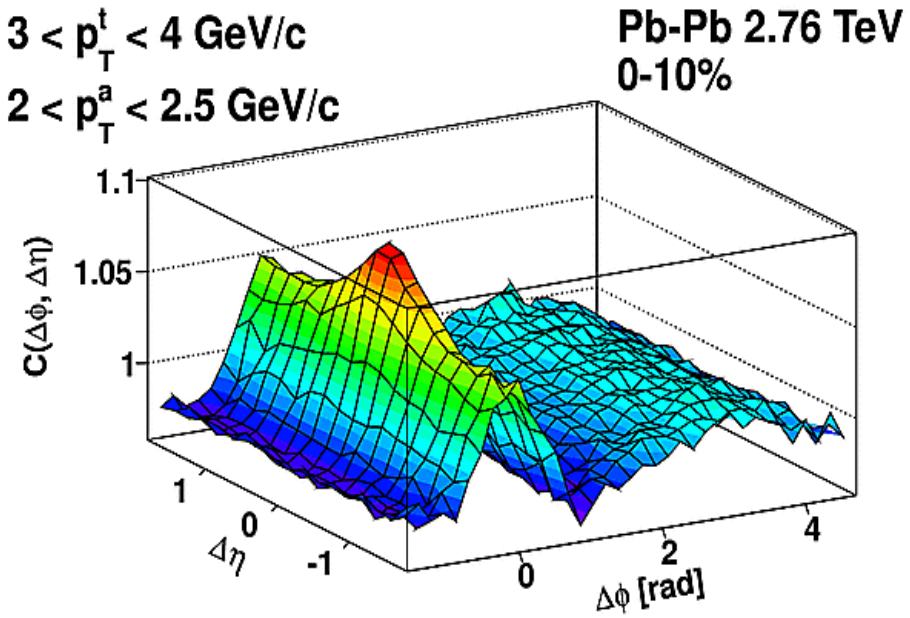

Figure 5.2: The di-hadron correlation function in central Pb + Pb collisions for $3 < p_T^{trig} <$ 4GeV/c and $> p_T^{assoc}$ 2.5 $>$ 2GeV/c in ALICE experiment.

In this thesis work, we propose a multi-component fit method to extract flow and non flow signals with higher purity. Cleaner flow parameters should ultimately lead to better estimates of η/s value of the QGP. Thus measuring flow with minimal presence of non-flow becomes an essential task. This will be discussed in chapter seven in detail.

5.2 Previous studies of flow

The quark-gluon plasma is a state of matter whose existence at high-energy density is predicted by quantum chromodynamics. The creation of this state of matter in the laboratory and the study of its properties are the main goals of the ultra relativistic nuclear collision program. One of the experimental observables that is sensitive to the properties of this matter is the azimuthal distribution of particles in the plane perpendicular to the beam direction. When nuclei collide at nonzero impact parameter (non-central collisions), the geometrical overlap region is anisotropic. This initial spatial asymmetry is converted via multiple collisions into an anisotropic momentum distribution of the produced particles.

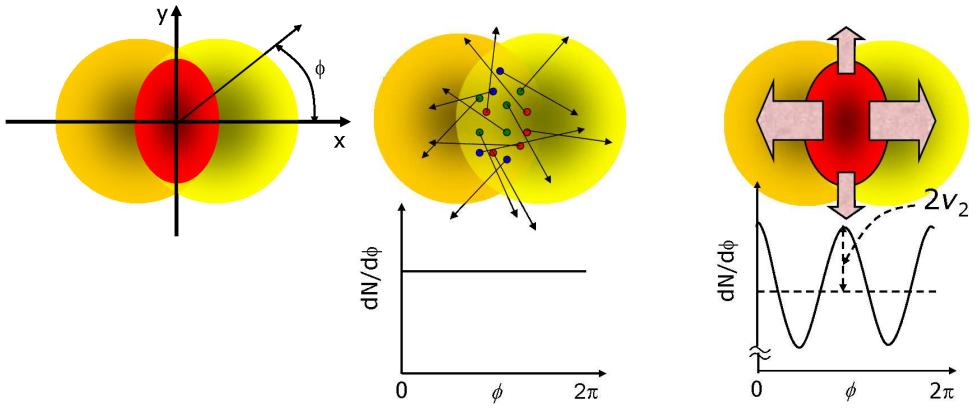

(a) Large mean free path (b) Small mean free path

Figure 5.3: Possible azimuthal patterns based on the mean free path of the produced particles between collisions

Figure 5.3 gives a graphical view of the anisotropic flow signal. If no medium formation has occurred, the distribution of particles in the azimuth should be an

uniform distribution (see the middle plot of the figure 5.3). Anisotropic flow measurements are based on an analysis of azimuthal correlations and might be biased by contributions from correlations that are not related to the initial geometry, which are called non-flow. The most frequently used method in flow analysis is the standard event plane method (EP). First, the true reaction plane angle is estimated. Then and all particles azimuthal angles are correlated to this estimated plane in order to get the flow harmonics v_n. This method is probably biased by contributions from non-flow. To improve the anisotropic flow measurements advanced methods based on genuine multi-particle correlations (cumulants) have been developed which suppress systematically the non-flow contribution [54-56]. The Fourier coefficients as a function of p_{T} shown in figure 5.4 are obtained by using the "cumulants" method.

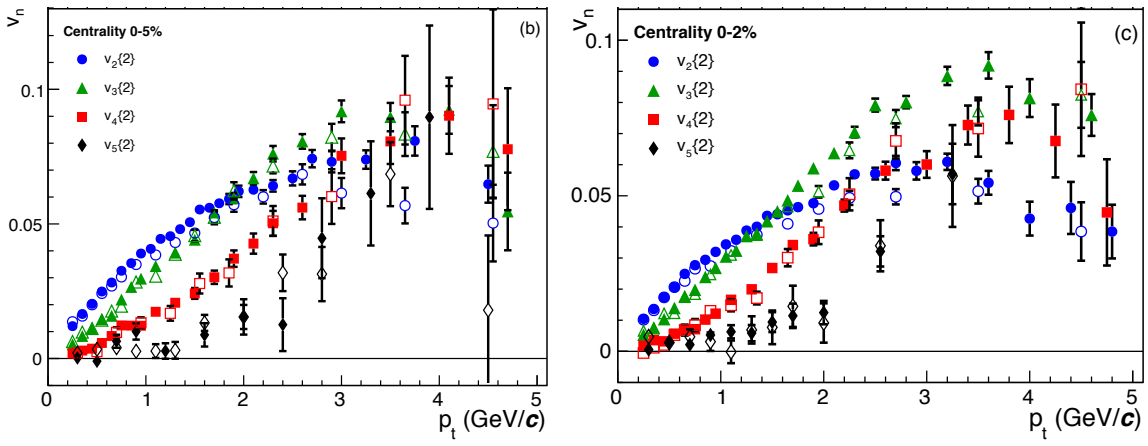

Figure 5.4: Higher-order Fourier decompositions of the anisotropic momentum distribution for central heavy-ion collisions.

Analysis approach for dissertation study

In order to measure flow with higher precision and investigate the cause of the ridge structure, we focus on the correlation structure in the most central events (0-10%). This centrality bin corresponds to the highest possible energy density created in a heavy-ion collision for any given system (e.g., Pb-Pb). If a QGP is formed, it is likely to be formed in these collisions and we can study the relation between the novel correlation phenomena and QGP. Finally, considering the centrality trend observed in data (Figure 5.5), we expect the correlation strength to be largest in the 0-10% centrality bin. In our study the transverse momentum evolution of di-hadron correlations is obtained by raising the lower p_T acceptance for both charged-particles. We first report our initial results of the Pb-Pb centrality dependence, and then report the the p_T evolution study using Pb-Pb collisions at $\sqrt{s_{NN}} = 2.76$ TeV.

5.3 Centrality evolution studies

As we discussed in section 3.2, our di-hadron correlation analysis technique uses all charged-particle pairs(untriggered analysis). From the measured centrality evolution study [175] (Figure 5.5) it is evident that the ridge structure starts to appear with increasing centrality in heavy-ion collisions. Di-hadron correlations in peripheral heavy-ion collisions are expected to show a similar structure than in elementary collisions, which is confirmed by comparing inclusive p + p collisions to peripheral Pb-Pb collisions. However, even in the most peripheral 70-80% bin, we still observe

a slight relative $\Delta\eta$ elongation in the Pb+Pb 2.76 TeV system. This observation is directly related to the density of the system created in the collision.

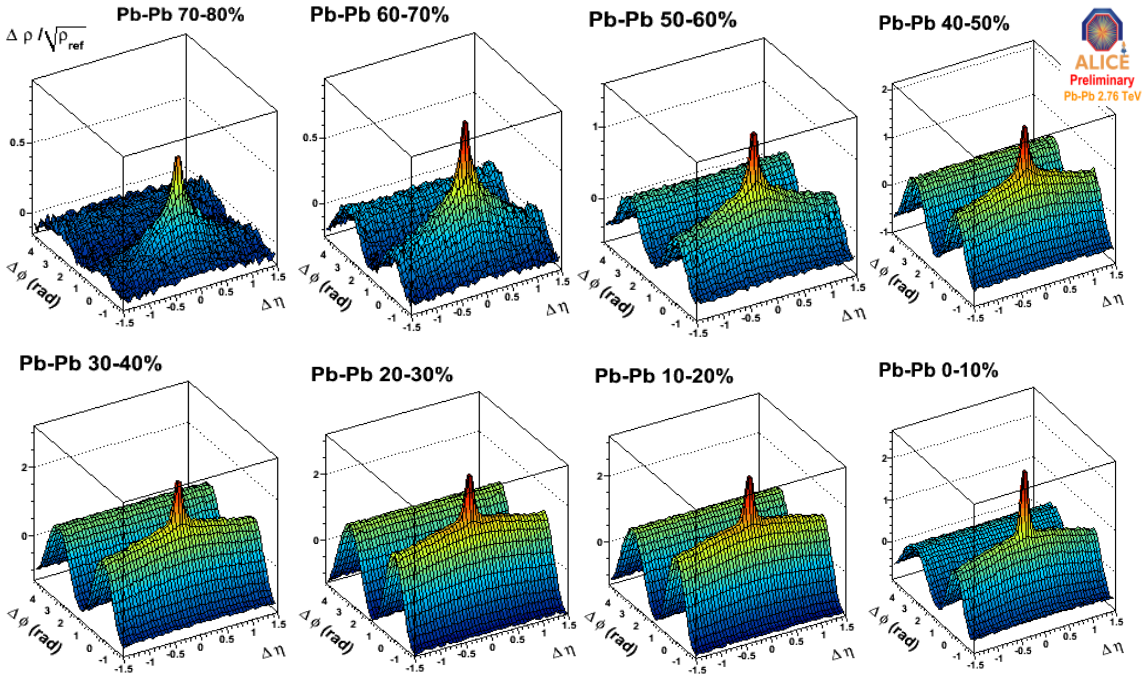

Figure 5.5: The centrality evolution of di-hadron correlations for $p_T > 0.15$ GeV/c [175].

In order to determine the underlying physics origins of this correlation structure, an empirical model fit function based on model components discussed in chapter four has been adopted. After considering all possible correlation contributions, the empirical model function takes the following form. The corresponding 11 fit parameters are denoted by a_i $(i = 0, 1, ..., 10)$ which are described in table 5.1. Figure 5.6 shows an example fit for central Pb-Pb 2.76 TeV data. The residual structure (data - fit) is a proof for the good fit quality (χ^2/DOF value ≈ 1.1) we get from our standard ROOT minimization method [74]. Figure 5.7 shows an example decomposition using

the same fit function in a particular momentum bin.

$$
\begin{aligned}
F = a_0 &+ a_1 cos(\Delta\phi) + a_2 cos(2\Delta\phi) + a_3 cos(3\Delta\phi) + a_4 cos(4\Delta\phi) \\
&+ a_5 cos(5\Delta\phi) + a_6 exp\left\{-\frac{1}{2}\left[\left(\frac{\Delta\eta}{a_7}\right)^2 + \left(\frac{\Delta\phi}{a_8}\right)^2\right]\right\} \\
&+ a_9 exp\left\{-1\left[\left(\frac{\Delta\eta}{a_{10}}\right)^2 + \left(\frac{\Delta\phi}{a_{11}}\right)^2\right]^{1/2}\right\}
\end{aligned}
\tag{5.1}
$$

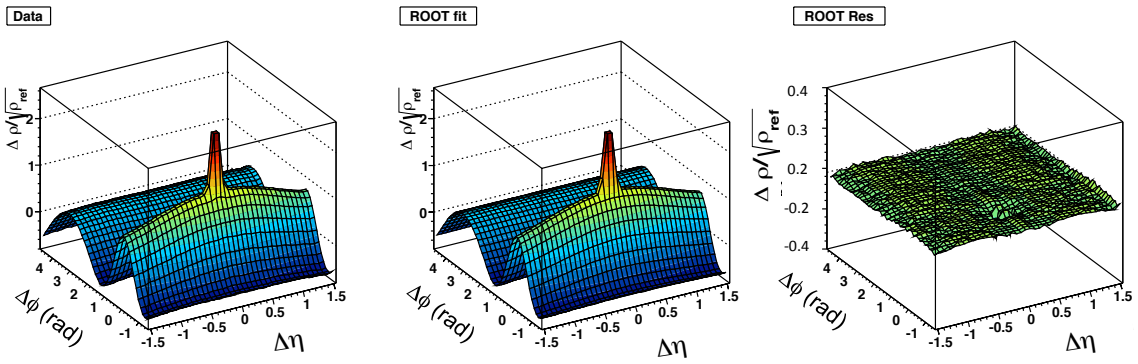

Figure 5.6: Example of a correlation function in $0-10\%$ Pb-Pb collisions (data, fit and the residual)

Figure 5.8 shows the extracted Gaussian parameters using the fit we described (excluding v_5) from the centrality evolution studies shown in Figure 5.5.

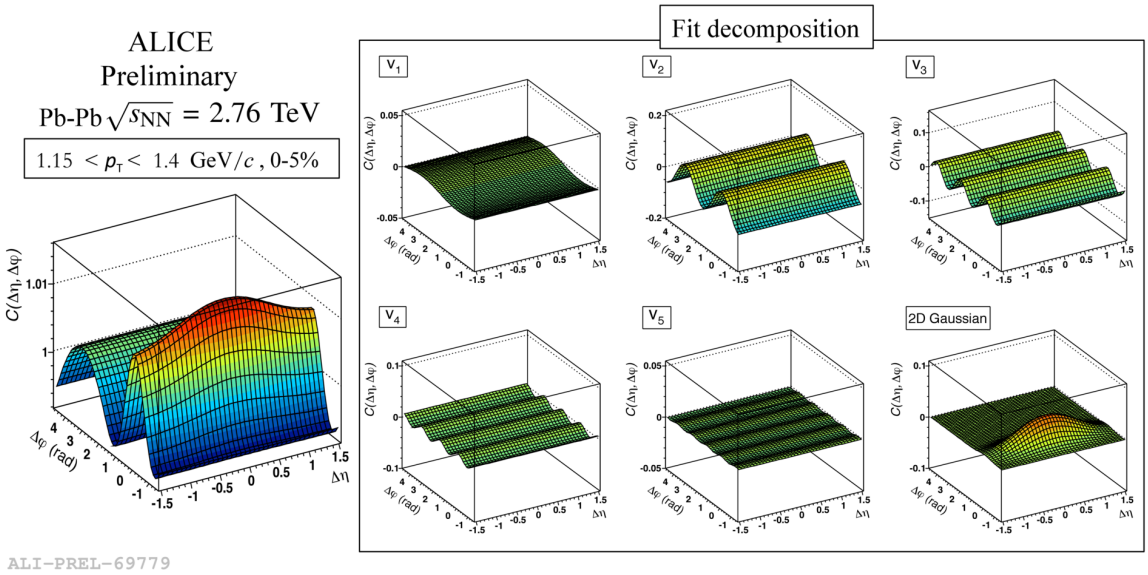

Figure 5.7: The fit function with v_n (n = 1, 2, 3, 4, 5) and 2D Gaussian

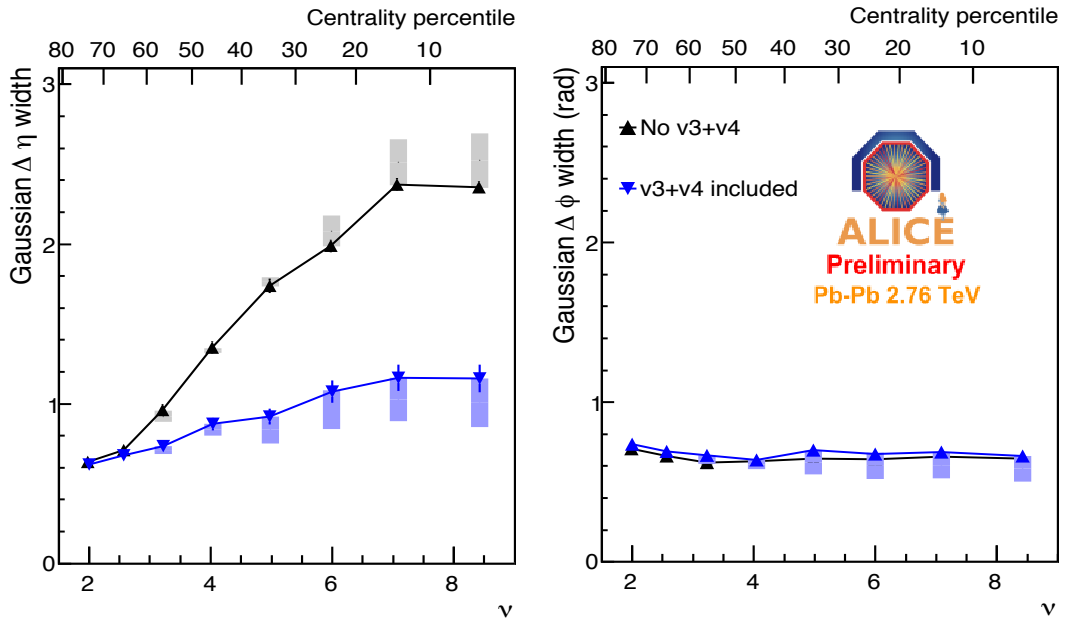

Figure 5.8: Extracted Gaussian parameters as a function of centrality in Pb-Pb $\sqrt{s_{NN}}$ = 2.76 TeV collisions. No v3+v4 refers to fits without higher harmonics, v3+v4 included refers to fits with higher harmonics [175].

Table 5.1: A summary of the fit parameters

Parameter	Parameter name	Description
a_0	Offset	Estimates a negative offset for positive correlation structures in the data
a_1	-cos($\Delta\phi$) amplitude	local and global momentum conservation
a_2	cos(2$\Delta\phi$) amplitude	elliptic flow
a_3	cos(3$\Delta\phi$) amplitude	triangular flow
a_4	cos(4$\Delta\phi$) amplitude	quadrangular flow
a_5	cos(5$\Delta\phi$) amplitude	pentagonal flow
a_6	2D Gaus. amplitude	amplitude of the ridge
a_7	2D Gaus. $\Delta\eta$ width	$\Delta\eta$ width of the ridge
a_8	2D Gaus. $\Delta\phi$ width	$\Delta\phi$ width of the ridge
a_9	2D Expo. amplitude	amplitude of the HBT peak
a_{10}	2D Expo. $\Delta\eta$ width	$\Delta\eta$ width of e^+e^- contamination
a_{11}	2D Expo. $\Delta\phi$ width	$\Delta\phi$ width of e^+e^- contamination

5.4 Transverse momentum dependence studies

The transverse momentum evolution of di-hadron correlations in the 0-10% centrality bin was mainly carried out to map the kinematic region neglected in previous studies [22,76,77]. We aimed to study the connection between the high and low p_T kinematic regions in the context of the "ridge" formation. At high p_T, we should be sensitive to jet physics, whereas at low p_T and intermediate p_T there are many convoluting effects such as, elliptic flow, string fragmentation, HBT, mini-jets, resonances and other possible novel QCD phenomena.

We first report our raw data spectra for Pb-Pb $\sqrt{s_{NN}} = 2.76$ TeV. Then we show the results after applying the corrections (explained in chapter 4). Next we present fit parameters as a function of mean p_{T}. Finally we compare our model study and related theoretical comparisons [98,99] in chapter seven.

5.4.1 Raw Correlation functions

The correlation functions reveal a smooth evolution of the near side structure as a function of the low p_T threshold for all particle pairs (see Figure 5.9 and 5.10). The long range correlation strength reduces at high p_T and the jet structure becomes more prominent. While the higher track density in Pb-Pb enables a better statistical reach in p_{T}, it also generates a dip at ($\Delta\eta = 0$, $\Delta\phi = 0$) for lower p_T threshold cuts. This is caused mainly by Coulomb repulsion between close tracks in a high

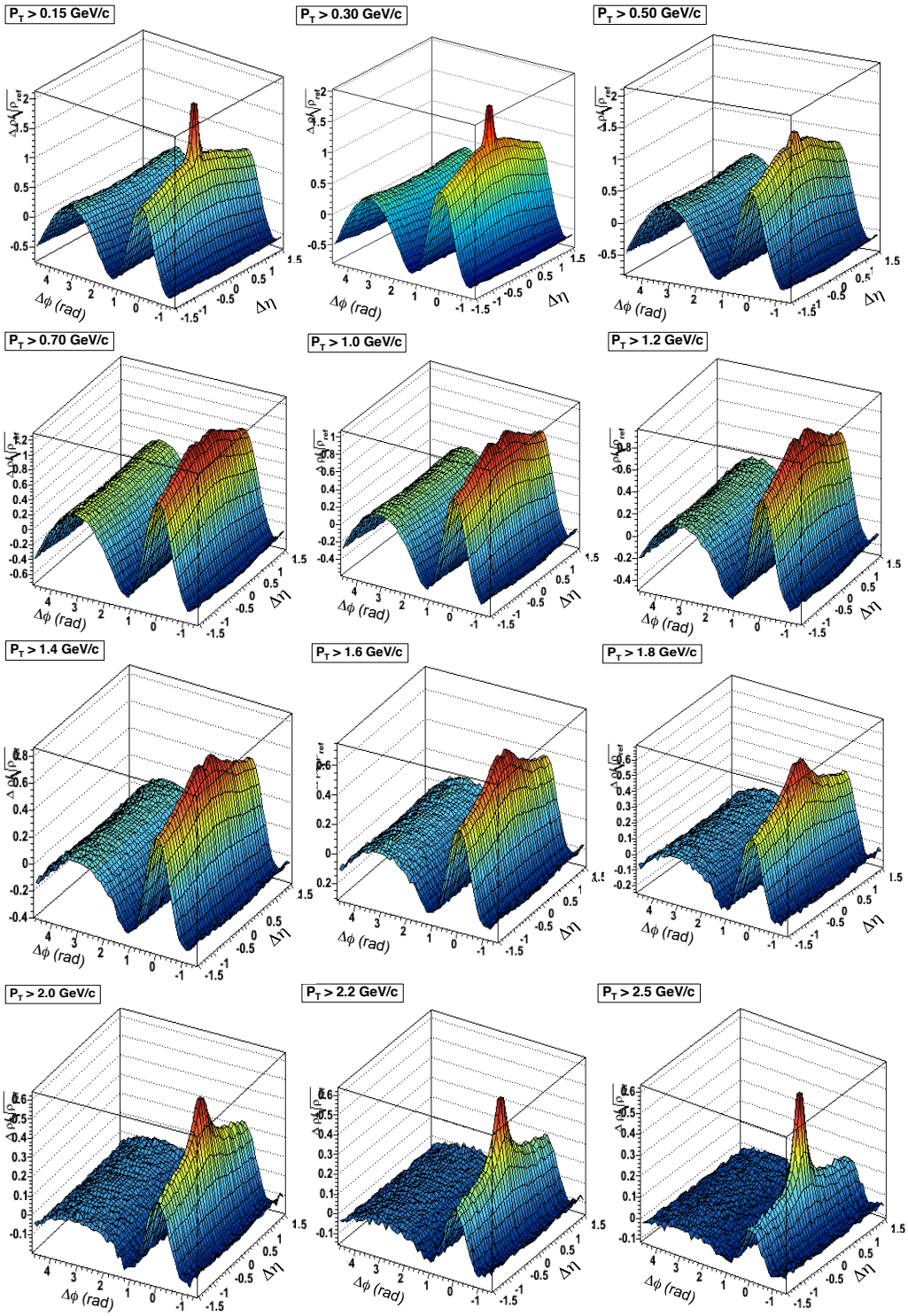

Figure 5.9: The uncorrected transverse momentum evolution for 0-10% data

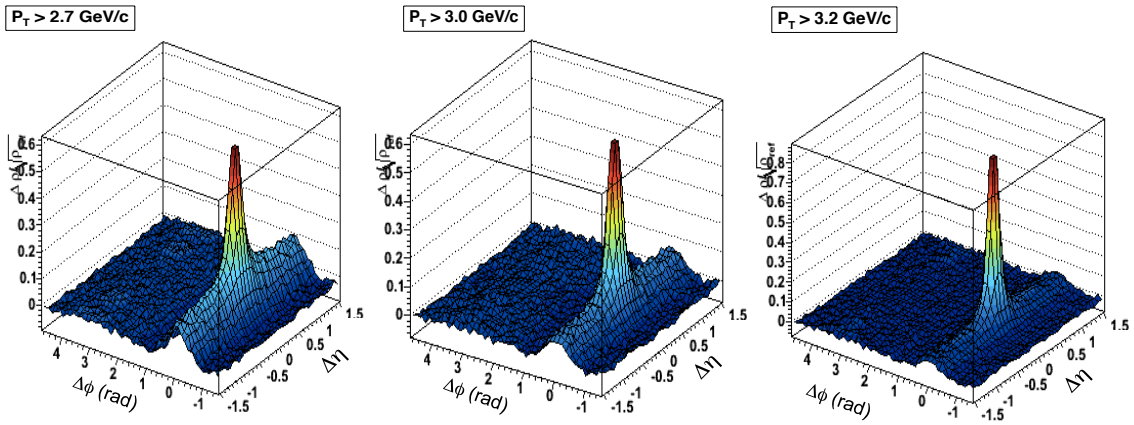

Figure 5.10: Transverse momentum evolution at higher momenta

track density environment. It is confirmed using charge dependent di-hadron correlations (will be discussed in detail in the systematic uncertainty estimation in chapter six). The like sign (++ and −−) charged pairs repel (Figure 5.9 mid p_T range) each other. A smaller dip structure at (0,0) remains even for unlike sign pairs (+−) which is due to tracking inefficiencies at small separation angles rejection criteria [58].

As we can observe in Figure 5.9, the inclusion of low p_T particles generates a structure on the near side compared to the structure at high p_T which is seen as a linear combination of a long range and a short range structure in $\Delta\eta$. Figures 5.11 and 5.12 show the two-track efficiency corrected momentum spectra. This correction minimizes the effect of coulomb repulsion. In these Figures the wing correction, which takes care of the slight enhancement at large $\Delta\eta$ in the away side long range correlations structure, has yet to be applied. Figures 5.13 and 5.14 show the spectrum with both corrections.

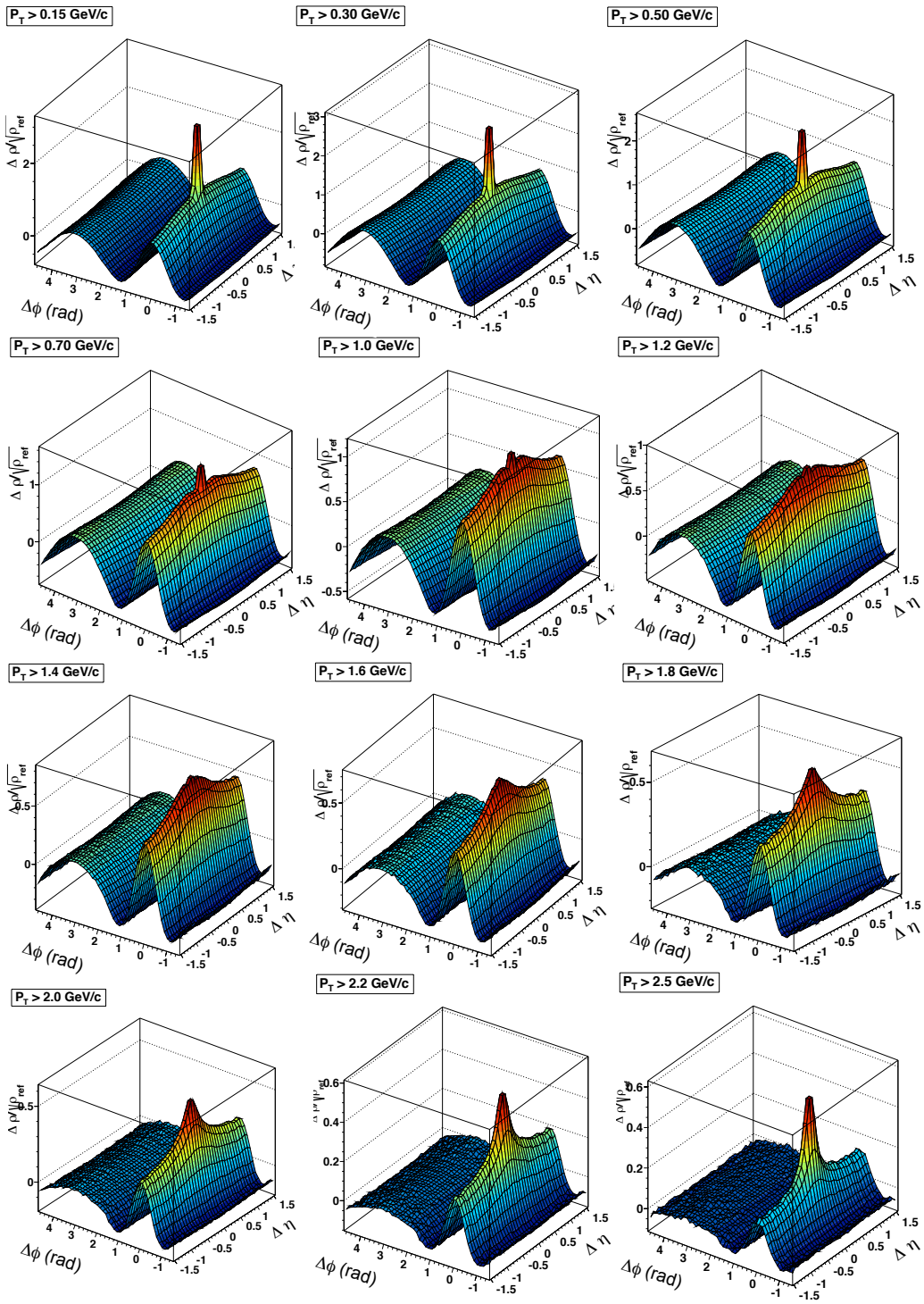

Figure 5.11: The two-track efficiency corrected p_T evolution for 0-10%

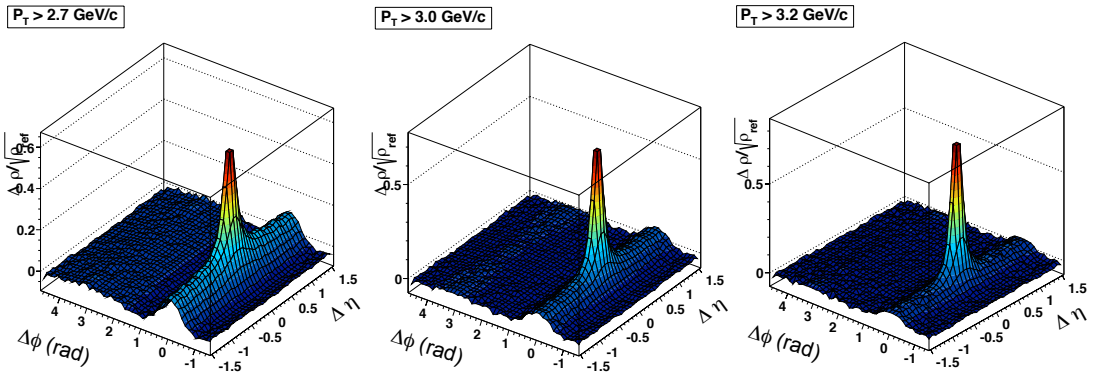

Figure 5.12: Transverse momentum evolution at higher momenta after the two-track correction

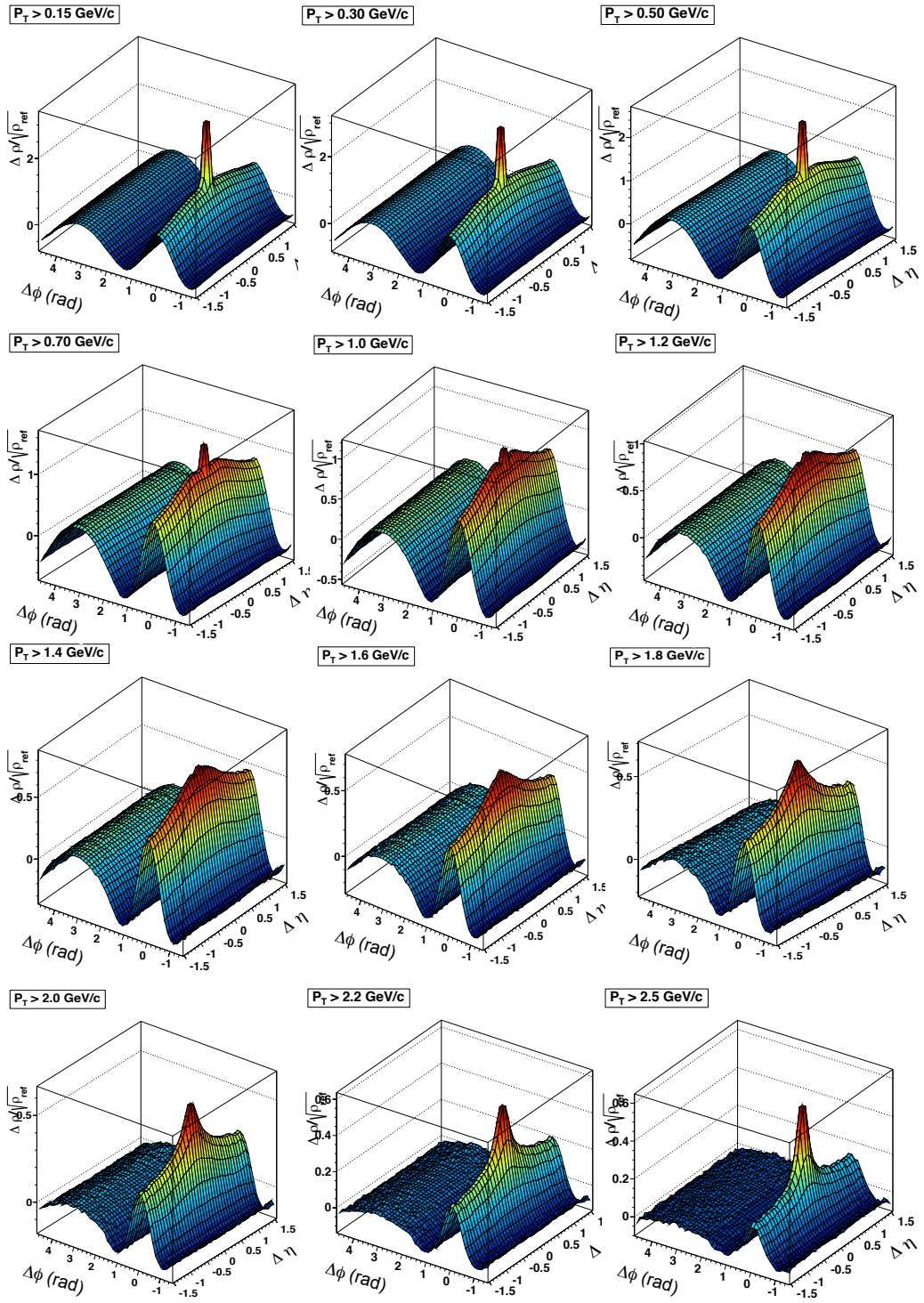

Figure 5.13: Transverse momentum evolution of di-hadron correlation in 0-10% centrality bin using Pb -Pb 2.76 TeV data.

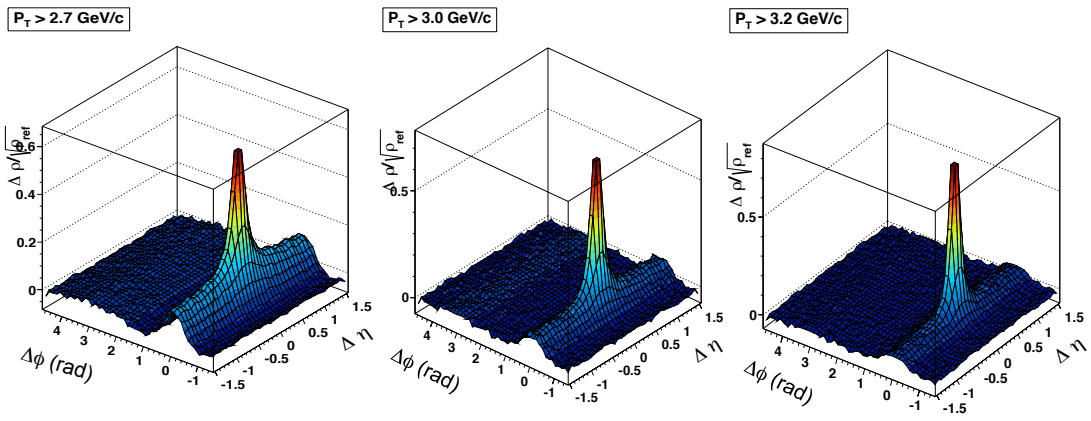

Figure 5.14: Transverse momentum evolution at higher momenta, after wing correction

5.4.2 p_{T} evolution in momentum windows

When we apply the lower-threshold p_T cut, the parameters extracted are reported as a function of mean p_T of a large momentum window. In order to investigate the contributions from a specific p_T range, narrow momentum windows are studied. On the other hand, the study in windows enables us to make comparisons with other independent measurements. Figure 5.15 shows the p_T evolution in momentum windows and the statistical fluctuations are visible compared to the integral method. The evolution of the correlations structures show similar trend to the integral method. The observed differences in extracted fit parameters were reported as a systematic uncertainty.

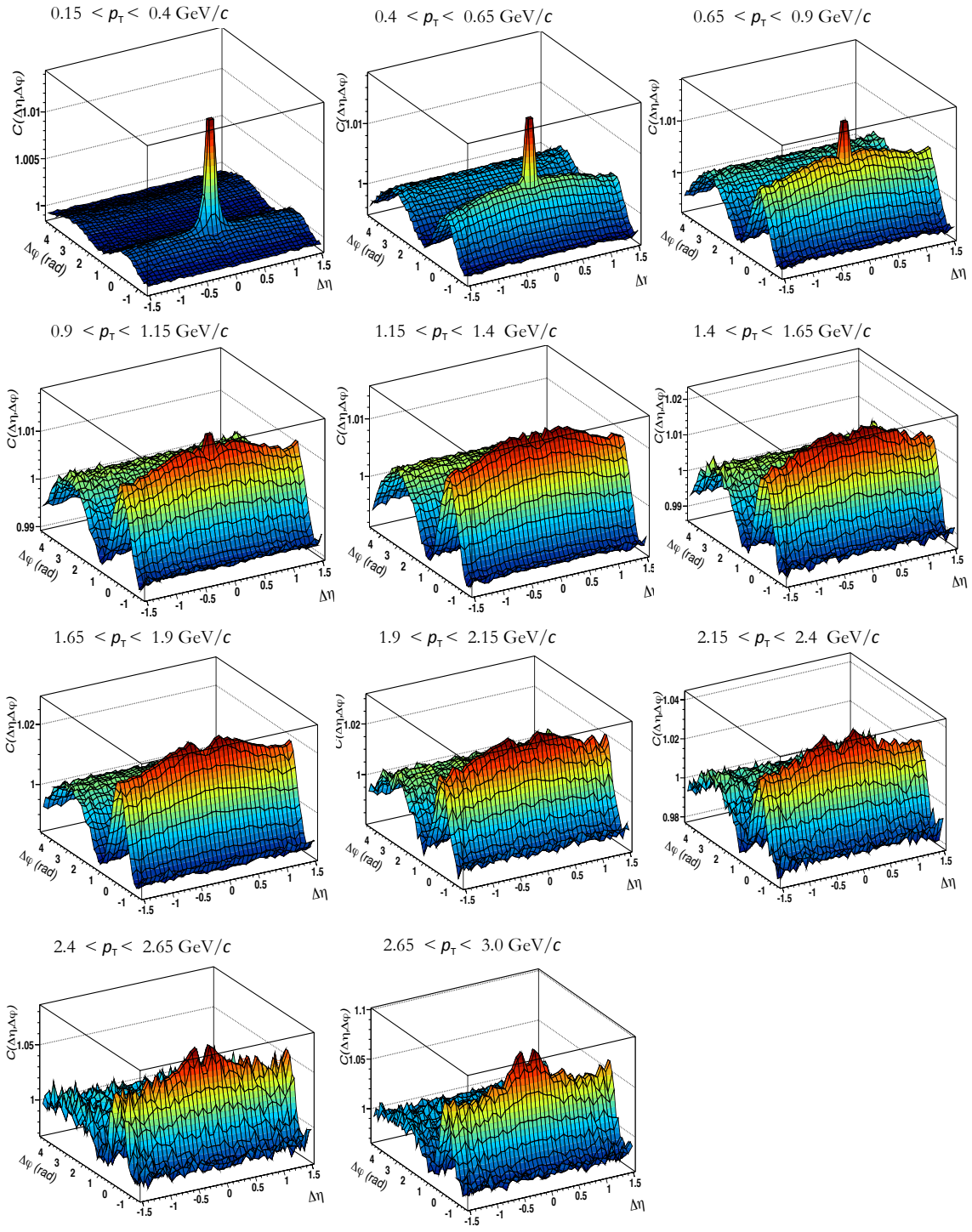

Figure 5.15: The momentum evolution of di-hadron correlations.

The fit quality and χ^2 test for goodness of fit

In order to test the fit quality we calculate the standard χ^2/DOF for $x_i (i = 1, 2, 3, ..., \nu)$ variables, the χ^2 is defined as:

$$\chi^2 \equiv \sum_{i=1}^{\nu} \frac{(x_i - \mu_i)^2}{\sigma_i^2} \tag{5.2}$$

where μ_i and σ_i^2 correspond to the mean and variance of the variable x_i respectively. Ideally we would expect that each term of the sum is one since the random fluctuation of the value x_i about the mean should be close to the variance. Therefore if we can choose μ_i and σ_i correctly, our χ^2 value should be equal to ν. The model function which defines the best μ_i values that satisfies this condition would describe the data well. If χ^2 becomes larger than ν given that our σ_i estimates are accurate, then the model function does not describe the data well. In our data, we calculate the σ_i which is the error on data, using square error propagation. The σ_i values are on the order of 10^{-3}. The χ^2 distribution with ν degrees of freedom is defined as:

$$f(\chi^2) = \frac{1}{2^{\nu/2}\Gamma(\nu/2)} e^{-\chi^2/2} (\chi^2)^{(\nu/2)-1} \tag{5.3}$$

with a mean of ν and a variance of 2ν. The distribution becomes symmetric for larger ν values even though it is highly skewed to the left for small ν values. In a test for goodness of fit, we have to consider the possibility that our x_i variables are not independent from each other for the most general case. Therefore, depending on

the number of relations or constraints (say r) between the variables x_i our degrees of freedom (ν) reduces to $N - r$. In our fit model study, x_i's are the bins in the $\Delta\eta$ x $\Delta\varphi$ space (625 in total) and the constraints are the number of parameters in the fit function (9 in total). This means the χ^2 for our fits should be close to 616 for our model study. Figure 5.16 shows the χ^2/DOF values for the model fit for different momentum bins.

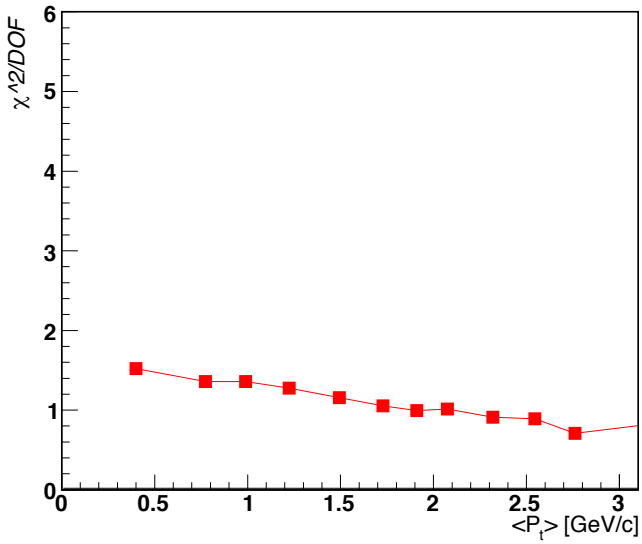

Figure 5.16: The value of χ^2/DOF as a function of transverse momentum.

5.4.3 Fit paramaters

5.4.3.1 Flow harmonics

Our model v_n parameters are not directly comparable to standard flow measurements. Measurements from di-hadron correlations need to be converted [82] using the following equation in order to be compared.

$$v_n(2D) = \sqrt{\frac{4\pi v_n(Fit)}{2(dN/d\eta d\phi)}} \tag{5.4}$$

In equation 5.4, $v_n(2D)$ represents the converted measure, $v_n(Fit)$ gives the extracted model fit value and $\frac{dN}{d\eta d\phi}$ is the charged-particle distribution within the selected acceptance of the di-hadron correlation function.

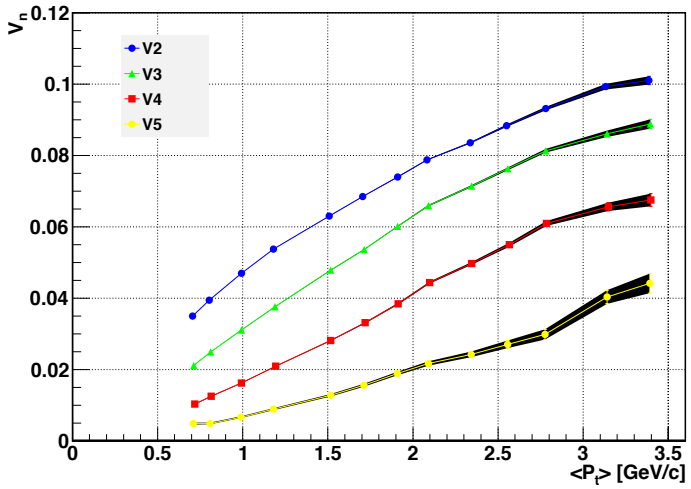

Figure 5.17: Extracted flow parameters (v_n, n=2,3,4,5) as a function of p_T.

Figure 5.17 shows $v_{\rm n}$ as a function of mean $p_{\rm T}$ in 0-10% central events. During the fit procedure, which is explained in the previous chapter, there was no η gap restriction. One can perform a direct Fourier decomposition [173] from the correlation function by projecting over the full $\Delta\eta$ range. We construct the correlation function in the $0-5\%$ centrality range in order to make a more direct comparison to the published data which used η gap method the event plane method [174].

5.4.3.2 Non-flow Parameters

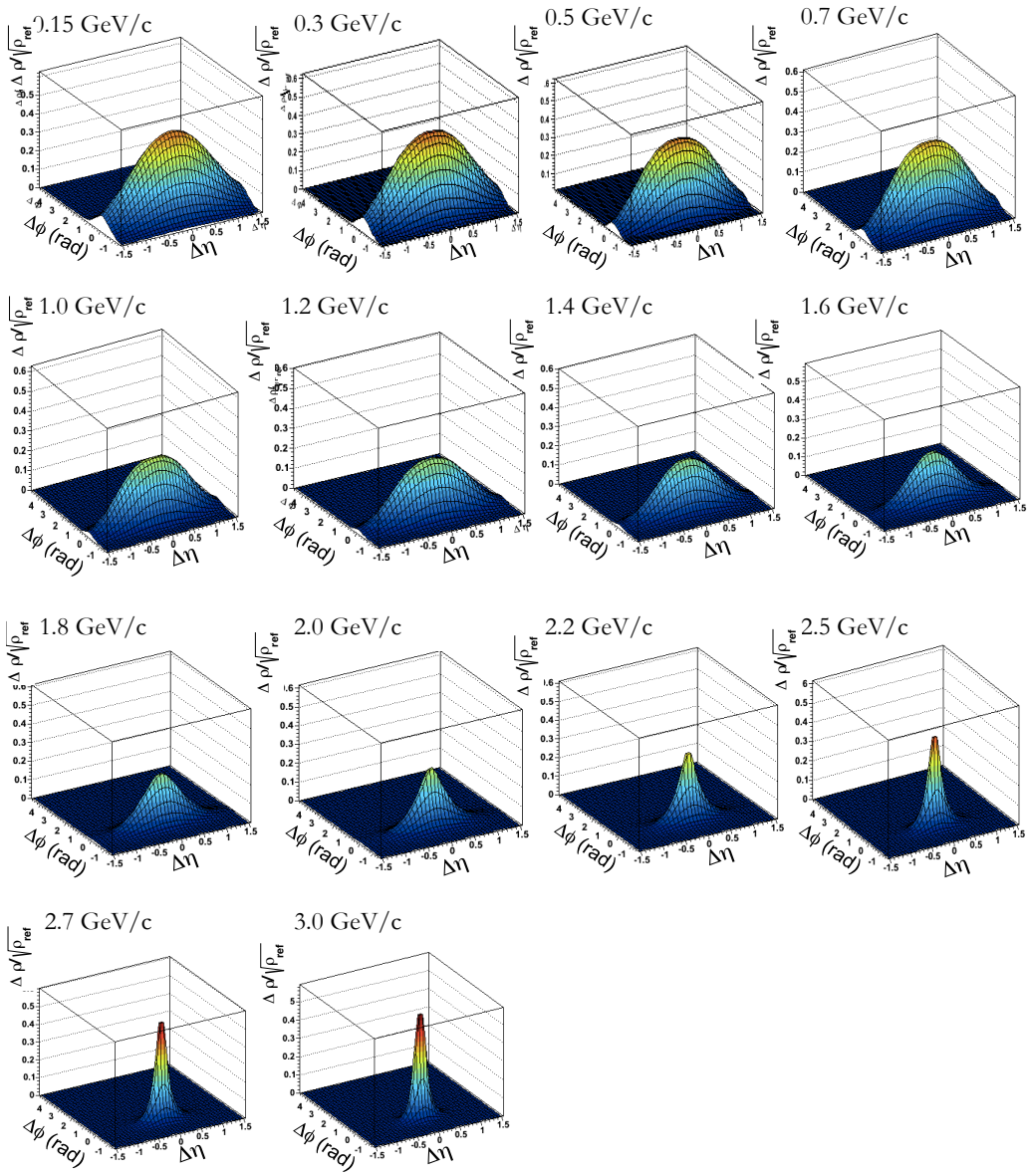

Figure 5.18: The momentum evolution of 2D Gaussian.

Figure 5.18 shows the modeled 2D gaussian evolution after v_n subtraction as a function of p_{T}. At low p_{T}, a broad ridge is observed, the so-called "soft ridge." At high p_{T}, the broad ridge becomes a sharp jet peak. We find a smooth evolution of di-hadron correlation structures as a function of p_{T} from a soft ridge to a jet peak.

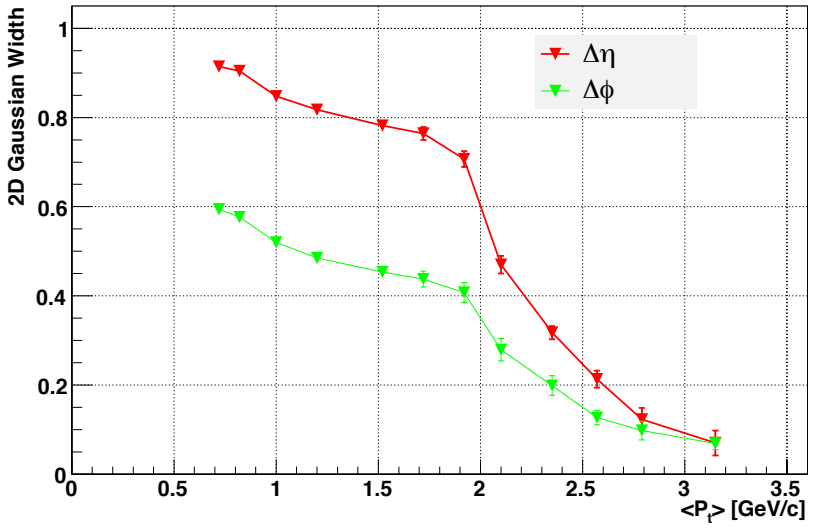

Figure 5.19: The Gaussian width evolution .

The extracted Gaussian width parameters from the fit are plotted as a function of mean p_{T} in Figure 5.19. At high p_{T}, the $\Delta\phi$ and $\Delta\eta$ widths agree well in magnitude, which can be interpreted as the the jet becoming symmetric at high p_{T}, while there is a clear separation or asymmetry at low p_{T}.

The reliability of our results is associated with the uncertainty of the measurement. Thus we performed an extensive statistical and systematic error estimation (chapter 6) before comparing to other independent measurements or theory predictions in chapter 7.

Chapter 6

Error Analysis

6.1 Statistical uncertainty estimation

In general, a statistical error gives the amount by which an observation differs from its expected value. By increasing the sample size one can reduce the statistical error. In this thesis work we used the full data set with 14 million events to minimize the statistical error.

6.1.1 Statistical error from the fit

As discussed in previous chapters, a multi component fit function was used to extract the parameters. The statistical error of the parameter was obtained from the uncertainty of the fit parameter. Because of ample statistics fluctuations were minimized and the quality of the fit is reflected by the χ^2/DOF. In the p_{T} windows study, we

start to lose statistics and can observe the gradual increase of statistical fluctuations.

6.2 Systematic uncertainty estimation

AOD 086 (14 M Events)						
Binning	Integral Method			Window method		
Event selection	Primary Vertex Selection			Primary Vertex Selection		
	10cm	7cm	5cm	10cm	7cm	5cm
TPC only tracks	✔	✔	✔	✔	✔	✔
Hybrid tracks	✔	✔	✔	✔	✔	✔
Two track efficiency	✔	✔	✔	✔	✔	✔
Charge dependency	✔	✔	✔	✔	✔	✔
Fitting procedure	✔	✔	✔	✔	✔	✔
	AOD 081 AMPT					
Wing correction	Generated level ✔			Reconstructed level ✔		

Figure 6.1: Overview of systematics checks performed

In this section we will discuss the systematic checks we performed (see table. 6.1) to check the stability of the results. By changing certain cuts in the analysis, one can determine the changes in the extracted parameters. One can also study additional effects by turning off correction procedures. First, we look at the systematics due to event selection and track selection. Afterwards, systematic errors from the correction

procedure will be discussed. Finally, systematics from the procedure itself will be addressed.

6.2.1 Systematics due to event selection

The event selection is based on a primary vertex cut and the centrality. In the p_T analysis we only studied the central events. Therefore event selection was only affected by the primary vertex selection. Hence, we compared the structures of the correlation functions for different primary vertex cuts as a systematic check. Primary vertices had to be within $\pm 5, \pm 7, \pm 10$ cm respectively. In order to see the dependence of the primary vertex selection, the correlation functions from two different primary vertex cuts were compared by subtraction. For TPC-only tracks, we observe a spike after the subtraction of 7cm from 10cm structure (Fig. 6.2, right frame).

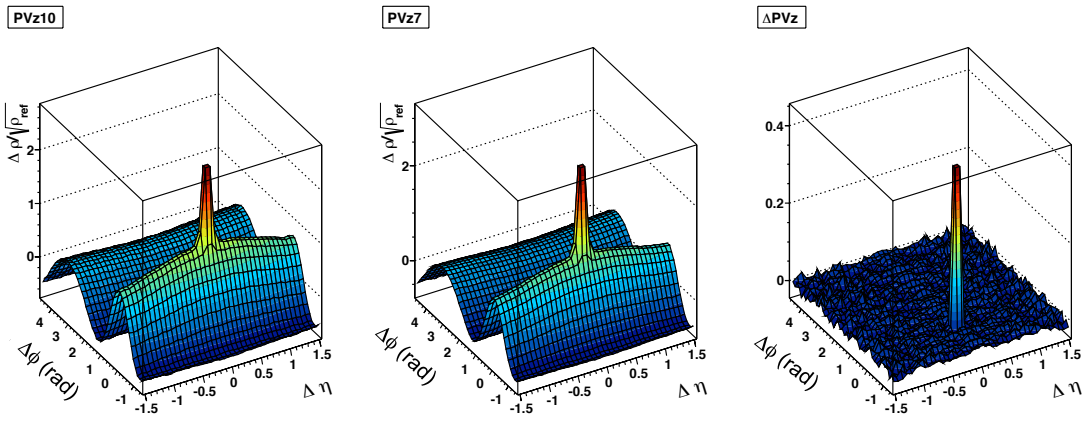

Figure 6.2: Left : the correlation structure with 10 cm , (middle) with 7 cm primary vertices and (right) the difference between the structure with $p_T > 0.15$ GeV/c.

There is no spike when the correlation functions are compared for the 5 cm and 7 cm cuts (Figure 6.3 and 6.4). The primary vertex selection is further extended

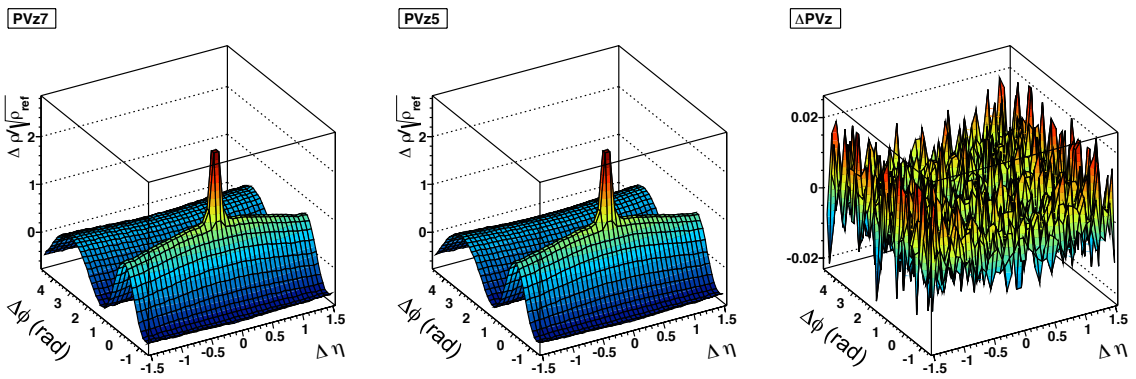

Figure 6.3: Comparison of the primary vertex selection 7 cm (left) and 5 cm (middle) using TPC only tracks and the residual is shown in the right
higher-order

by using Hybrid tracks (e.g., Figure 6.4). Hybrid tracks are reconstructed with TPC and ITS signals together, and regarded as the most reliable set of tracks. In all cases, there appears to be little difference when the vertex cuts are changed. The narrow peak in the TPC Only signal is stronger than the hybrid signal. This is due to the primary particles interaction with the detector material and hybrid tracks are cleaner compared to TPC Only tracks, as it requires both TPC Only and ITS hits for track reconstruction. However, this does not affect our analysis as we remove the quantum correlations. It should be noted the spike is modeled with a exponent in the fits, and we do not extract any physics information from these correlation functions. Figure 6.5 shows the extracted parameters with the different primary vertex selections. Good agreement is observed within different primary vertex selections and, there is no accountable dependency of correlation function on the primary vertex selection.

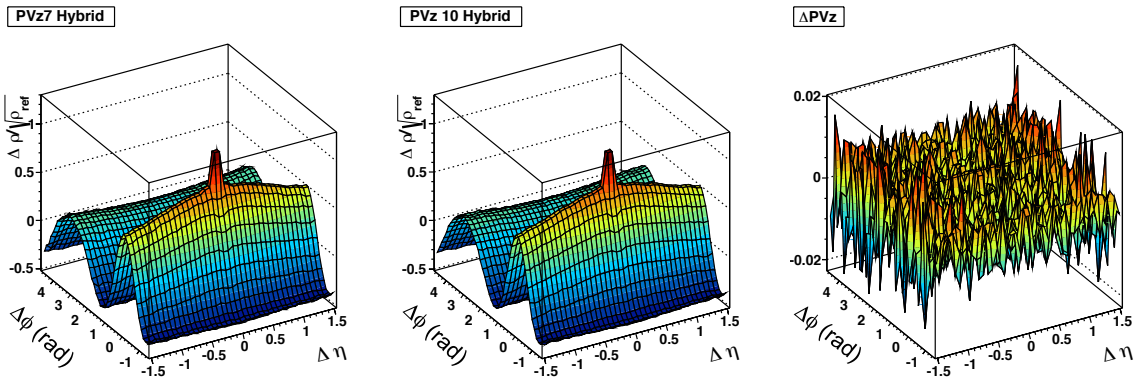

Figure 6.4: Comparison of the primary vertex selection 7 cm (left) and 10cm (middle) using Hybrid tracks and the residual is shown in the right

6.2.1.1 Statistical significance test

One should note that events with 7cm and 5cm primary vertex are a subset of the 10cm primary vertex event pool. A technique advocated by Barlow [177] is useful for checking the statistical significance of systematic variations when a subset of data is compared to the full sample. If A is a subset of B, then the statistical uncertainty of the difference $A - B$ is $\sqrt{{\sigma_A}^2 - {\sigma_B}^2}$. If the difference is less than the statistical limit there is no true systematic due to the selection of the subset.

Figure 6.6 upper raw shows the above mentioned statistical significant test for $v_2$and v_3. Data sets with 7cm and 5cm primary vertex cut are compared as per above. It is observed that the statistical uncertainties are higher than the difference between the observables from the subsets. This means there is no systematic deviation beyond what is expected from statistics. In the bottom row of the fig. 6.6 we observe that the trend for v_2 and v_3 also applies to v_4 and v_5. Thus, we report the maximum

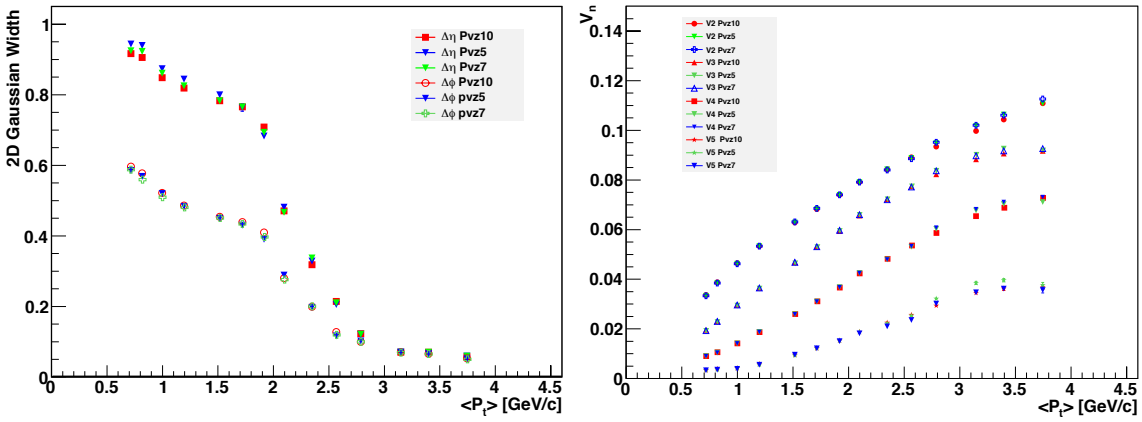

Figure 6.5: Systematic study of Fourier harmonics and Gaussian parameters with different primary vertex selections.

discrepancy of the parameters between two primary vertex selections as a systematic.

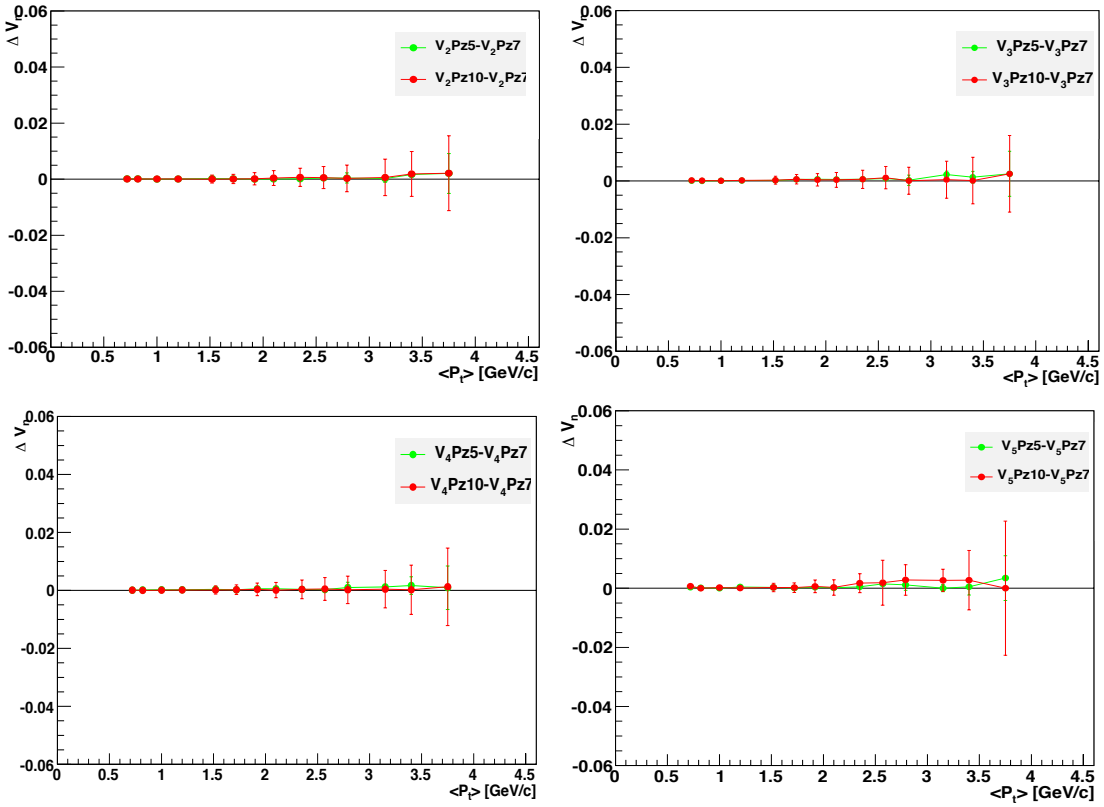

Figure 6.6: Barlow test for v_n due to primary vertex selection.

6.2.2 Systematics due to track selection

The effect of the track selection is evaluated by comparing results obtained using different track cuts, i.e. Hybrid tracks versus TPC-only tracks.

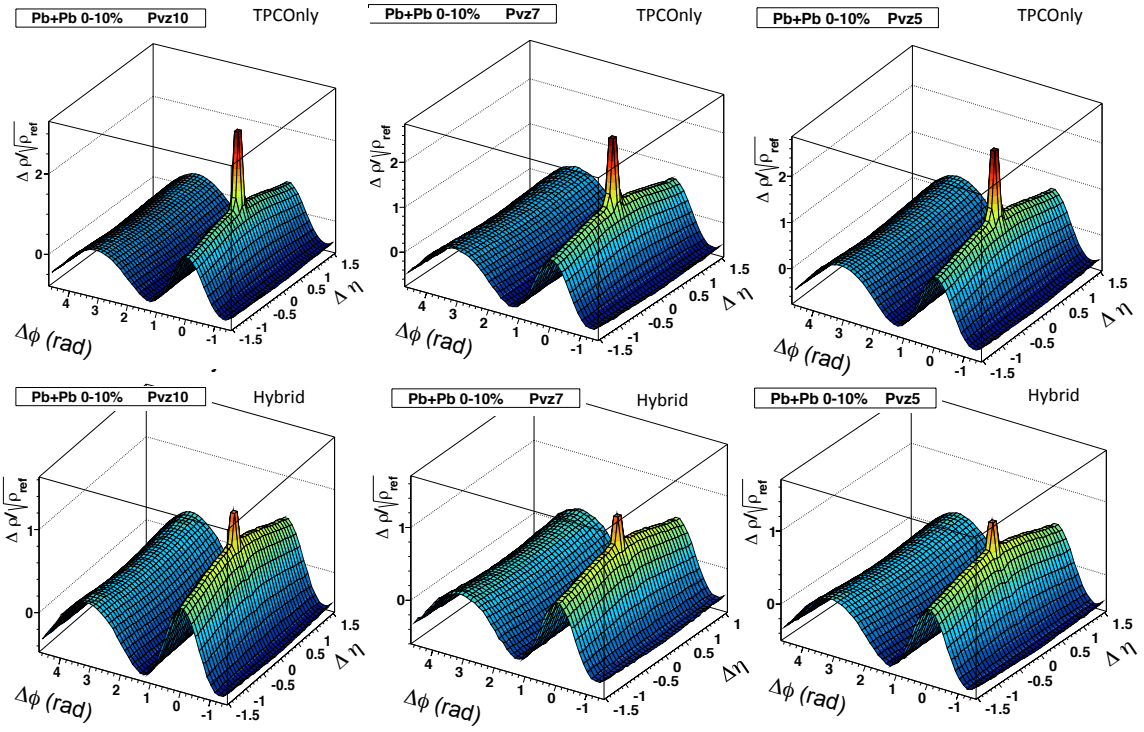

Figure 6.7: The comparison of the track selection TPC Only (upper row) and Hybrid(lower row) first the lowest bin ($p_T > 0.15$ GeV/c) three different primary vertex selections are shown .

Figure 6.7 shows the comparison of TPC-only tracks (upper row) and Hybrid tracks (lower row), where the columns are for different primary vertex cuts. The HBT peak for the TPC-only tracks is much larger than for hybrid tracks, otherwise, both structures looks quite similar. The structures can now be compared as a function of p_{T}(see Figures 6.8 - 6.13).

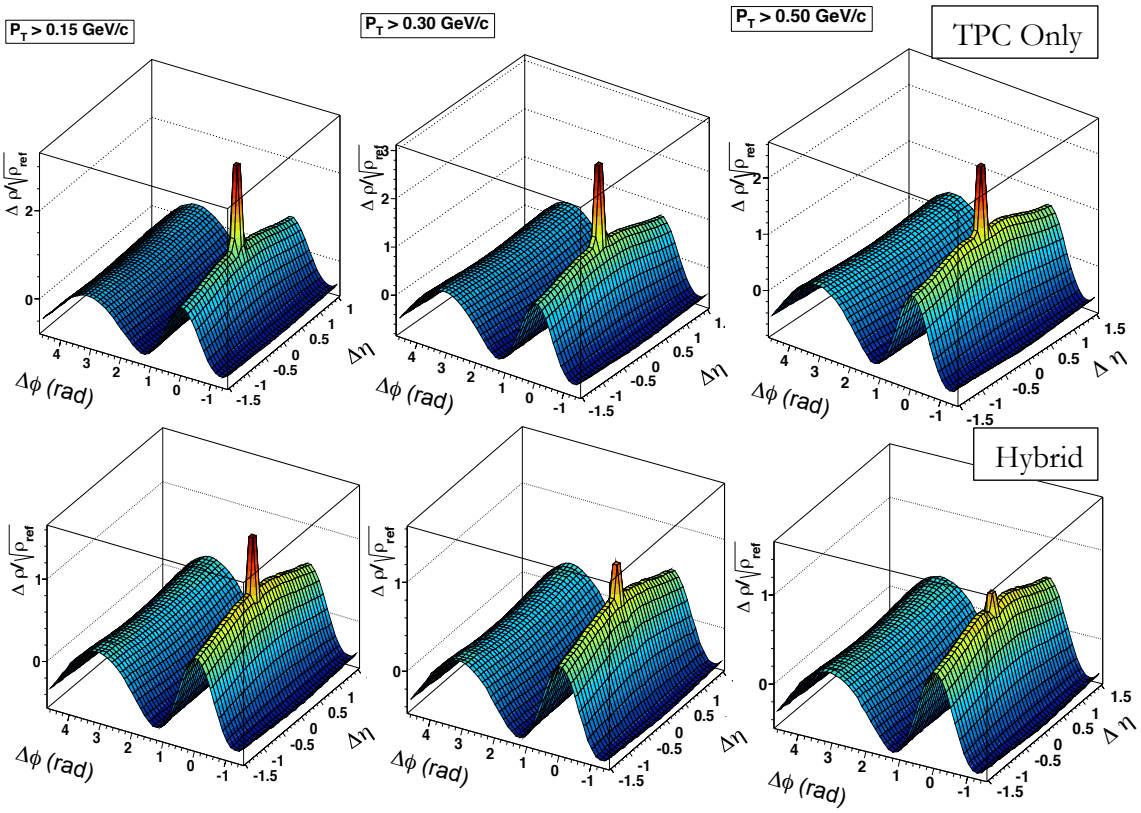

Figure 6.8: The comparison of the track selection TPC Only (upper row) and Hybrid(lower row) tracks as a function of p_{T} for first three bins

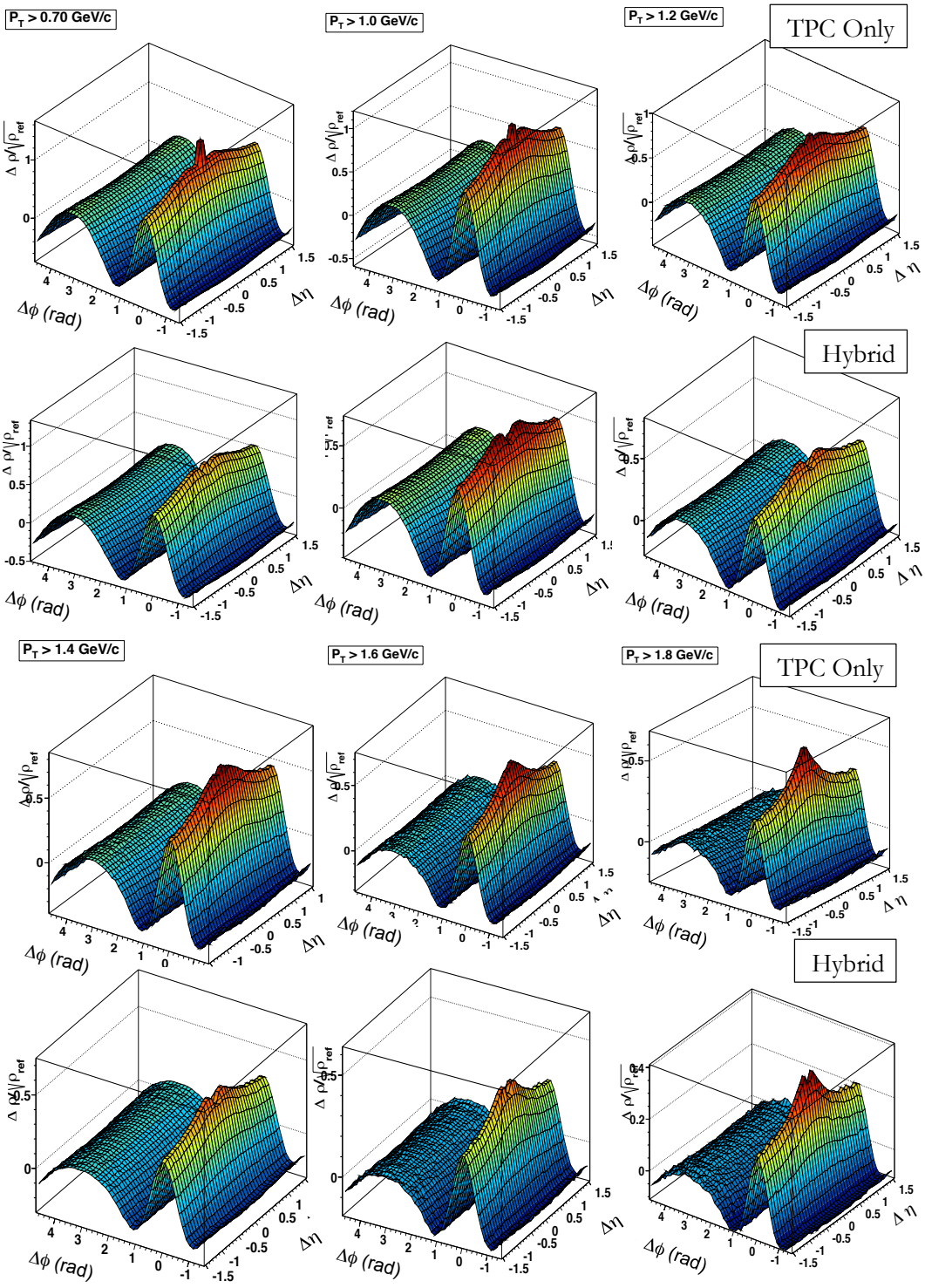

Figure 6.9: The comparison of the track selection TPC Only (upper row) and Hybrid(lower row) tracks as a function of p_{T} momentum bins up to 1.8 GeV/c are shown

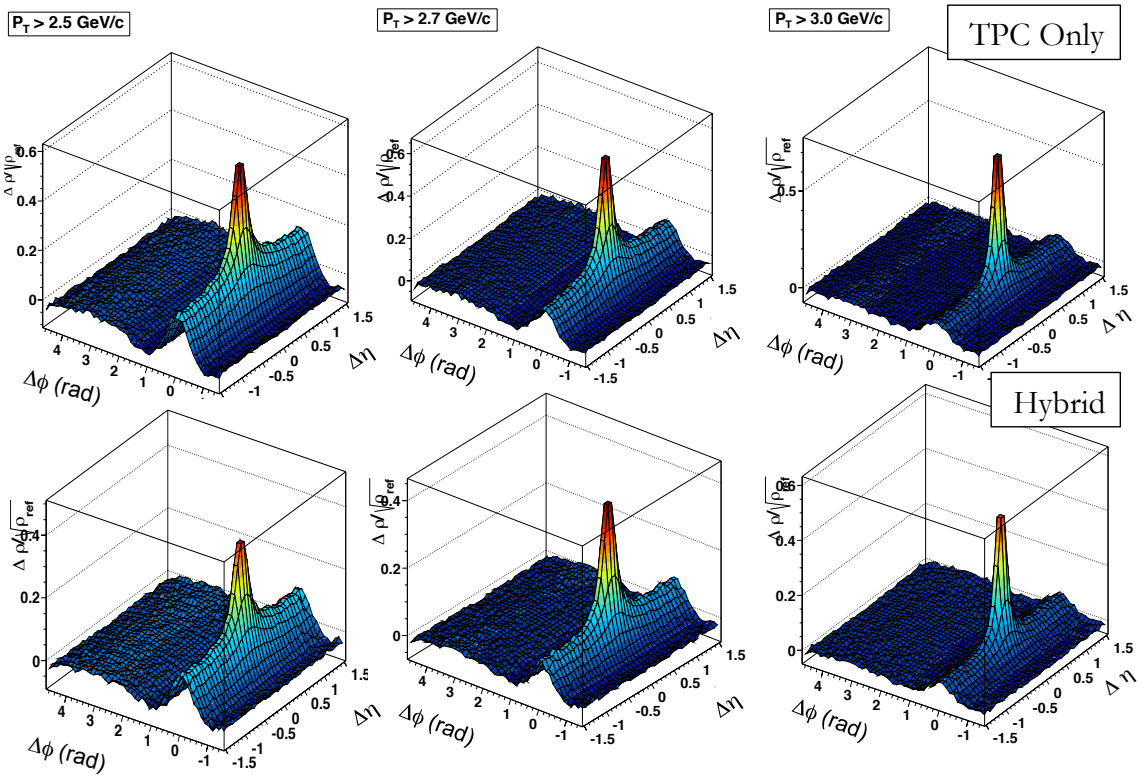

Figure 6.10: TPC Only vs. Hybrid tracks at high $p_T > 2.5$ GeV/c

In order to gain a better understanding, the correlation structures of different track selections are projected over the full $\Delta\phi$ range. Here, a lower momentum threshold of $p_{\mathrm{T}} > 0.15 GeV/c$ is used. As shown by the left frame of Figure 6.11, both the projections look quite similar, except near $\Delta\eta$=0. However, the small angle peak ($\Delta\eta \approx 0$) is higher in TPC-only tracks, so this difference is expected. The green line in the right frame shows the difference whereas the ratio is shown as the black line. It is observed that the difference is close to zero and the ratio has a slight oscillation near unity, presumably from HBT contributions.

Figure 6.12 shows the p_{T} evolution of Fourier coefficients for different track selections. Good agreement is observed between the different track selections.

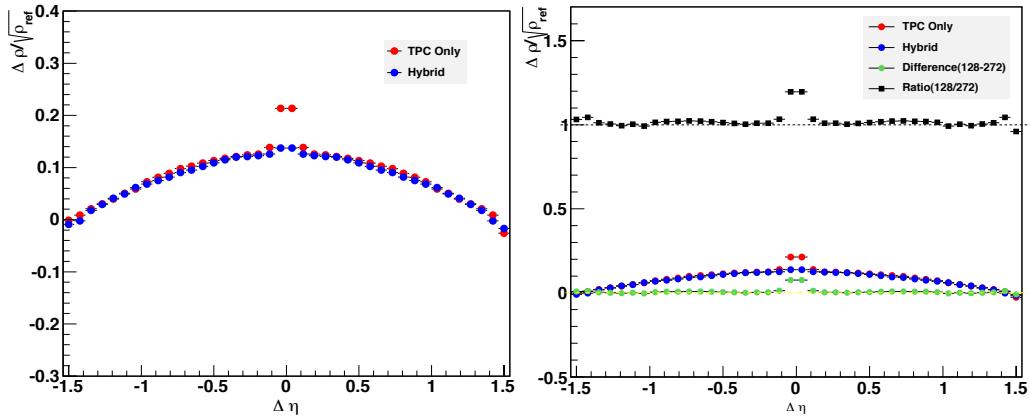

Figure 6.11: The comparison of projected correlation functions over $\Delta\eta$ using TPC-only and Hybrid tracks

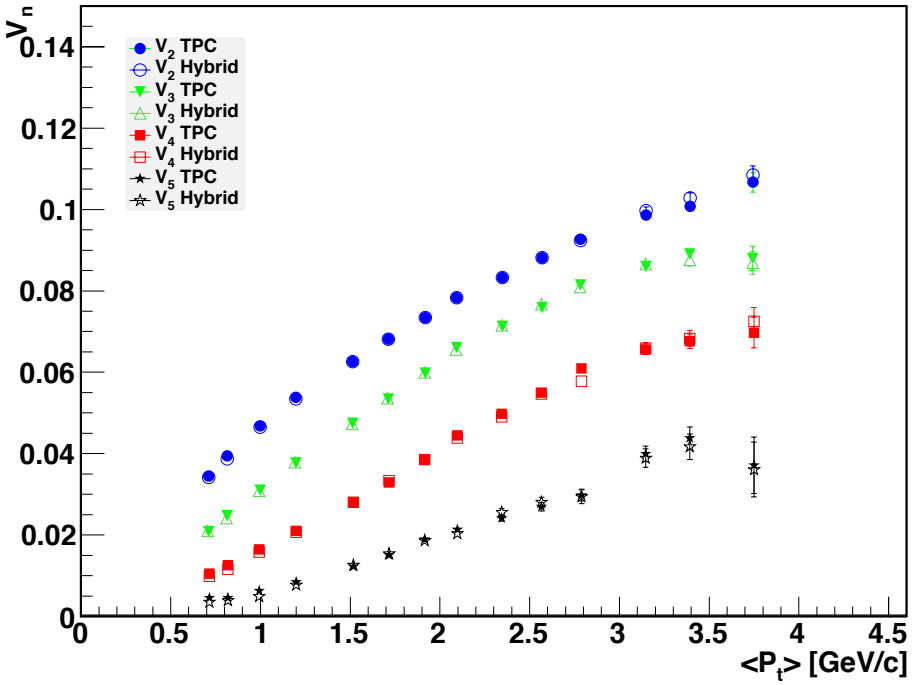

Figure 6.12: Comparison of flow coefficients as a function of transverse momentum (TPC-only vs. Hybrid tracks)

6.2.3 Systematics due to corrections

6.2.3.1 Wing effects

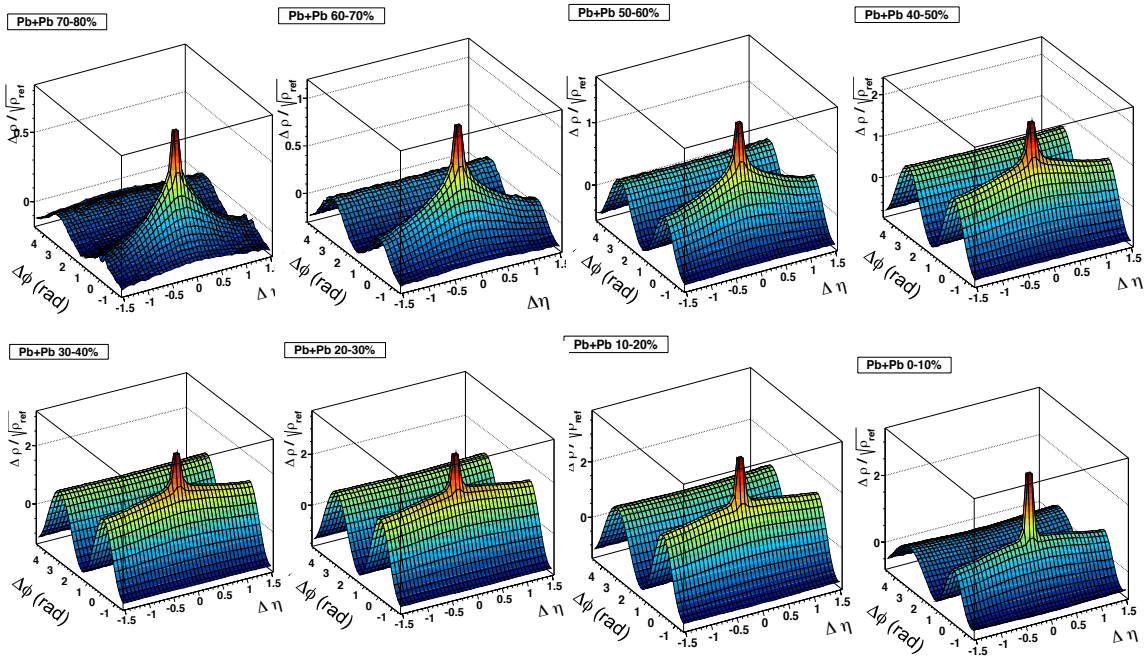

Figure 6.13: The centrality evolution of untriggered di-hadron correlations for min bias events.

Figure 6.13 shows the centrality evolution of the 2D correlation functions. In Figure 6.14, we show an away-side projection to investigate the centrality dependence of the wings. It appears the wings are stronger in central events. As explained in chapter 4, the correction for this acceptance effect in η is carried out via a subtraction of a polynomial function. Here we calculate the difference of the parameters with and without that subtraction and report it as the systematic uncertainty due to the $\Delta\eta$ acceptance. The estimates are summarized in the table 6.1 and this correction has the highest contribution(5%) to the systematics in low momentum range.

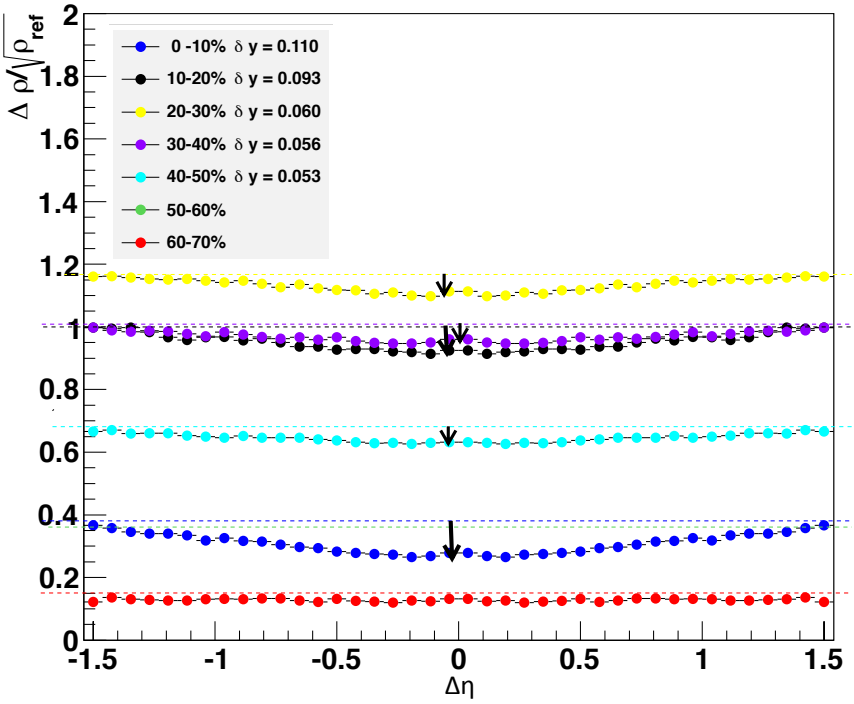

Figure 6.14: The centrality evolution of projected away-side wing on $\Delta\eta$.

6.2.3.2 Two-track efficiency

The effect of the two-track efficiency correction was also studied by comparing the fit parameters with and without the correction. An additional test is carried out by varying the standard cut values ($\Delta\eta < 0.02$ and $\Delta\varphi < 0.02$) . The cuts were first doubled and then halved. Both Gaussian parameters and flow parameters showed less sensitivity (<1%) to the two-track efficiency correction.

6.2.4 Systematics due to procedure

6.2.4.1 Momentum binning

The momentum evolution of the untriggered di-hadron correlations first studied by increasing the lower threshold of the momentum cut for both particles. The extracted parameters are then plotted as a function of the mean p_{T} for a given cut. We refer to this as the *integral* method . The second procedure was to study the parameters as a function of momentum windows, which the following cuts $x < p_T < x + 0.5$, $x < p_T < x + 0.25$ GeV/c. The widths of the windows are 0.5 and 0.25 GeV/c. We refer to this as the *window* method.

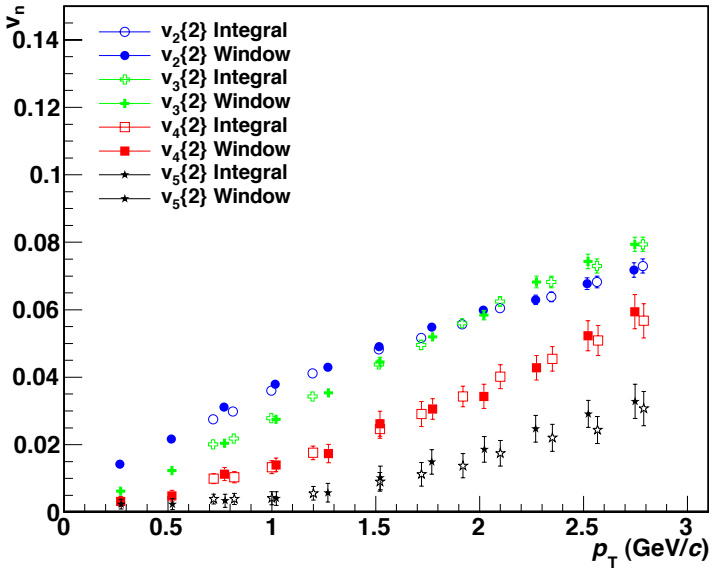

Figure 6.15: The comparison of extracted v_n between Integral method and windows methods.

Figure 6.15 shows the comparison of the two methods; integrals vs windows (with 0.25 GeV/c width windows). One can see they give consistent results.

6.2.4.2 Charge dependence of the correlation function

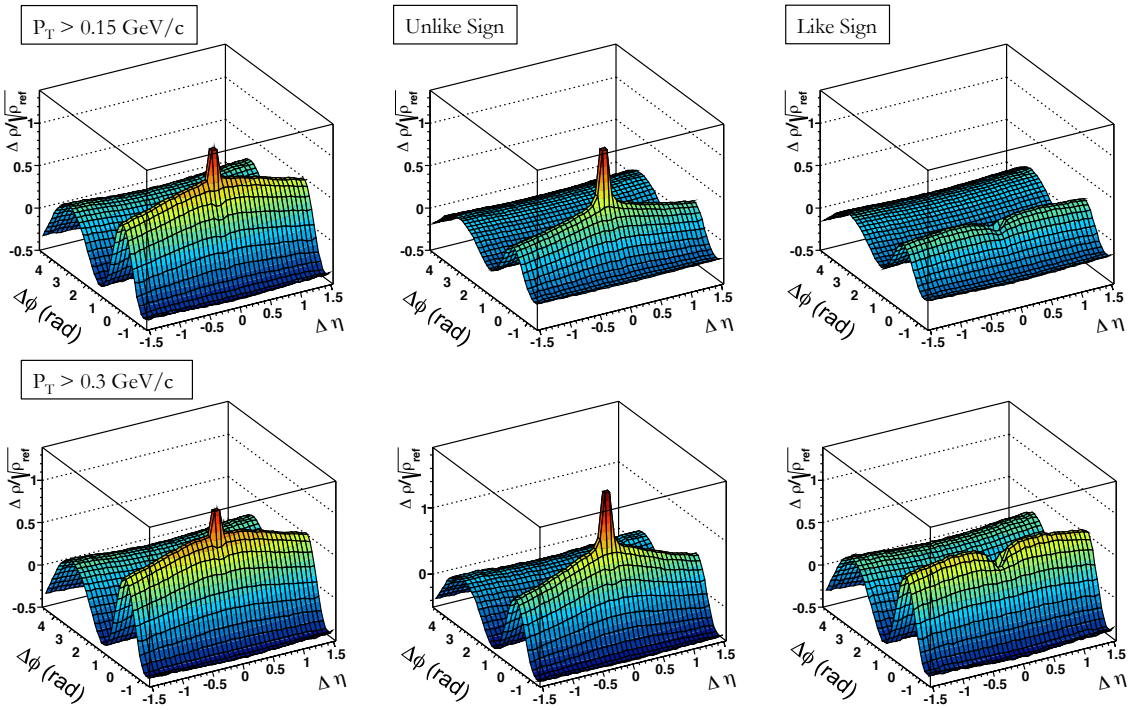

Figure 6.16: Charge dependence of di-hadron correlation function

In order to study the charge dependence of the extracted parameters, correlations functions were constructed separately from like-sign (++ or $--$) and unlike-sign ($+-$ or $-+$) pairs. Figure 6.16 (upper row) shows the charge independent (left) ,unlike-sign (middle) and like-sign(right) structures of correlation function for $p_{\mathrm{T}} > 0.15 GeV/c$. One can see that the spike appears only in the unlike sign correlation function (middle structure in both rows). This indicates that we see more e^+, e^- conversions than HBT correlations. Figures 6.17-6.19 show the momentum evolution of the charge dependence of the correlation function.

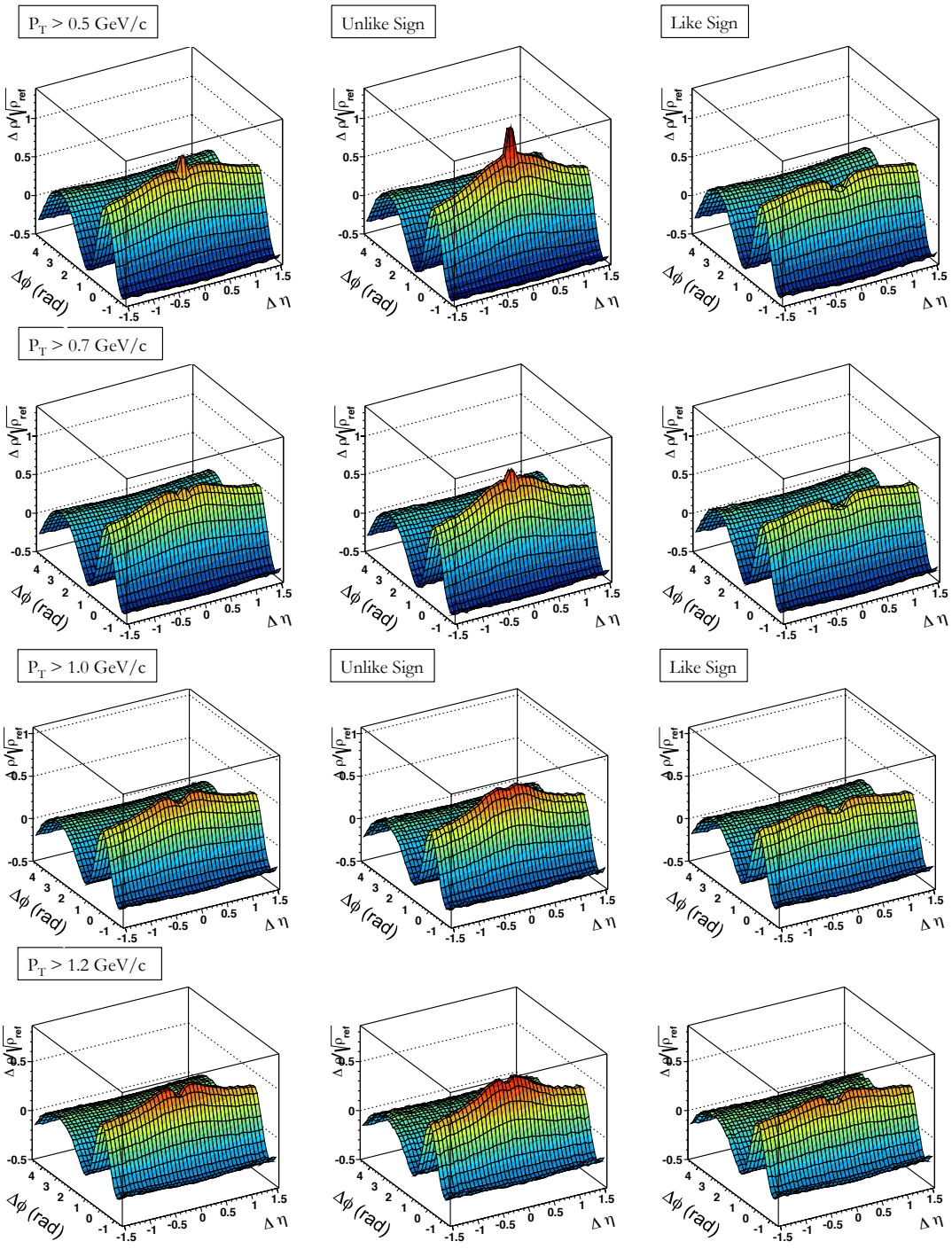

Figure 6.17: Comparison of the correlation functions(left) charge independent (middle)Unlike sign Like sign(right) as a function of p_T.

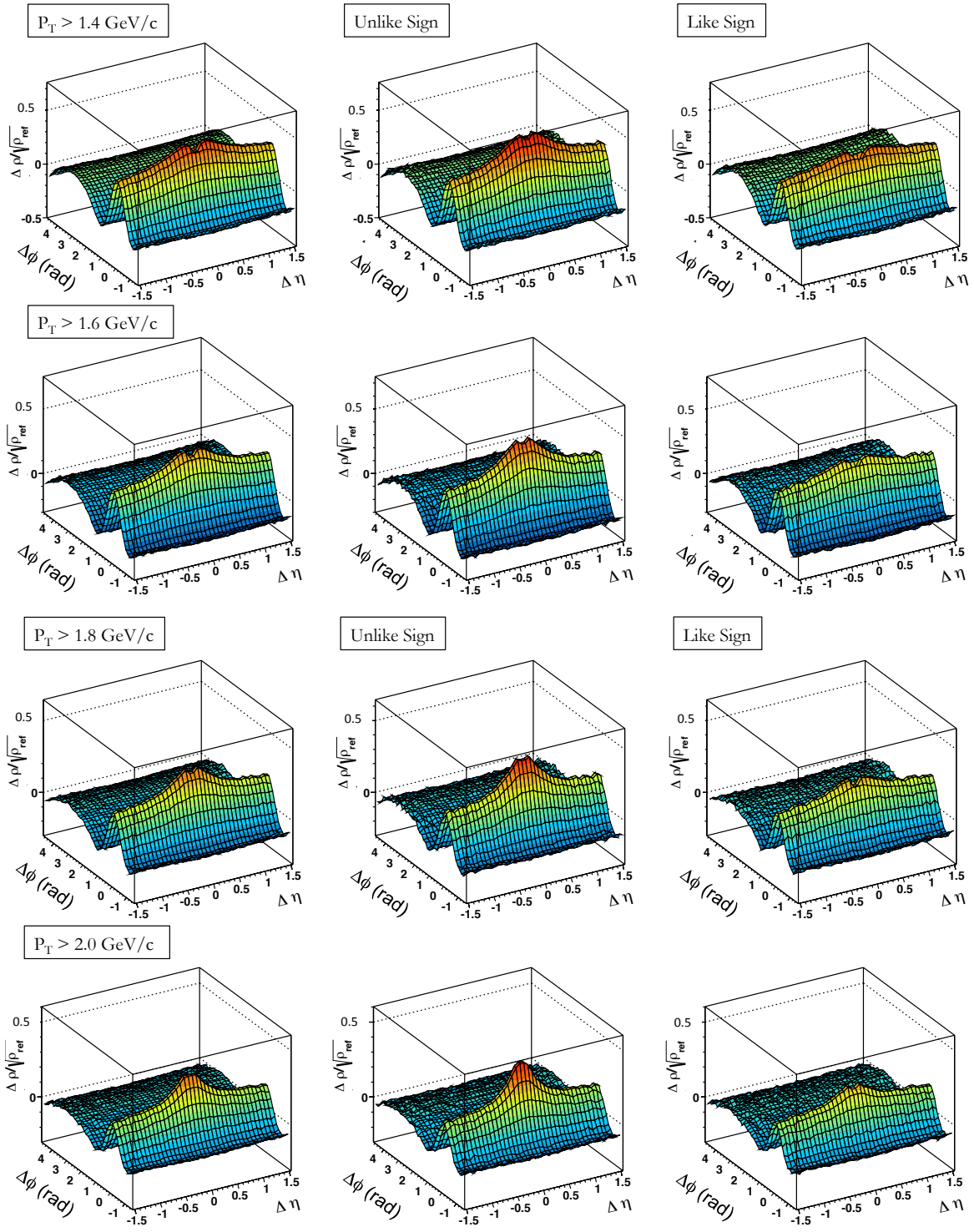

Figure 6.18: Charge dependence of the correlation in the mid p_{T} range.

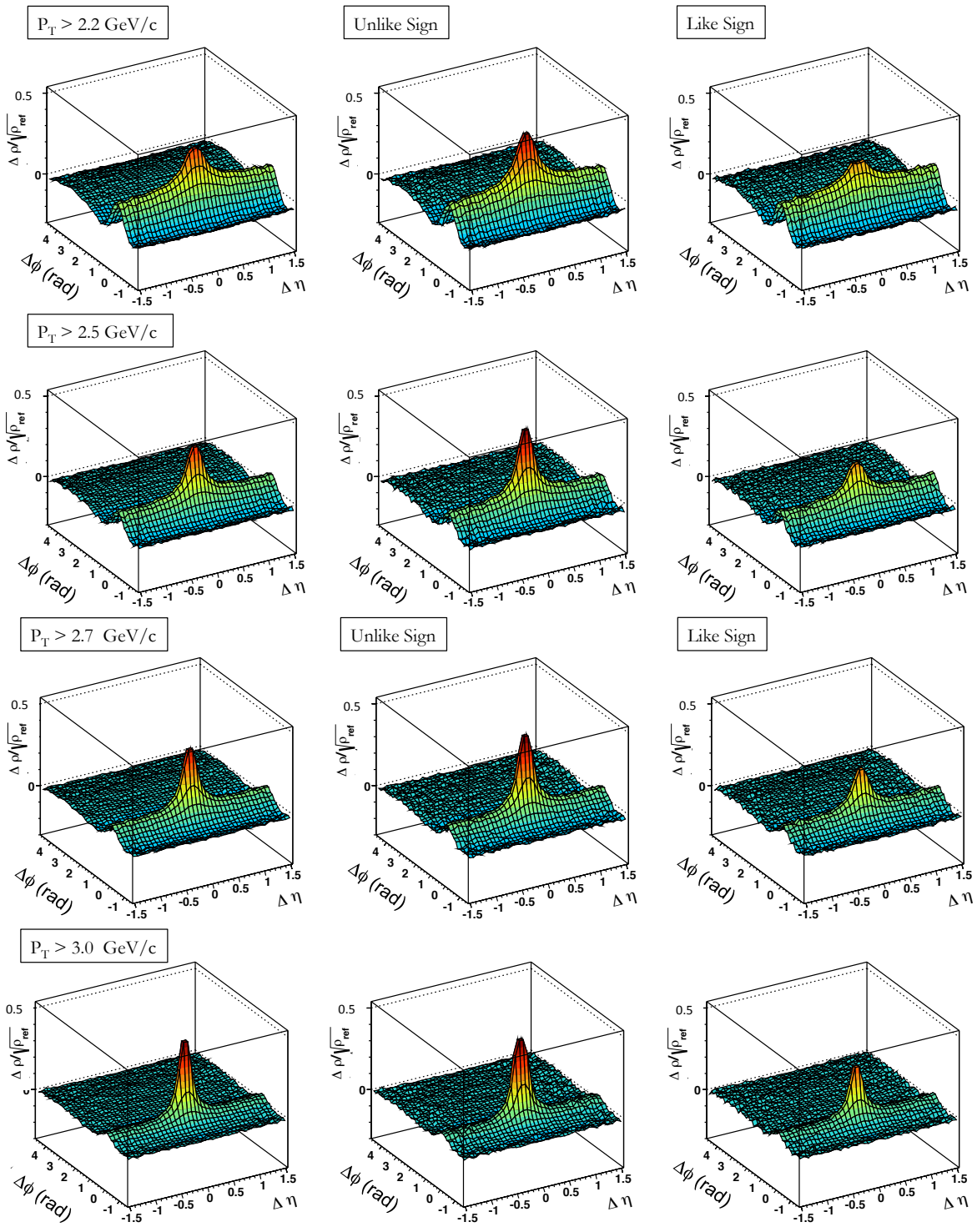

Figure 6.19: Charge dependence of the correlation in the high range $p_{\mathrm{T}} > 2.2$ GeV/c

.

In figure 6.20 we compare the charge dependent Fourier coefficients as a function of mean p_{T}. There is no evidence for any charge dependence of the Fourier harmonics.

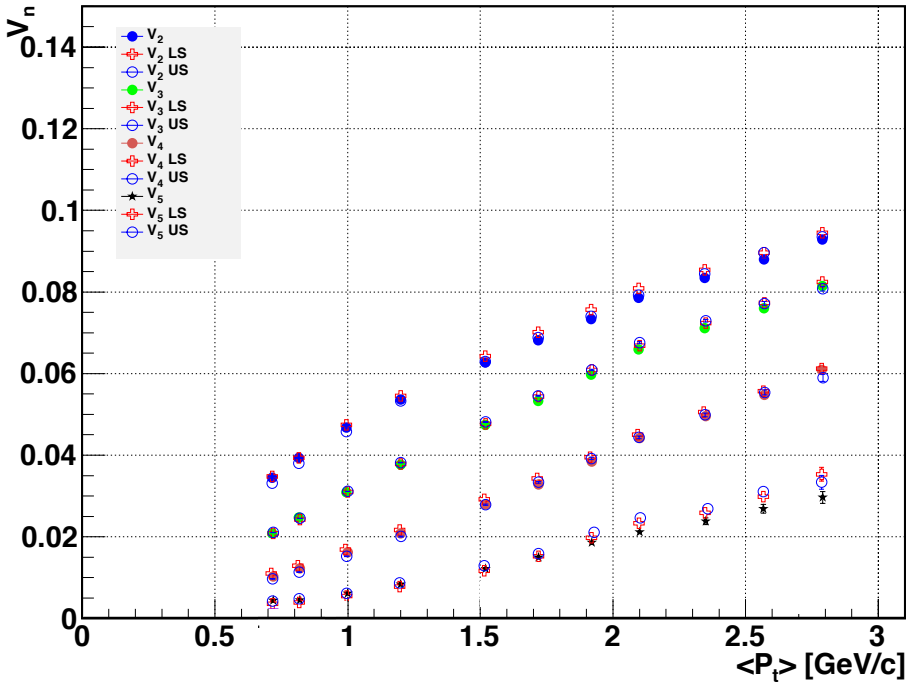

Figure 6.20: Charge dependence of the Fourier harmonics (v_n, n= 2,3,4,5) as a function of p_T.

6.2.5 Summary of systematics uncertainties

Table 6.1 shows a summary of the systematic uncertainties. The track selection relates to the differences observed between hybrid and TPC only tracks. Event selection refers to the differences observed for different vertex cuts. The acceptance correction (wing) causes the largest uncertainty.

Parameter	$v_{\mathrm{n}}(n = 1, 2, 3, 4, 5)$	2d Gaus. $\Delta\eta$ width	2d Gaus. $\Delta\phi$ width
Track selection	$< 1\%$	$< 1\%$	$< 1\%$
Event selection	$< 1\%$	$< 1\%$	$< 1\%$
Wing correction	$< 1\%$	$< 5\%$	$< 5\%$
Two-track efficiency	$< 1\%$	$< 1\%$	$< 1\%$
Momentum binning	$< 1\%$	$< 1\%$	$< 1\%$
Fitting procedure	$< 1\%$	$< 1\%$	$< 1\%$
Charge dependence	$< 1\%$	$< 1\%$	$< 1\%$

Table 6.1: Summary of systematic uncertainties

6.3 Final results

6.3.0.1 Addition of higher harmonics (v_6)

In order to study the initial energy density fluctuations, the order of the highest v_n increased and up to v_6. At high p_{T} one can see the v_6 signal (see fig. 6.21 green line in the bottom). The v_6 parameters are extracted for the first time from the ALICE experiment via di-hadron correlations.

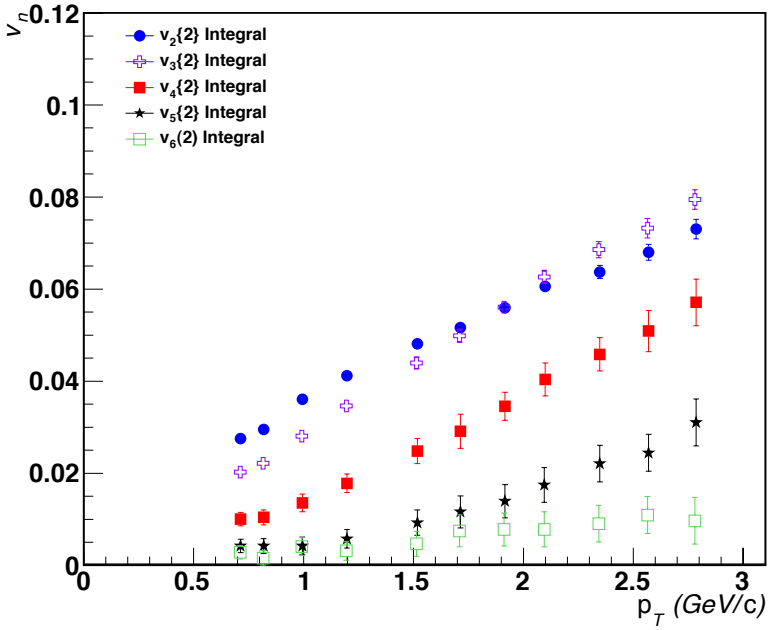

Figure 6.21: Fourier harmonics v_n, (n = 2,3,4,5,6) for 0-5% centrality class using the lower threshold method.

The systematics we discussed so far can be treated as independent errors. Hence one can add them in quadrature to get the final systematic uncertainty. Figure 6.22 shows the extracted Fourier harmonics with full systematics. Here the statistical and systematic errors are combined and presented as a single value. The values are also

compared with the most recent independent measurement[175]. The closed symbols are from this analysis and yield smaller error bars. As v_6 is extracted for the first time, one needs an independent measurement to confirm the result.

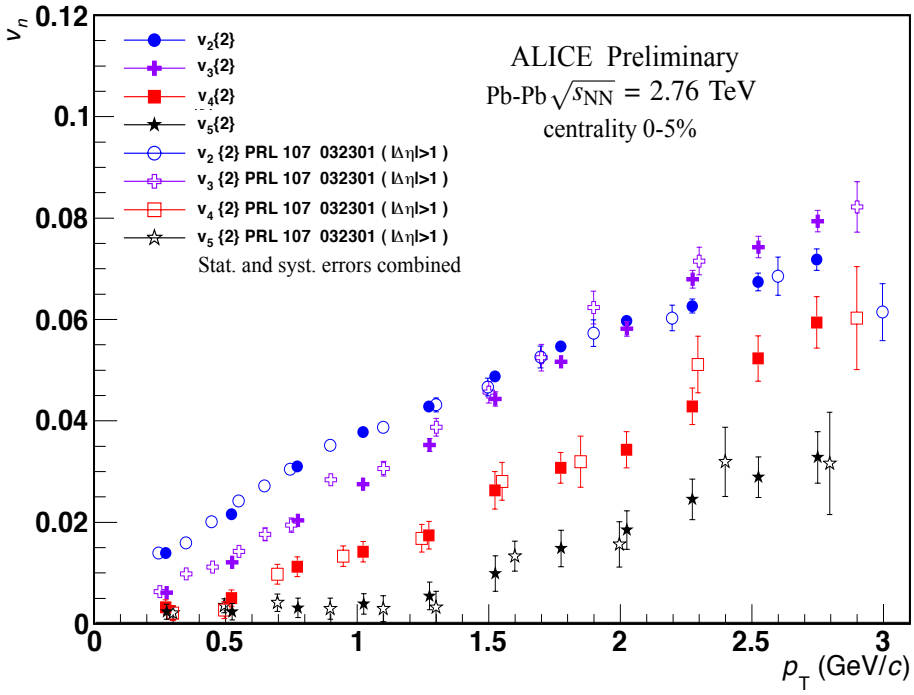

Figure 6.22: Fourier harmonics with final error bars.

Figure 6.23 shows the transverse momentum evolution of Gaussian widths. The systematics are shown as gray box whereas statistical errors are shown as error bars. One can observe that the largest systematic uncertainty is in the lower momentum bins. This is mainly due to the acceptance correction because the wing correction causes the nearside Gaussian to become larger. Consequently, the Gaussian parameters have larger uncertainty. At hight p_{T} the effect of the correction is minimal and the uncertainty is dominated by statistics.

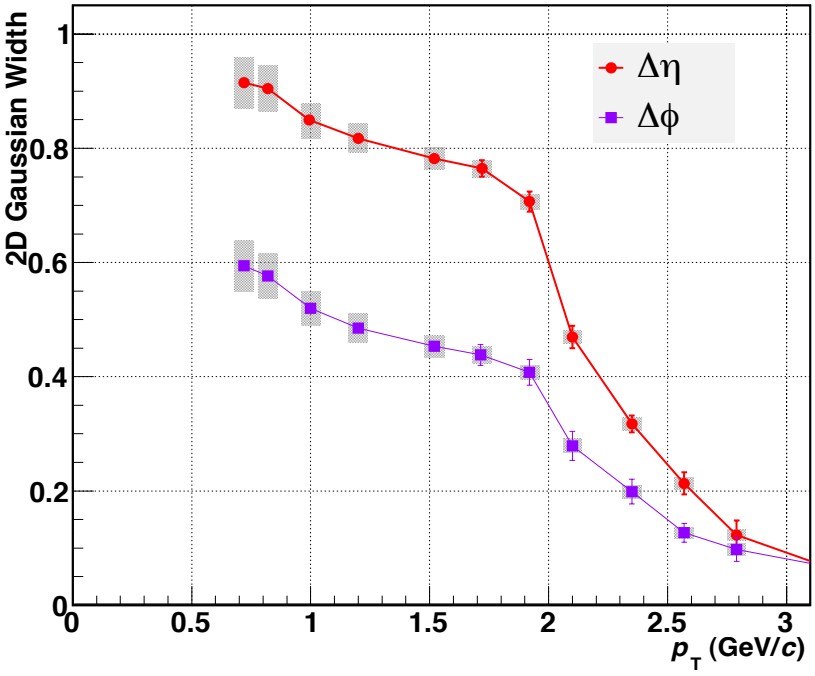

Figure 6.23: Gaussian parameters as a function of p_{T}.

Chapter 7

Discussion and Conclusions

In this chapter, we try to relate the parameters extracted from the momentum dependence of di-hadron correlations to the model predictions. First we discuss the advantage of the technique applied for our v_n measurements. Then we compare our measurements to the most recent measurements. Afterwards, we compare our v_n values to the recent theoretical predictions and deduce the importance of the flow measurements to understand the QGP medium properties. At the end, we address the Gaussian parameters and jet modification at lower momentum. A possible link to calculating energy transport coefficient in the QGP based on the data at high $\langle p_T \rangle$ will also be discussed.

7.1 Higher-order Fourier coefficients

Comparison to other techniques

Here we compare the v_n $(n = 2, 3, 4)$ values from this analysis for two different techniques. Obtaining flow parameters with the least presence of non-flow was one of the goals of this thesis work. Figure 7.1 shows the comparison between the 2D fit method(this thesis work open symbols) and the $\Delta\eta$ gap method (closed symbols). In the $\Delta\eta$ gap method [174] the removal of non-flow (or jet) is carried out by excluding the jet region in the fit function (typically $|\Delta\eta| < 1$).

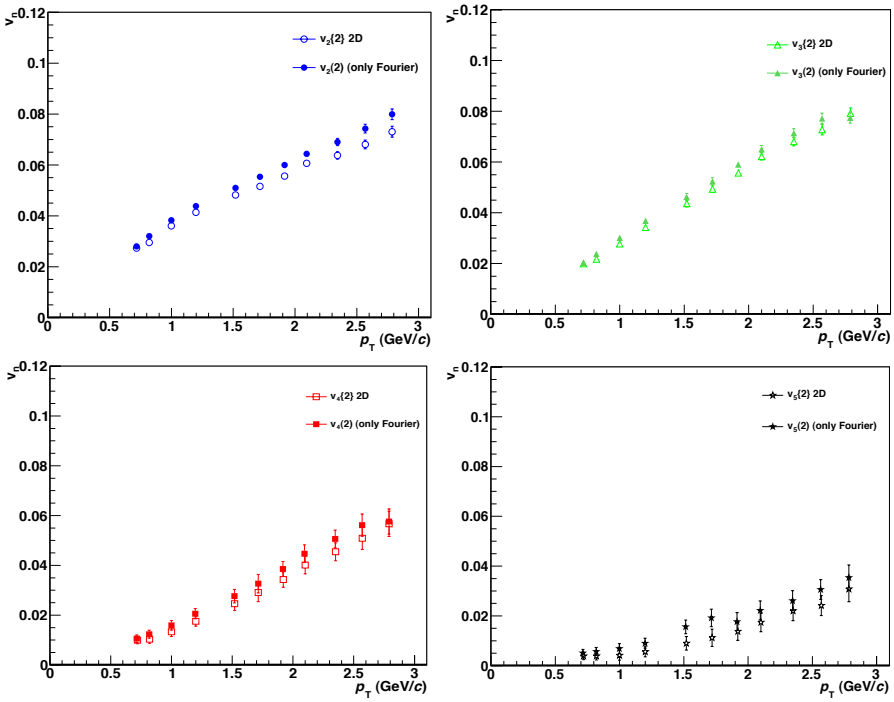

Figure 7.1: Comparison of extracted v_n coefficients from 2D fit method and $\Delta\eta$ gap method.

By excluding the jet region one can minimize the non-flow contribution in flow

measurements. However it does not fully remove the non-flow. In our method, we do not exclude any region, which means the complete $\Delta\eta$ is used in the estimation of the flow coefficients and non-flow contributions. This way, we remove the non-flow rather than minimizing it. One can see that the v_n values from the $\Delta\eta$ gap method are slightly higher than the 2D fit method, which can be attributed to the presence of non-flow in the measurement compared to our method. The above figure indicates the strength of the applied analysis technique.

7.1.1 Theory comparison

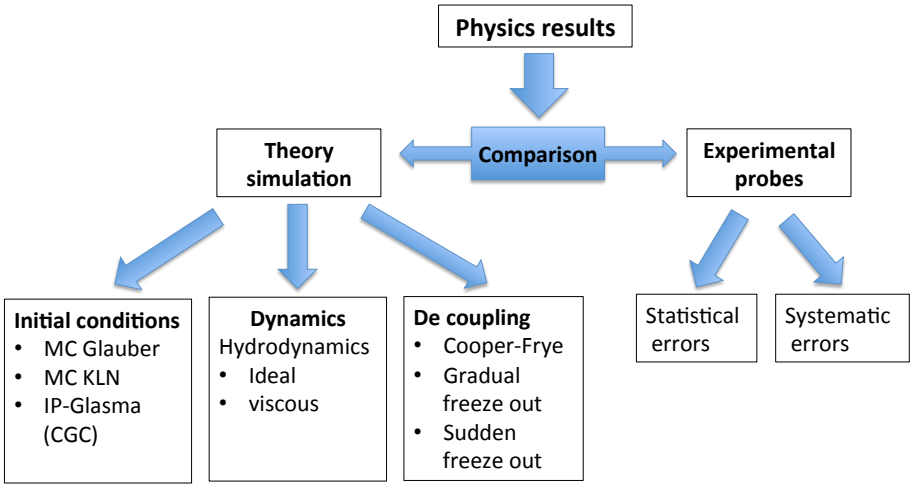

Figure 7.2: Sources of uncertainties which influence the physics results

7.1.1.1 Comparison to recent theoretical developments

In order to understand the physics behind the deconfined state of matter, we attempt to explain the experimental results using model predictions. Obtaining new physics

depends on the accuracy of both theoretical and experimental calculations. Thus, proper estimation of statistical and systematic uncertainty becomes an essential task. In this thesis work we discussed the uncertainty associated with the experimental results in the chapter 6. We have performed an extensive systematics study while minimizing the statistical uncertainties. Theoretical modeling of a relativistic heavy-ion collision is quite complicated and challenging. The process of modeling can be done in three steps. First, the initial conditions of the colliding nuclei have to be modeled. Second, the dynamical evolution of the Quark Gluon Plasma has to be implemented. The third stage is the reproduction of the particle spectra. Each stage has different challenges and limitations. The modeling of the initial nucleon distribution of colliding nucleus is theoretically represented by several models. The Monte Carlo (MC)Glauber model is one such model.

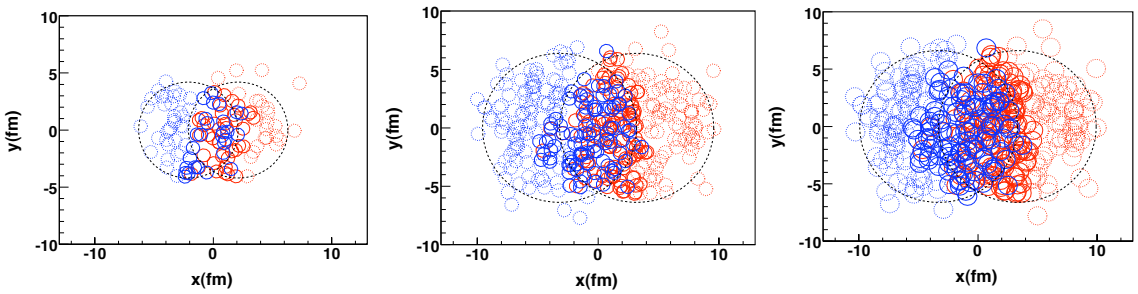

Figure 7.3: Typical events for Cu+Cu (left panel), Au+Au (middle panel), and Pb-Pb (right panel) collisions, the first two were performed at RHIC energies and the latter at the LHC.Wounded nucleons (participants) are indicated as solid circles, while spectators are dotted circles

In heavy-ion collisions, initial geometric quantities such as the shape of the collision region and the impact parameter cannot be directly determined experimentally.

However, it is possible to find the relationship between the number of observed particles and number of spectator neutrons to the centrality of the collision. Based on the centrality of a collision, the initial geometry can be estimated. In MC Glauber calculations, a uniform matter density is assumed. The quantity is typically described by a Fermi distribution in the radial direction and uniform over solid angle. In the Monte-Carlo-based models, individual nucleons are randomly distributed on event-by-event basis. The calculation of collision properties are done via averaging over larger number of events (collisions). Figure 7.3 shows the Glauber-Monte-Carlo simulation of the nucleon distribution for different systems. The dynamical evolution of the QGP phase is modeled via hydrodynamics. Hydrodynamic modeling includes initial conditions, an equation of state (EOS) and a decoupling prescription. At the kinematic freeze out temperature, the Cooper-Frye formalism has been carried out for converting the fluid cells of the system into particles [124].

Studies show that the higher-order Fourier harmonic scaling relation $\frac{v_n^{1/n}}{v_2^{1/2}}$, for RHIC data which is discussed in [100] indicates a discrepancy from the ideal hydrodynamical behavior[106]. Further studies [107-110] indicate that the observed discrepancy can be due to the degree of thermalization in the QGP, elliptic flow and eccentricity fluctuations in the initial geometry, or viscous effects of the QGP medium. The Glauber initial condition model was improved very recently by coupling to color charge fluctuations using a modified Color Glass Condensate (CGC) picture to incorporate quantum fluctuations. In order to investigate the underlying physics, we compared the Fourier harmonics to these models which pair CGC initial conditions with viscous hydrodynamical flow [104,105].

First, an Impact Parameter dependent saturation model (IP-Sat) [112,113] which incorporates high energy nuclear and nucleon wave functions has been combined with classical Yang-Mills description of glasma fields (CGC)[114-117] in heavy-ion collisions. This improved model is called IP-Glasma model [104,105,118] and has the following properties.

- Nucleon positions are distributed using Woods-Saxon potential
- Impact parameter dependent $Q_s^2(x, \mathbf{b}_\perp)$ is obtained for each nucleon by fitting IP-Sat model to deep inelastic scattering (DIS)data from the HERA experiment
- The color charge squared per unit area, $g^2\mu^2(x, \mathbf{b}_\perp)$, is proportional to $Q_s^2(x, \mathbf{b}_\perp)$
- The characteristic correlation length is $1/Q_s$ thus allowing a finer granularity than the nucleon scale

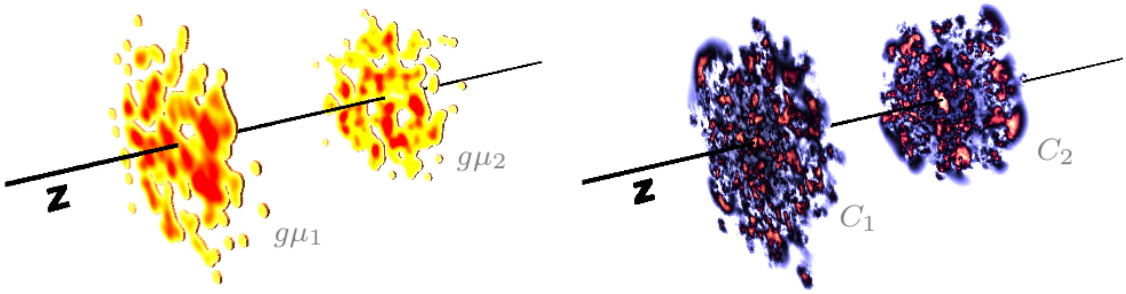

Figure 7.4: The color charge densities of incoming nuclei $g\mu$ for Au + Au collisions at 200 GeV. Higher densities are shown in red [118].The degree of correlation and fluctuation in the gluon fields of the lead ions at $\sqrt{S_{NN}} = 2.76\,TeV$.

The degree of correlation and fluctuation of the gluon fields in the incoming nuclei are shown in Figure 7.4. After the initial classical Yang-Mills (CYM) description ($\approx 0.2\, fm/c$) of this boost invariant configuration of gluon fields, the system is evolved using relativistic viscous hydrodynamics as prescribed in MUSIC [119-122] which is a 2 + 1D relativistic viscous hydrodynamical simulation. The hydrodynamical evolution requires the construction of the energy momentum tensor:

$$T^{\mu\nu}_{fluid} = (\epsilon + P)u^{\mu}u^{\nu} - Pg^{\mu\nu} + \Pi^{\mu\nu} \tag{7.1}$$

where ϵ is the energy density in the fluids rest frame, u^{μ} is the flow velocity, P is the local pressure using the equation of state at all transverse positions and $\Pi^{\mu\nu}$ is the shear viscosity. The equation of state used is derived using a hadron resonance gas model and fits to lattice QCD results [123] solved for ϵ and u^{μ} considering energy momentum conservation ($\partial_{\mu}T^{\mu\nu} = 0$). Partial chemical equilibrium temperature at which the different species of particles are formed is set to below 150 MeV with the kinematic freeze out temperature at which the particles stop interacting set to 120 MeV.

Comparison to RHIC measurements

Figure 7.5 shows how the initial energy anisotropy propagates with and without viscous effects. As shown in figure 7.5, after 6 fm/c, ideal hydrodynamical evolution preserves much of the initial energy anisotropy compared to the viscous hydro evolution of the medium. A non-zero viscosity to entropy density ratio ($\eta/s \neq 0$)

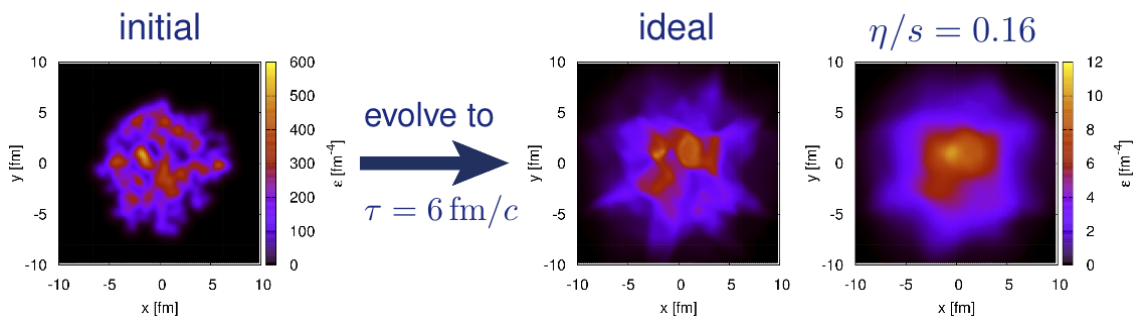

Figure 7.5: The evolution of initial energy density with and without viscous effects using the MUSIC simulation [111].

dampens the flow strength (the anisotropy transformation between the initial geometrical anisotropy and final state momentum space anisotropy) that is measured experimentally.

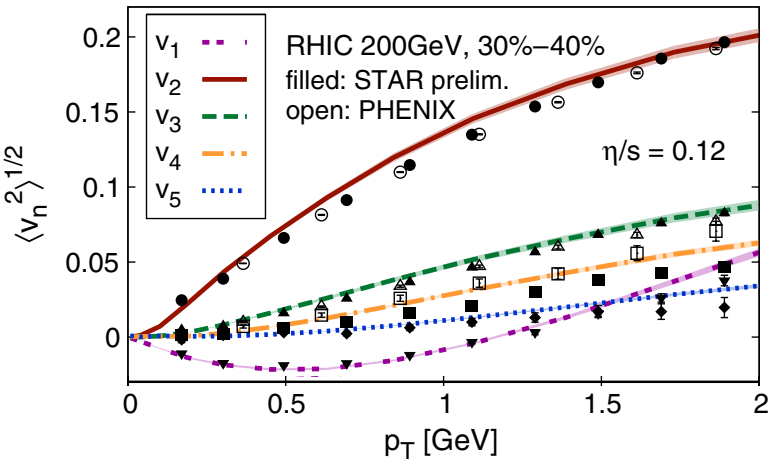

Figure 7.6: Comparison of $v_n(p_T)$ for $\eta/s = 0.12$ for RHIC data , Experimental data by the PHENIX (open symbols) and STAR (preliminary, filled symbols) Collaborations. Bands indicate statistical errors.

The data are well described by the theoretical results with a η/s value of 0.12, which is larger than the predicted quantum limit of $(1/4\pi = 0.08)$ [125,126] and

within the predicted range 0.08 - 0.24 [127].

Comparison to our LHC measurements

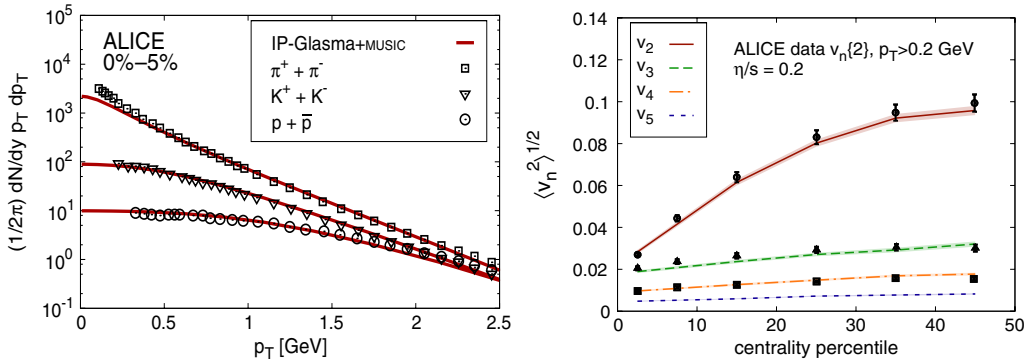

Figure 7.7: (Leftpanel) Identified particle p_T spectra including all resonances up to 2 GeV compared to experimental ALICE data; (Right panel) Root-mean-square anisotropic flow coefficients v_n $(n = 2, 3, 4, 5)$ computed as a function of centrality, compared ALICE [175] (experimental points)

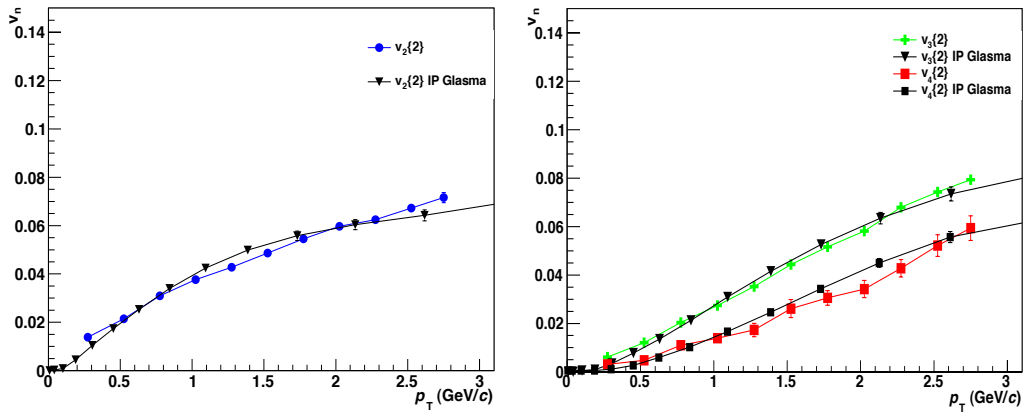

Figure 7.8: Pb-Pb 2.76 TeV data from ALICE at 0-5%(this thesis work) compared to IP-Glasma model calculations with $\eta/s = 0.2$.

The obtained p_T spectra of pions kaons and protons for 0-5% central Pb-Pb collisions at $\sqrt{S_{NN}}$= 2.76 TeV at ALICE shows good agreement with the IP-Glasma+Music

predictions with η/s= 0.2. Figure 7.7 shows that the centrality evolution also agrees well within error bars. The IP-Glasma framework has described a wide range of data in both RHIC and LHC with decent accuracy. It is the best candidate to compare our Fourier harmonics to estimate the specific shear viscosity.

We compare the transverse momentum evolution of v_n 0-5% central data to IP-Glasma model in Figure 7.8. Despite the small deviations in v_4 the model describes the data well. In particular v_3 shows excellent agreement. One can deduce that, the analysis strengthen the prediction of η/s= 0.2 since anisotropic flow measurements obtained from this method (see Figure 6.22) has better precision and the least presence of non-flow.

7.2 Implication of 2D Gaussian parameter evolution

The 2D Gaussian parameter evolution shown in Figure 6.23 can be understood primarily as medium modified jets. As shown in Figure 5.19, that the Gaussian become symmetric above $p_T \approx 2.8$ GeV/c.

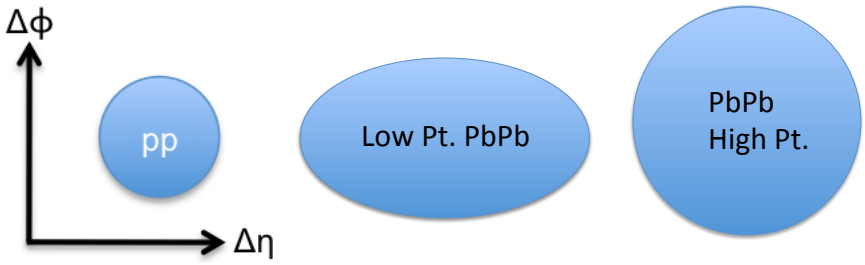

Figure 7.9: The behavior of Gaussian width modification at three different momentum ranges

The strength of di-hadron correlations in a narrow $\Delta\eta$ x $\Delta\phi$ space is expected to grow as we increase the momentum (lower p_T cut). Jets are high energetic set of partons distributed around a leading hard scattered parton, and consist of sub-leading partons closer(in the coordinate space) to the initial leading parton. The partons which are further away from leading and sub-leading particles have lower momentum compared to leading partons. Thus, as a function of the lower p_T threshold cut, the decrease in correlated pairs is less steep compared to the decrease in background pairs. This is clearly reflected in di-hadron correlation measure, as an increase of the correlation strength (see Figure 5.18). In the range Below p_T 2.8 GeV/c, the 2D Gaussian is asymmetric and more elongated in $\Delta\eta$. First we discuss the 2D Gaussian

parameters in the momentum range below 2.8 GeV/c. Recent theoretical developments [128,129], which are based on hydrodynamical evolution of the QGP, can be related to the parameter evolution. Afterwards, the broadening of the 2D Gaussian width in relation to modified jets, and the energy-loss mechanisms (characterized by the jet transport coefficient $\hat{q}$) in the QGP medium will also be discussed.

7.2.1 Implications of Gaussian widths at low momenta

The candidates for describing the $\Delta\eta$ elongation are; medium modified jets [158,159], hydrodynamical phenomena [128,129] and resonance production [165]. First, we will discuss hydrodynamical predictions which exhibit similar trends in the data.

7.2.1.1 Hydrodynamical explanations

The dynamical model we use to model the space-time evolution of QGP is a very versatile framework. As we discussed earlier, hydrodynamical modeling requires the initial conditions to propagate. The studies show that the effects due to the initial state fluctuations within a fluid cell can cause induced correlations in the final state[130]. This phenomena occurs due to natural hydrodynamical fluctuations. In this procedure, a single fluid element (also referred to as a local hot spot) is evolved by using the hydrodynamical equations in the expanding medium with flow background. The hydro fluctuations are modeled as perturbations and are implemented by adding these perturbations to the energy-momentum tensor ($T^{\mu\nu}$) and current densities (J^{μ}) [130]. The di-hadron correlation functions K($\Delta\eta$) of these stochastic terms are then

calculated by using the fluid equations of motion.

The motivation behind this study comes from studies [131]. It is found that, most of di-hadron correlations featuring azimuth angle difference ($\Delta\phi$) can be reproduced by using the hot spots. This is carried out by placing the hot spots at a particular position in the transverse plane and evolved using hydrodynamical equations. In brief, the initial microscopic space-time fluctuations are propagated in the expanding medium. Though the fluctuations are still correlated at a macroscopic scale and observed in the final state. Therefore the long range correlation in $\Delta\eta$ can be described as a result of natural hydrodynamical fluctuations of initial state, propagating through an expanding medium. In addition, one can use this procedure to deduce the η/s value.

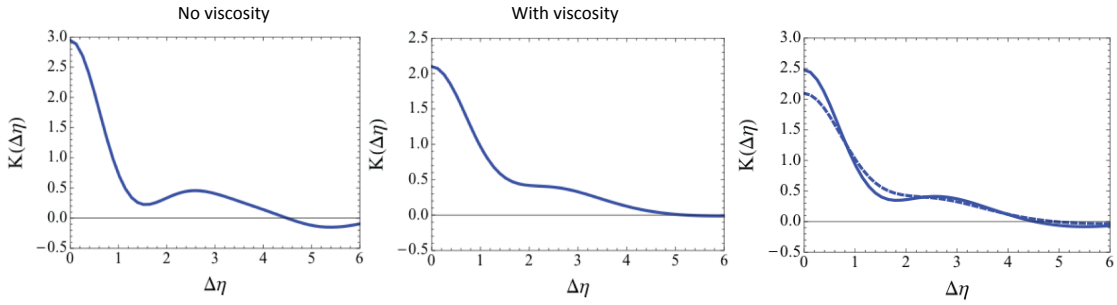

Figure 7.10: The correlation strength K($\Delta\eta$) measured in $\Delta\eta$ without (left) and with (middle) viscous effects in a hydrodynamical evolution, (right) The comparison of correlation function K($\Delta\eta$) for the two viscosity values $\eta/s = 1/4\pi$ and $3/4\pi$ using solid and dashed curve respectively.

Figure 7.10 (left and middle) shows the di-hadron correlation described in [130] without and with viscosity effects. It is observed a viscosity dependence in the $\Delta\eta$ of the di-hadron correlations. Figure 7.10 (right) shows the comparison of the correlation function K($\Delta\eta$) for the two (η/s) values $1/4\pi$ and $3/4\pi$ (the predicted range

is (η/s =0.08 - 0.24) [127]). The calculations are based on the value of kinematic freeze-out temperature (T_{fo}) of 150 MeV and the Cooper-Frye prescription [124] to obtain the final state particle spectra.

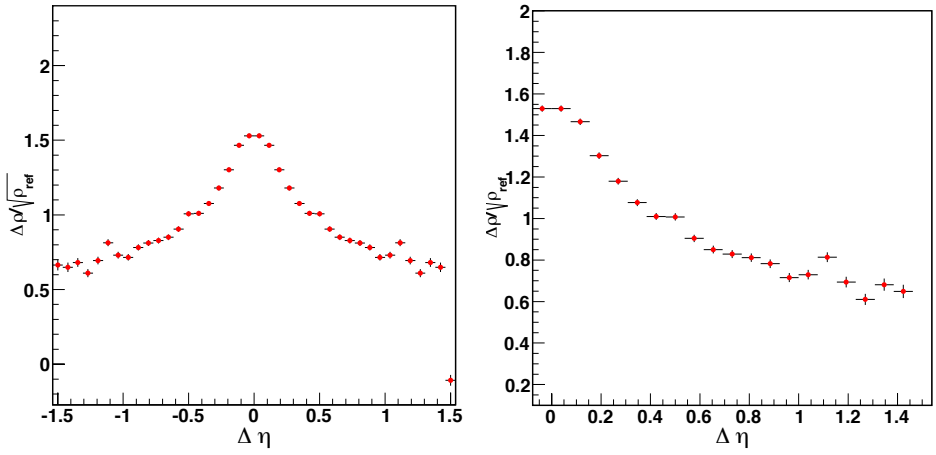

Figure 7.11: Left:The one diminutional projection of our correlation function (Pb+Pb data 0-10%) as a function of $\Delta\eta$, Right: the comparable range to the model (0- 1.5) $\Delta\eta$

In order to see the evidence of such a behavior in our correlation function, we took the one dimensional projection of the 2D correlation function on $\Delta\eta$ axis over $\Delta\phi$. Though our analysis is limited to mid pseudo rapidity range ($\Delta\eta < 1.5$), the data shows qualitative similar trend within the range. Still one needs a more analysis specific simulation to make a quantitative comparison.

7.2.1.2 Local charge conservation picture

Another hydrodynamically motivated explanation is based on the effects of local charge conservation at the de-coupling stage of the evolution [129]. In this procedure, hydrodynamical calculation has been carried out on the basis of an event by event and

Glauber model initial conditions energy distributions to construct the 2D di-hadron correlation function in $\Delta\eta-\Delta\phi$. The previous work [132 - 135], shows the importance of the formation of charges at de-coupling stage of the hydro evolution of QGP medium. Such charge-dependent particle productions exhibit strong correlations between unlike-sign pairs in $\Delta\eta$ and $\Delta\phi$. Thus, the mechanism has been proposed as the cause of $\Delta\eta$ dependence of the "ridge" correlation. In this case,the ridge is on top of the flow modulation [136]. In this local charge conservation picture, the Glauber initial conditions are evolved using a 3 + 1D viscous hydrodynamical evolution with both bulk and shear viscosity [137,138]. The initial entropy density is modeled from the code GLISSANDO [139] and the freeze-out particle emission is carried out using THERMINATOR code [140]. The local charge conservation is implemented at the de-coupling stage of the THERMINATOR code with opposite charged particles emitted in pairs from the fluid element (see Figure 7.12).

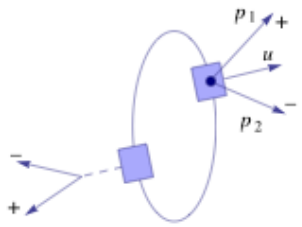

Figure 7.12: Charge conservation mechanism for resonance decay and local pair creation, where u gives the collective flow velocity of the fluid cell and p_1, p_2 are the momenta of positive and negative charged particles in the pair respectively. The charged particle pair coming out from the dotted line represents resonance decay.

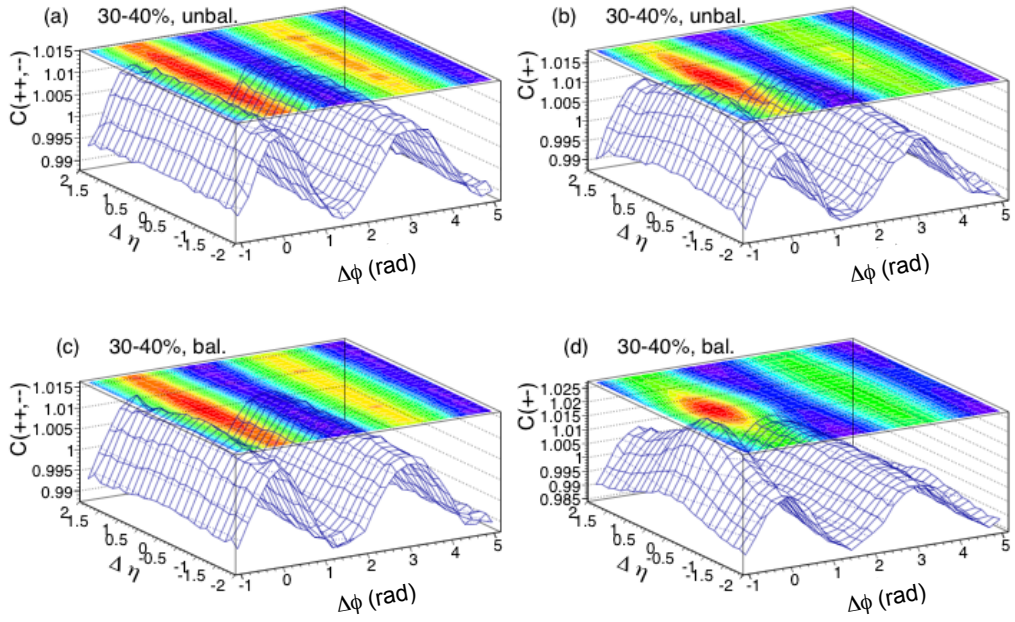

Figure 7.13: 2D correlation functions showing the local charge conservation effects. Top and bottom rows are without and with charge balancing respectively while left and right columns are for like-sign and unlike sign pairs respectively. The correlation functions are generated for 30-40% Au + Au collisions at $\sqrt{s_{NN}} = 200$ GeV and for charged particles with $0.2 < p_T < 2$ GeV/c with $T_{fo} = 150$ MeV.

As shown in Figure 7.12, the local charge conserving charged particle pair experiences the same collective flow velocity u which collimates their motion. The calculation also includes pairs from resonance decay cascades. The effect of the resonance decay cascades can be observed in Figure 7.13 top row, right panel, (unlike-sign correlation) as a weak short range correlation peak, compared to the left panel (like-sign correlation). However, when we apply the local charge conservation (bottom row), the unlike-sign correlation function is enhanced and show significant peak structure compared to the like-sign measurement. This feature is comparable to the experiment and observed similar trend [141]. As global momentum conservation needs to

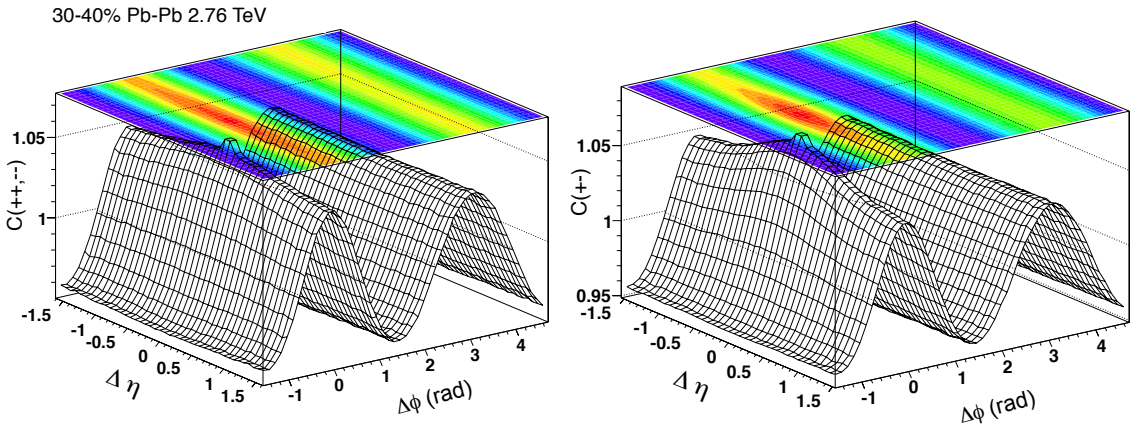

Figure 7.14: 2D correlation functions shown for this thesis work with the charge dependence. Left and right columns are for like-sign and unlike sign pairs respectively. The correlation functions are generated for 30-40% Pb-Pb collisions at $\sqrt{s_{NN}} = 2.76$ TeV and for charged particles $p_T > 0.7$ GeV/c.

be implemented in the theory, direct quantitative comparison of the theory to our data is not possible yet. In order to study this effect qualitatively, 30-40% centrality class was generated by like sign pairs and unlike pairs for Pb-Pb collisions at $\sqrt{s_{NN}} =$ 2.76 TeV. The effects from resonance decay cascades has been removed by taking out the secondaries from the data. As shown by figure 7.14 Pb-Pb data also shows the trend explained by the local charge conservation. The qualitative correlation trend shown in theory by incorporating hydrodynamical flow and local charge conservation is an indicative of a possible explanation for our results.

7.2.2 Comparison to triggered analysis

In the triggered analysis the construction of the correlation function is carried in a way that the triggered particle is in a higher p_T range whereas the associated particle is in the lower p_T region. For instance, one can choose $2 < {p_T}^{trig} < 3$ GeV and $1 < {p_T}^{asso} < 2$. The main objective of such an analysis is to sample the jets in a desired momentum range. Recently, a study was carried out to model the near side jet shape[176] as a function of centrality for different p_T combinations. Our analysis is not focused on identifying the jet contribution. The correlation structures consist of contributions from jets and modified jets. If we compare to a jet only analysis we can isolate the effect of the jet modifications. In order to make such a comparison a centrality evolution study was carried out in the momentum range of $1< p_T < 3$ GeV.

Figure 7.16 shows the near side centrality evolution of the untriggered correlations. Figure 7.17 shows the comparison to triggered jet shape analysis. The top four 2D correlation structures are from the jet shape analysis and the bottom ones are from this thesis work. The first column is 0-10% and the second column shows the structure after the flow subtraction. The elongation in $\Delta\eta$ our analysis is clearly visible compared to the triggered analysis.The third column is for 60-70% and the right most column shows the flow subtracted structures.

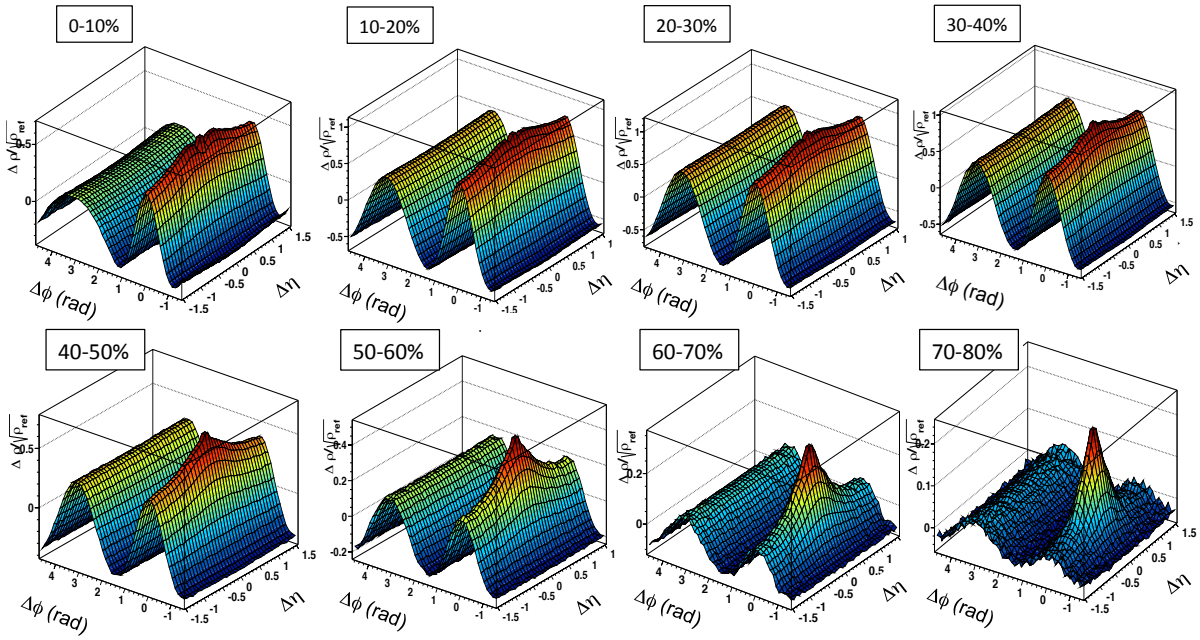

Figure 7.15: Centrality evolution of untriggered correlations in $1< p_T < 3$ GeV.

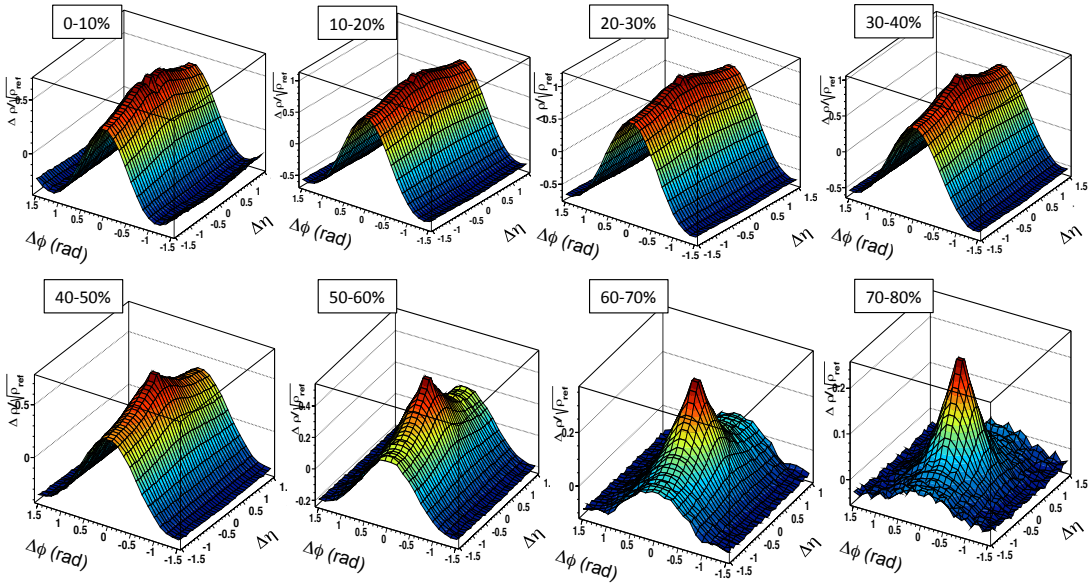

Figure 7.16: Centrality evolution of untriggered correlations in the near-side.

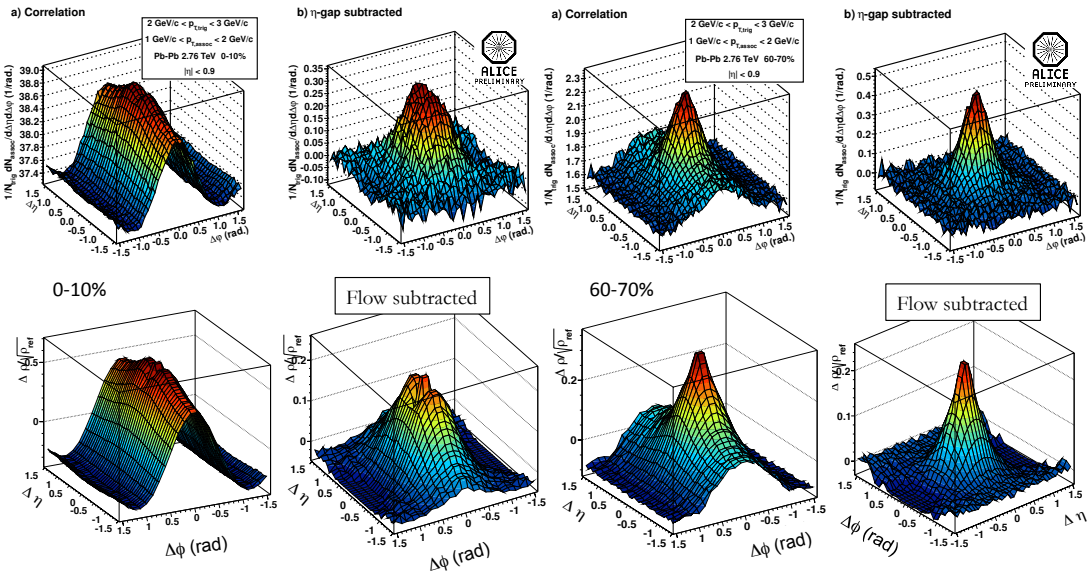

Figure 7.17: Comparison of triggered and untriggered correlations .

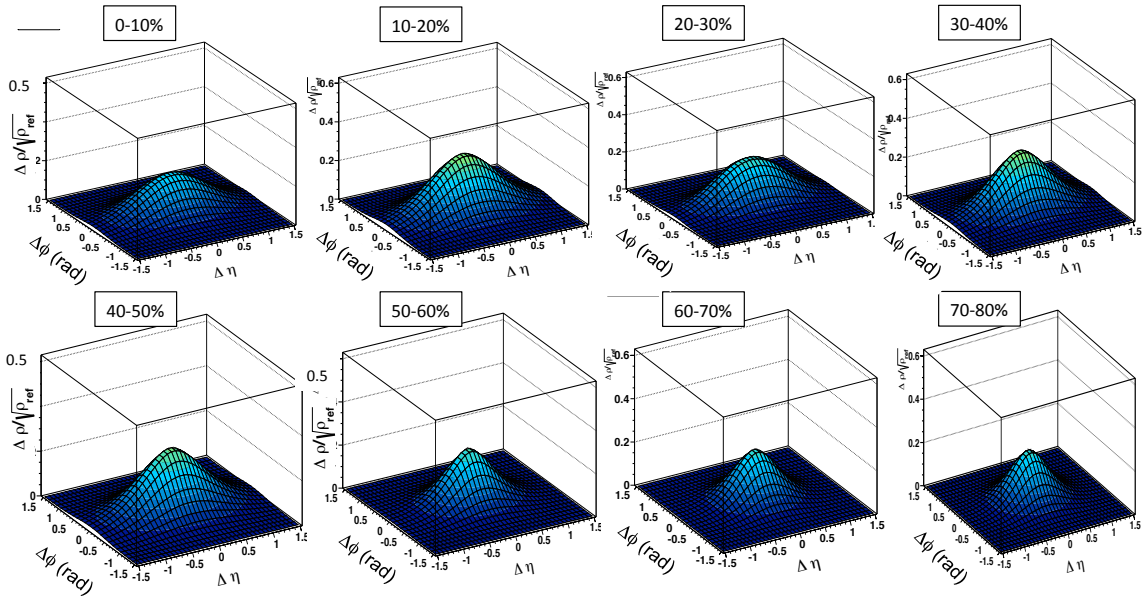

Figure 7.18: Centrality evolution of 2D Gaussian .

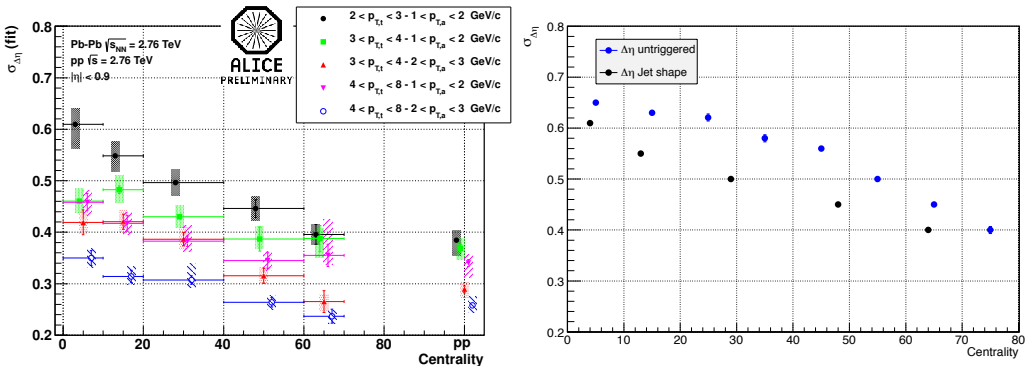

Figure 7.19: Comparison of Gaussian parameters

In order to model the centrality evolution the data are fitted using the same fit function used in the momentum evolution studies in the chapter 5. Figure 7.18 shows the fitted 2D Gaussian as a function of centrality. Figure 7.19 shows the comparison of the Gaussian widths to jet shape analysis as a function of centrality. The black points (corresponding to $2 < {p_T}^{trig} < 3$ GeV/c and $1 < {p_T}^{asso} < 2$ in the left panel) are compared. One can see that there is a difference in the $\Delta\eta$ width in all centralities . The observed difference qualitatively described as a consequence of medium modification of the jets. The strength of the untriggered analysis technique used in this thesis work is the ability to probe the lower momentum region (even < 1 GeV/c). However, the observation needs feedback from the theory and model predictions to quantify the medium modifications, which ultimately will connect to a energy-loss mechanism. Next we discuss the energy-loss mechanisms, which describes the observed behavior.

7.2.3 Energy-loss mechanisms in the QGP medium

One of the extensively studied QGP properties is the energy-loss in the medium. As we briefly discussed in chapter one, the energy-loss in the QGP medium can be related to the R_{AA} measurement. In a R_{AA} measurement, the particle yield in a heavy-ion collision is compared to the corresponding yield in a p + p collision system as a function of p_T. If R_{AA} measures a value of one, implies in a heavy-ion collision the particle yield is a superposition of p + p in that p_T bin, which indicates that no medium effect has taken place.

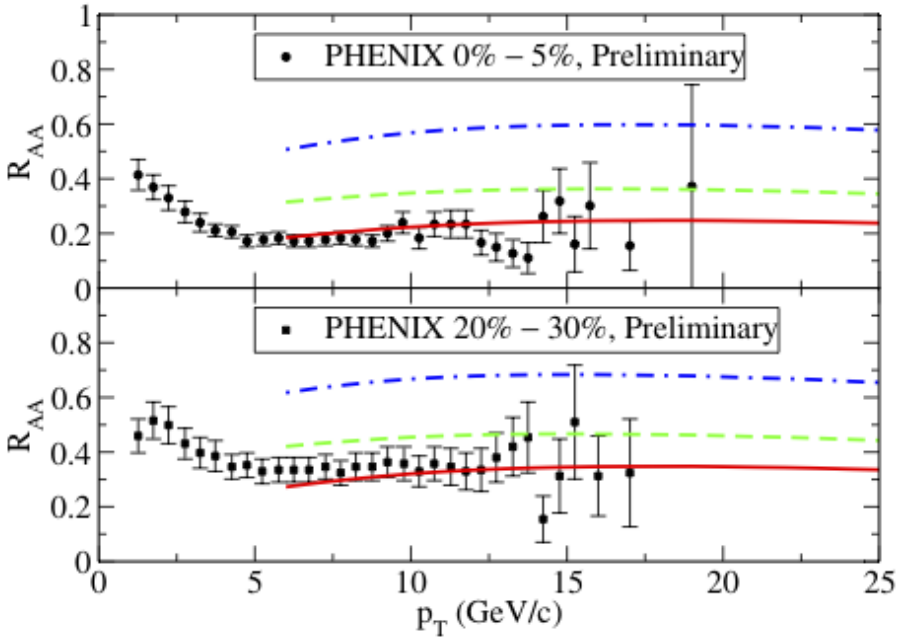

Figure 7.20: Neutral pion suppression factor in central and mid-central 200 GeV Au + Au collisions from PHENIX collaboration compared to theory calculations. Here the dashed dotted curve represents collisional, dashed curve represents radiative and solid curve represents both energy-loss mechanisms taken into consideration [151].

The energy-loss of a traversing high energetic parton in the QGP medium is described in two different mechanisms. First, by elastic scattering [142-144] and second, medium-induced gluon radiation [145-150]. Figure 7.20 shows an example of the different contributions to the π^0 suppression spectrum. The energy-loss models calculate the energy transport coefficient $\hat{q}$ in order to quantify the average energy transfer between the medium and the parton. Thus, the energy transport coefficient $\hat{q}$ is also described as the jet energy transport coefficient.

The energy-loss via gluon radiation is described by two different procedures, which characterized by the equations 7.2 and 7.3. The radiative energy-loss using BDMPS model [152] describes via multiple gluon emission whereas the GLV model [153] the energy-loss describes via single gluon emission.

$$\langle \Delta E \rangle_{BDMPS} \propto \alpha_s C_R \langle \hat{q} \rangle L^2 \tag{7.2}$$

$$\Delta E_{GLV} \propto \alpha_s^3 C_R \frac{1}{A_\perp} \frac{dN^g}{dy} L \tag{7.3}$$

In the BDMPS model, the energy-loss is characterized by the jet transport coefficient $\hat{q}$, whereas the GLV model characterizes the initial gluon density $\frac{dN^g}{dy}$. In the equations, α_s is the strong coupling constant, $\frac{dN^g}{dy}$ is the gluon density per unit rapidity, $A_\perp$ is the transverse area, C_R is the Casimir operator and L is the path length of a parton in the QGP medium. Defining $\hat{q}$ requires the number density density ρ of the constituents in the medium (partons). A definition can be written as,

$$\hat{q} = \rho \int d^2 q_\perp q_\perp^2 \frac{d\sigma}{d^2 q_\perp} \tag{7.4}$$

where $q_\perp$ is the transverse momentum transfer (in the x-y plane) and $\frac{d\sigma}{d^2 q_\perp}$ is the differential scattering cross section of the parton in the medium.

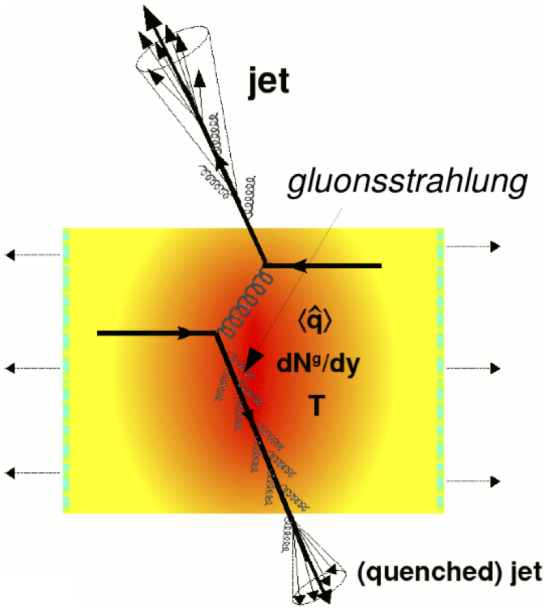

Figure 7.21: A schematic of radiative energy-loss in a hard scattered jet. Some of the the relevant physical quantities which drives the energy-loss, T, $\hat{q}$ and gluon density are notified.

Figure 7.21 shows a schematic view of a hard scattered parton traversing the QGP formed in a heavy-ion collision. The parton shower of the jet on top of the schematic does not interact with the medium if it is emitted from the surface of the QGP (surface jet). If a jet is formed inside the QGP, then the jet interacted with the medium and is called quenched jet. Our measurement shows a broadening of quenched jets with respect to unmodified jets in p + p collisions where a QGP is

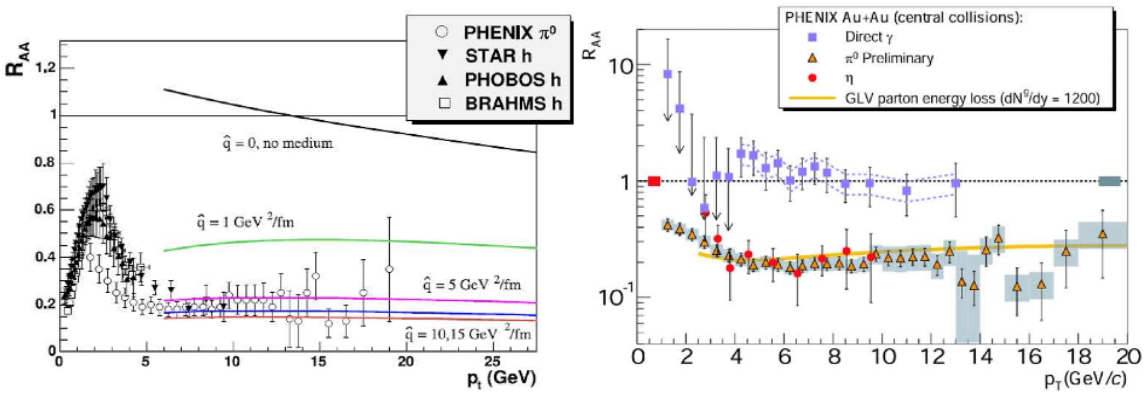

Figure 7.22: left panel:BDMPS models fits to the π^0 and charged hadron R_{AA} as a function of $\hat{q}$. A $\hat{q}$ value of 5 GeV^2/fm corresponds to a $\frac{dN^g}{dy}$ of 900. Right panel: GLV model comparison to π^0 R_{AA} for central Au + Au 200 GeV data from PHENIX. R_{AA} for η and direct γ is also shown without model comparisons

not formed. Though, both GLV and BDMPS model computations shown in figure 7.22 successfully describes the observed R_{AA} measurements, they do not converge to a common $\hat{q}$ value. The GLV calculation gives a range for $\hat{q}$ that is 0.35 - 0.85 GeV^2/fm for $dN^g/dy = 900$ with the corresponding BDMPS value at 5 GeV^2/fm. In fact due to many theoretical uncertainties, $\hat{q}$ ranges from 0.3 - 20 GeV^2/fm [155-157].

The BDMPS model is extended in order to study the jet broadening and corresponding energy-loss, to extract $\hat{q}$ of the QGP [160]. Figure 7.23 shows the mechanism which is implemented in the model. As seen in figure 7.23, the collective flow fields in the medium modifies the high p_T parton fragmentation. The partonic energy-loss mechanism is remodeled by considering flow induced, directed momentum transfer. The asymmetry of energy and multiplicity distributions for the modified jets in the $\eta - \phi$ plane have been calculated and are shown in Figure 7.24. The gluon

energy distribution that resulted from fragmenting the initial scattered parton, can be deduced by coupling the momentum transfer to flow fields in the medium .

A model calculation (shown in Figure 7.24) has been carried out by using, a momentum transfer per scattering center μ of 1 GeV/c, a total transverse jet energy of E_T=100 GeV, a path length L of 6 fm, a collective flow effected momentum transfer q_0 of 1 GeV/c, a jet cone radius of 0.3 and the strong coupling of α_s=1/3. It is also shown that in general the reconstructed jet axis (the symmetry axis of the jet) gets modified (shifted) in the direction of the flow. The multiplicity distribution of the fragmented initial parton is shown in Figure 7.24. The effects is observed in the multiplicity distributions, as expected from the model prediction. As it is implemented in the model, that the long tails of the gluon multiplicity distribution cause the elongation in $\Delta\eta$ correlation function. In the case $\alpha^{'}$=0, gives a slightly higher yield as compared to the $\alpha^{'}=\pi/4$ case. It is evident that as one increases the lower p_T/energy cut off for the partons, the yield closer to the jet axis slightly reduces. For the $\alpha^{'}=\pi/2$ case, the multiplicity distribution is symmetric as one would expect due to relatively smaller medium interactions.

The model study yields qualitative agreement with our analysis as, we observed the both jet broadening and the asymmetry via the 2D Gaussian width evolution as a function of p_T. But more quantitative approach will require knowledge of the jet energy, which is beyond the scope of this thesis.

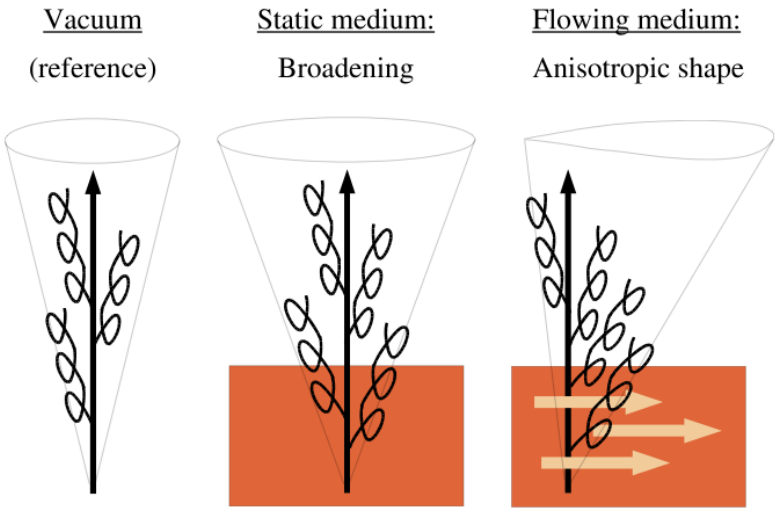

Figure 7.23: A schematic of a jet traversing a). in vacuum b). in a medium which is co-moving with the jet's rest frame c). in a medium which is boosted perpendicularly to the rest frame of the jet. The distribution of radiated parton multiplicity under the influence of a co-moving QGP medium is shown[160].

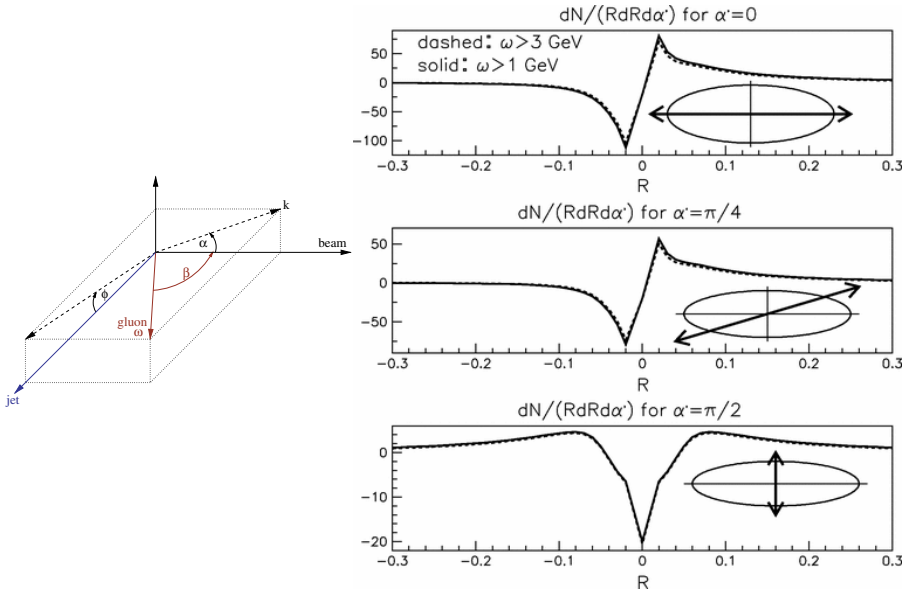

Figure 7.24: The jet multiplicity distribution for different cuts in $\eta - \phi$ plane for two low momentum cut off values, $w > 3$ GeV/c and 1 GeV/c. The flow field acts in the direction of the beam line[160].

7.3 Summary

In summary, we were able to study the transverse momentum evolution of triggered di-hadron correlation analysis in the 0-10% centrality bin using Pb-Pb 2.76 TeV data from the ALICE experiment. A smooth evolution of di-hadron correlation structures as a function of p_T and $\langle\ p_T \rangle$ is observed. The correlation structure was modeled using a Fourier series that consist of terms up to n=5 and a 2d Gaussian structure to model the non-flow contributons in the near side after subtracting out the summed Fourier series contribution. The Fourier series terms are due to possible initial state energy density fluctuation correlation contributions in heavy-ion collisions. We studied the Fourier series terms n$\geq$2 by comparing to an independent analysis from the ALICE experiment, based on single particle measurements with respect to the reaction plane, and observed excellent agreement. Then we focused on characterizing medium properties of the QGP by extracting a value for the shear viscosity (η/s). Our results are consistent with a hydrodynamics based model that uses an η/s value of 0.2, which is within the anticipated range (0.08 - 0.24) for a near perfect liquid close to the quantum limit. It is also about a factor 2 larger than the value obtained with the same model fit for RHIC data. This is consistent with the picture where the strong coupling falls weaker as a function of collision energy.

For the second part of our analysis we focused on the Gaussian profile of non-flow. The region below $p_T = 2.8$ GeV/c was discussed in relation to two possible scenarios that use hydro-dynamical description of QGP. Indications are that the asymmetry in the Gaussian can be attributed primarily to medium modified jets. The observed difference of the $\Delta\eta$ widths between our analysis and the jet shape analysis can be

understood as the contribution from the particles produced via induced gluon distributions that result for partonic energy-loss, i.e., quenched jets in the medium.

7.3.1 Features of the analysis

- A smooth evolution of structures in the measured di-hadron correlation function as a function of increasing momentum is observed
- A multi-component fit function has been proposed to describe the measured structures.
- v_n scaling can be used to describe the flow.
- The 2D Gaussian fit component, which is added to a describe the modified jet contribution, gradually shifts from an asymmetric to a symmetric shape in $\Delta\eta$ and $\Delta\phi$ with increasing momentum

7.3.2 Physics conclusions

- Extracted specific shear viscosity value ($\eta/s = 0.2$) show small viscous contribution to the 'perfect liquid' medium. We have constrained the shear viscosity to a new level of precision.
- The IP Glasma model, which assumes strong gluon saturation in the initial state, and a viscous hydro dynamical evolution of the system describe the data quite well.

- This is consistent with the picture where the strong coupling becomes weaker as a function of collision energy, as similar model study at RHIC estimated ($\eta/\mathrm{s} = 0.12$).
- Gaussian parameters describe the medium modified jets
- Future modeling will provide more constrains for the transport coefficient

Bibliography

[1] http://www.particleadventure.org

[2] G. Steigman, Ann. Rev. Nucl. Part. Phys. 57, 463 (2007)

[3] E. Komatsu et.al., Astrophysical Journal Supplement 180, 330 (2009)

[4] D. Scott, arXiv:astro-ph/0510731 (2005)

[5] Coles, P (2001). *Routledge Critical Dictionary of the New Cosmology*. Routledge, London

[6] UA1, Phys. Lett. B 122, 716 (1983)

[7] Peter W. Higgs, Phys. Rev. Lett. 13, 508 (1964)

[8] ATLAS, Phys. Lett. B 702, 716 (2012)

[9] Edward W. K. and Michael S. T. (1994). *The Early Universe*, p. 447. Westview press, New York, New York

[10] D. Samtleben et.al, Ann. Rev. Nucl. Part. Sci. 57, 245 (2007)

[11] J.D. Bjorken, FERMILAB-Pub-82/59-THY

[12] M. Gyulassy and M. Plumer, Phys. Lett. B 243, 432 (1990); R. Baier et al., Phys. Lett. B 345, 277 (1995)

[13] R. Baier, D. Schiff and B.G. Zakharov, Annu. Rev. Nucl. Part. Sci. B 50, 37 (2000)

[14] X. N. Wang and M. Gyulassy, Phys. Rev. Lett. 68, 1480 (1992); X. N. Wang, Phys. Rev. C 58, 2321 (1998)

[15] E. Wang and X. N. Wang, Phys. Rev. Lett. 89, 162301 (2002); F. Arleo, Phys. Lett. B 532, 231 (2002)

[16] STAR, J. Adams et al., arXiv:nucl-ex/0306024 (2003)

[17] W. Cassing, K. Gallmeister and C. Greiner, arXiv:hep-ph/0311358 (2003)

[18] Cronin et al., Phys. Rev. D 11, 3105 (1975)

[19] Peter Jacobs, Eur. Phys. J. C 43, 467 (2005)

[20] STAR, J. Adams et al., arXiv:nucl-ex/0501016 (2005)

[21] N. Borghini, P.M. Dinh and J.-Y. Ollitrault, Phys. Rev. C 62, 034902 (2000)

[22] STAR, J. Adams et al., arXiv:nucl-ex/0411003 (2004)

[23] J. D Bjorken, Phys. Rev. D 27, 140 (1983)

[24] B. Tomasik, U.A. Wiedemann and U. Heinz, CERN report TH-215 (1999), arXiv:nucl-th/9907096 (1999)

[25] Peter Jacobs, eConf. C020805, TTH05 (2002)

[26] B. Abelev et al., Phys. Rev. Lett. 110, 082302 (2013)

[27] P. K. Kovtun, D. T. Son, A. O. Starinets, Phys. Rev. Lett. 94, 111601 (2005)

[28] K. Aamodt, et al, arXiv:nucl-ex/1012.1004 (2010)

[29] Ulrich Heinz, Chun Shen, Huichao Song, arXiv:nucl-th/1108.5323 (2011)

[30] ALICE, B. Abelev et al., arXiv:nucl-th/1208.2711 (2013)

[31] The ALICE Collaboration et al. JINST 3 S08002 (2008)

[32] H. Hahn et al., Nucl. Instrum. Meth. A 499, 245 (2003)

[33] RHIC Design Manual (1990-2000), http://www.agsrhichome.bnl.gov/AGS/Accel/Reports

[34] J. H. Lee, Notes from Workshop on Thermalization and Chemical Equilibration in Heavy Ions Collisions at RHIC, BNL (2001)

[35] B. B. Back et al., Nucl. Instrum. Meth. A 499, 603 (2003)

[36] STAR, K. H. Ackermann et al., Nucl. Instrum. Meth. A 499, 624 (2003)

[37] H. S. Matis, R. L. Brown, W. Christie, W. R. Edwards, R. Jared, B. Minor and P. Salz, Nucl. Instrum. Meth. A 499, 802 (2003)

[38] STAR, D. Reichhold et al., Nucl. Instrum. Meth. A 499, 792 (2003)

[39] STAR, F. Bergsma et al., Nucl. Instrum. Meth. A 499, 633 (2003)

[40] F. S. Bieser et al., Nucl. Instrum. Methods A 499, 766 (2003)

[41] STAR, C. Adler et al., Nucl. Instrum. Meth. A 499, 778 (2003)

[42] Kalman R. E., Journal of Basic Engineering, pp. 35-45 (1960)

[43] L.V. Gribov, E.M. Levin, and M.G. Ryskin, Phys. Rept. 100, 1 (1983)

[44] A.H. Mueller and J.W. Qiu, Nucl. Phys. B 268, 847 (1986)

[45] LBL online archive: http://www.lbl.gov/Science-Articles/Archive/star/

[46] Particle Data Group. Eur. Phys. J. C15, 1 (2000)

[47] F. Sauli, Technical Report CERN 77-09, CERN (1977)

[48] M. Anderson et.al., Nucl. Instrum. Meth. A 499, 659 (2003)

[49] New State of Matter created at CERN, www.info.web.cern.ch/Press/PressReleases/Releases2000/PR01.00EQuarkGluonMatter.html

[50] M. Stephanov, K. Rajagopal, E. Shuryak, Phys. Rev. D 60 114028 (1999)

[51] STAR, J. Adams et al., Phys. Rev. C 71, 064906 (2005)

[52] STAR, J. Adams et al., J. Phys. G 32, 37 (2006)

[53] K. Pearson, Phil. Trans. Royal Soc. 187, 253 (1896)

[54] T. A. Trainor, R. J. Porter, D. J. Prindle, J. Phys. G 31, 809 (2005)

[55] T. A. Trainor and D. T. Kettler, arXiv:hep-ph/0704.1674 (2007)

[56] A. Einstein, Ann. Phys. 17, 549 (1905)

[57] D. J. Prindle and T. A. Trainor, J. of Phys. Conf. Ser. 27, 118 (2005)

[58] Daugherity, MS (2008), 'Two Particle Correlations in Ultra Relativistic Heavy Ion Collisions: A study of new state of matter created at RHIC', PhD thesis, University of Texas at Austin, Austin, Texas, USA

[59] M. Miller et al., Ann. Rev. Nucl. Part. Sci. 57, 205 (2007)

[60] R. L. Ray and M. Daugherity, arXiv:nucl-ex/0702039 (2007)

[61] S. Voloshin and Y. Zhang, Z. Phys. C 70, 665 (1996)

[62] Michael L. Miller et al., Ann. Rev. Nucl. Part. Sci. 57, 205 (2007)

[63] Derek Teaney and Li Yan, Phys. Rev. C 83, 064904 (2011)

[64] M. Luzum and J.-Y. Ollitrault, Phys. Rev. Lett. 106, 102301 (2011)

[65] M. Luzum and J.-Y. Ollitrault et al., Phys. Rev. C 83, 064901 (2011)

[66] M. Luzum and J.-Y. Ollitrault et al., Phys. Rev. Lett. 108, 252302 (2012)

[67] S. Mohapatra et al., arXiv:nucl-th/1203.3410v1 (2012)

[68] ATLAS, G. Aad et al., Phys. Rev. C 86, 014907 (2012)

[69] B. Andersson, et al., Phys. Rep. 97, 31 (1983)

[70] M. Lisa et al., Ann. Rev. Nucl. Part. Sci 55, 357 (2005)

[71] Guo-Liang Ma and Xin-Nian Wang, Phys. Rev. Lett. 106, 162301 (2011)

[72] B. Alver and G. Roland, Phys. Rev. C 81, 054905 (2010)

[73] B. Schenke, S. Jeon, C. Gale, arXiv:hep-ph/1009.3244 (2010)

[74] Rene Brun and Fons Rademakers, Nucl. Inst. and Methods A 389, 81 (1997)

[75] Ishihara, A (2004), 'Large Scale Two Particle Correlation Structures in Au + Au Collisions at $\sqrt{S_{NN}} = 130GeV$: A study of new state of matter created at RHIC', PhD thesis, University of Texas at Austin

[76] Xin-Nian Wang and Miklos Gyulassy, Phys.Rev. D 44, 3501 (1991)

[77] Joern Putschke et.al., J. Phys. G 34, S679 (2007)

[78] D. Magestro, talk given at Hard Probes (2004)

[79] L. Ray and M. Daugherity, J. Phys. G: Nucl. Part. Phys. 35, 125106 (2008)

[80] R. J. Porter and T. A. Trainor, J. of Phys. Conf. Ser. 27, 98 (2005)

[81] M. Lisa, et al., Ann. Rev. Nucl. Part. Sci. 55, 357 (2005)

[82] T. A. Trainor and D. T. Kettler, arXiv:hep-ph/0704.1674 (2007)

[83] T. Ludlam and L. McLerran, What have we learned from the Relativistic Heavy Ion Collider?, Phys. Today 56N10, 48 (2003)

[84] L. McLerran, arXiv:hep-ph/0804.1736 (2008)

[85] L. V. Gribov, E. M. Levin, and M. G. Ryskin, Phys. Rept. 100, 1(1983)

[86] A. H. Mueller and J.-w. Qiu, Nucl. Phys. B 268, 427 (1986)

[87] J. P. Blaizot and A. H. Mueller, Nucl. Phys. B 289, 847 (1987)

[88] L. D. McLerran and R. Venugopalan, Phys. Rev. D 49, 2233 (1994); arXiv:hep-ph/9309289 (1993)

[89] L. D. McLerran and R. Venugopalan, Phys. Rev. D 49, 3352 (1994); arXiv:hep-ph/9311205 (1993)

[90] Moschelli, G (2010), 'Two Particle Correlations and The Ridge in Relativistic Heavy Ion Collisions: A study of new state of QCD matter', PhD thesis, Wayne State University

[91] L. McLerran, Prog. Theor. Phys. Suppl. 187, 17 (2011)

[92] G. Moschelli and S. Gavin, arXiv:nucl-th/0910.3590 (2009)

[93] G. Moschelli, S. Gavin and L. McLerran, arXiv:nucl-th/0806.4718 (2008)

[94] L. C. De Silva, arXiv:nucl-ex/0910.5938 (2009)

[95] E. Schnedermann, J. Sollfrank and U. W. Heinz, Phys. Rev. C 48, 2462 (1993)

[96] Zi-Wei Lin, Che Ming Ko, Bao-An Li, Bin Zhang, Subrata Pal, Phys. Rev. C 72, 064901(2005)

[97] F. Retiere and M. A. Lisa, Phys. Rev. C 70, 044907 (2004)

[98] L. C. De Silva, arXiv:nucl-ex/1112.1111v1 (2011)

[99] L.C. De Silva, arXiv:nucl-ex/1209.4941 (2012)

[100] C. Gombeaud et al., Phys. Rev. C 81, 014901 (2010)

[101] STAR, Y. Pandit, arXiv:nucl-ex/1210.5315 (2012)

[102] A. M. Poskanzer and S. A. Voloshin, Phys. Rev. C 58, 1671 (1998)

[103] STAR, C. Adler et al., Phys. Rev. C 66, 034904 (2002)

[104] B. Schenke and P. Tribedy et.al, Phys. ReV. Lett. 108, 252301 (2012)

[105] B. Schenke and P. Tribedy et.al, arXiv:nucl-th/1209.6330 (2012)

[106] N. Borghini and J. Y. Ollitrault, Phys. Lett. B 642, 227 (2006)

[107] STAR, J. Adams et al., Phys. Rev. Lett. 92, 062301 (2004)

[108] PHENIX, H. Masui, Nucl. Phys. A 774, 511 (2006)

[109] STAR, B. I. Abelev et al., Phys. Rev. C 75, 054906 (2007)

[110] PHENIX, S. Huang, J. Phys. G 35, 104 (2008)

[111] B. Schenke, Quark Matter 2012, Washington, DC

[112] J. Bartels, K. J. Golec-Biernat, and H. Kowalski, Phys. Rev. D 66, 014001 (2002)

[113] H. Kowalski and D. Teaney, Phys. Rev. D 68, 114005 (2003)

[114] A. Kovner, L. D. McLerran, and H. Weigert, Phys. Rev. D 52, 6231 (1995)

[115] Y. V. Kovchegov and D. H. Rischke, Phys. Rev. C 56, 1084 (1997)

[116] A. Krasnitz and R. Venugopalan, Nucl. Phys. B 557, 237 (1999); Phys. Rev. Lett. 84, 4309 (2000); 86, 1717 (2001)

[117] T. Lappi, Phys. Rev. C 67, 054903 (2003)

[118] B. Schenke, P. Tribedy, and R. Venugopalan, Phys. Rev. C 86, 034908 (2012)

[119] B. Schenke, S. Jeon, and C. Gale, Phys. Rev. C 82, 014903 (2010)

[120] B. Schenke, S. Jeon, and C. Gale, Phys. Rev. Lett. 106, 042301 (2011)

[121] B. Schenke, S. Jeon, and C. Gale, Phys. Lett. B 702, 59 (2011)

[122] B. Schenke, S. Jeon, and C. Gale, Phys. Rev. C 85, 024901 (2011)

[123] P. Huovinen and P. Petreczky, Nucl. Phys. A 837, 26 (2010)

[124] F. Cooper and G. Frye, Phys. Rev. D 10, 186 (1974)

[125] G. Policastro, D. T. Son and A. O. Starinets, Phys. Rev. Lett. 87, 081601 (2001)

[126] P. Kovtun, D. T. Son, and A. O. Starinets, Phys. Rev. Lett. 94, 111601 (2005)

[127] M. Luzum and P. Romatschke, Phys. Rev. C 78, 034915 (2008)

[128] Todd Springer and Mikhail Stephanov, arXiv:nucl-th/1210.5179v1 (2012)

[129] Piotr Bozek and Wojciech Broniowski, arXiv:nucl-th/1210.4315v1 (2012)

[130] J. Kapusta, B.Muller and M. Stephanov, Phys. Rev. C 85, 054906 (2012)

[131] P. Staig and E. Shuryak, Phys. Rev. C 84, 044912 (2011)

[132] S. A. Bass, P. Danielewicz, S. Pratt, Phys. Rev. Lett. 85, 2689 (2000)

[133] S. Jeon, S. Pratt, Phys. Rev. C 65, 044902 (2002)

[134] P. Bozek, Phys. Lett. B 609, 247 (2005)

[135] M. M. Aggarwal, et al., Phys. Rev. C 82, 024905 (2010)

[136] P. Bozek, W. Broniowski, Phys. Rev. Lett. 109, 062301 (2012)

[137] P. Bozek, Phys. Rev. C 85, 034901 (2012)

[138] P. Bozek, Phys. Rev. C 81, 034909 (2010)

[139] W. Broniowski, M. Rybczynski, P. Bozek, Comput. Phys. Commun. 180, 69 (2009)

[140] M. Chojnacki, A. Kisiel, W. Florkowski, W. Broniowski, Comput. Phys. Commun. 183, 746 (2012)

[141] G. Agakishiev, et al., arXiv:nucl-ex/1109.4380 (2011)

[142] J. D. Bjorken, Fermilab preprint Pub-82/59-THY (1982)

[143] E. Braaten and M. H. Thoma, Phys. Rev. D 44, 2625 (1991)

[144] S. Peigné and A. Peshier, Phys. Rev. D 77, 114017 (2008)

[145] M. Gyulassy and X.-N. Wang, Nucl. Phys. B 420, 583 (1994)

[146] R. Baier, Y. L. Dokshitzer, A. H. Ḿuller, S. Peigné, and D. Schiff, Nucl. Phys. B 483, 291 (1997); ibid. 484, 265 (1997)

[147] M. Gyulassy, P. Levai, and I. Vitev, Phys. Rev. Lett. 85, 5535 (2000); Nucl. Phys. B 571, 197 (2000); ibid. 594, 371 (2001)

[148] P. B. Arnold, G. D. Moore, and L. G. Yaffe, JHEP 0011, 001 (2003); ibid. 0305, 051 (2003)

[149] N. Armesto, C. A. Salgado, and U. A. Wiedemann, Phys. Rev. D 69, 114003 (2004); Phys. Rev. C 72, 064910 (2005)

[150] B. G. Zakharov, JETP Lett. 63, 952 (1996); ibid. 64, 781 (1996); ibid. 65, 615 (1997); ibid. 73, 49 (2001); ibid. 78, 759 (2003)

[151] G. Qin et al., Phys. Rev. Lett. 100, 072301 (2008)

[152] Eskola, Honkanen, Salgado and Weidemann, Nucl. Phys. A 747, 511 (2005)

[153] M. Gyulassy, P. Levai and I. Vitev, Phys. Lett. B 594, 371 (2001)

[154] J. Lajoie, Braz. J. Phys. vol. 37, no. 2C, June (2007)

[155] F. Arleo, JHEP 0211, 044 (2002)

[156] K. J. Eskola, H. Honkanen, C. A. Salgado and U. A. Wiedemann, Nucl. Phys. A 747, 511 (2005)

[157] R. Baier and D. Schiff, JHEP 0609, 059 (2006)

[158] I. Vitev et al., JHEP 0811, 093 (2008)

[159] I. Vitev et al., Phys. Rev. Lett. 104, 132001(2010)

[160] Nstor Armesto et al., Phys. Rev. C 72, 064910 (2005)

[161] A. Majumder et al., Phys. Rev. Lett. 99, 192301 (2007)

[162] H.-U. Bengtsson, Computer Physics Commun. 31, 323 (1984)

[163] N. Borgini, PoSLHC07, 013 (2007)

[164] S. Hands, Contemp. Phys. 42, 209 (2001)

[165] E. Oset et al., Eur. Phys. J. A 44, 431 (2010)

[166] The Hebrew University of Jerusalem:
http://www.phys.huji.ac.il/˜paul/files/eras_of_universe.jpg

[167] DashLB: http://zewex.blogspot.com/2010/09/doppler-effect.html

[168] RIKEN BNL: http://www.riken.jp/engn/r-world/info/release/news/2003/aug/index.html

[169] Feng, A (2008), 'Di-hadron Azimuthal Correlations Relative to Reaction Plane in Au + Au Collisions at $\sqrt{S_{NN}} = 200$ GeV', PhD thesis, Central China Normal University, Wuhan, CHINA

[170] Berger, J (2003), 'Anti-Proton to Proton Ratio in Au+Au Collisions at STAR', PhD thesis, Johann Wolfgang Goethe-University, Frankfurt, Germany

[171] Ulery, JG (2007), 'Two and Three Particle Jet-like correlations', PhD thesis, Purdue University, Indiana, USA

[172] B.Alver, M.Baker, C.Loizides, P.Steinberg, arXiv:nucl-ex/0805.4411v1(2008)

[173] A.M Adare et al., Phys. Lett. B 708 (2012)

[174] A. Timmins, arXiv:nucl-ex/1106.6057 (2011)

[175] K. Aamodt et al., Phys. Rev. Lett. 107, 032301(2011)

[176] ALICE, arXiv:hep-ex/1311.2394v2 (2013)

[177] R. Barlow, arXiv:hep-ex/0207026 (2002)

[178] NASA, http://map.gsfc.nasa.gov/site/citations.html

[179] Planck Collaboration, arXiv:astro-ph.CO/1502.01582 (2015)

[180] CERN, http://snelling.web.cern.ch/snelling/my-research.html

[181] http://www.quantumdiaries.org/tag/heavy-ion-physics/page/2/

[182] CERN, http://home.web.cern.ch/about/accelerators

[183] The ALICE Collaboration et al., JINST 3 S080002 (2008)